Functional Nanoporous Polymers from Block Copolymer Precursors

Guo, Fengxiao

Publication date:
2010

Document Version
Publisher's PDF, also known as Version of record

Functional Nanoporous Polymers from Block Copolymer Precursors

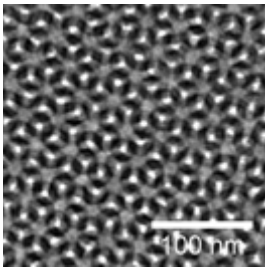

Nanoporous gyroid 1,2-PB before…

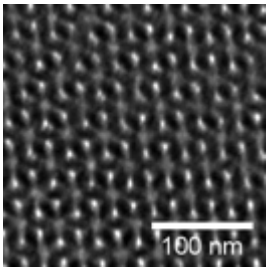

…and after PPEGMA grafting

Fengxiao Guo
Ph.D. Thesis
2010

DTU Chemical Engineering
Department of Chemical and Biochemical Engineering

Functional Nanoporous Polymers from Block Copolymer Precursors

Fengxiao Guo

23rd June, 2010

Department of Chemical and Biochemical Engineering

Technical University of Denmark

ISBN-978-87-92481-25-2

Printed in Denmark by
WWW.FRYDENBERG.DK
Baldersgade 12 - 16
DK-2200 Copenhagen N

Abstract

Self-assembly of block copolymers provides well-defined morphologies with characteristic length scales in the nanometer range. Nanoporous polymers prepared by selective removal of one block from self-assembled block copolymers offer great technological promise due to their many potential applications as, e.g., membranes for separation and purification, templates for nanostructured materials, sensors, substrates for catalysis, low dielectric constant materials, photonic materials, and depots for controlled drug delivery. The development of nanoporous polymers with well controlled pore wall functionalities remains a great challenge due to the limitation of available polymer synthesis and the nanoscale confinement of the porous cavities. The main topic of this thesis is to develop methods for fabrication of functional nanoporous polymers from block copolymer precursors.

A method has been developed, where living anionic polymerization and atom transfer radical polymerization (ATRP) are combined to synthesize a polydimethylsiloxane-*b*-poly(*tert*-butyl acrylate)-*b*-polystyrene (PDMS-*b*-P*t*BA-*b*-PS) triblock copolymer precursor. By using either anhydrous hydrogen fluoride or trifluoroacetic acid, P*t*BA block can be hydrolyzed to hydrophilic poly(acrylic acid) (PAA) and PDMS can be quantitatively etched. The resultant material is nanoporous PS with hydrophlilic PAA pores.

Surface-initiated ATRP and click chemistry have been utilized as '*grafting from*' and '*grafting to*' techniques respectively to fabricate functional nanoporous polymers based on nanoporous 1,2-polybuatdiene 1,2-PB, which is derived from a 1,2-PB-*b*-PDMS diblock copolymer precursor. As a result, nanoporous 1,2-PB with pores decorated of polyacrylates, sulfonated polymers and poly(ethylene glycol) are created.

A method of vapor phase deposition has also been generated to obtain nanoporous polymers with functional coatings on pore walls. Vapor phase polymerization of pyrrole is performed to incorporate an ultra thin film of polypyrrole into nanoporous 1,2-PB. The preliminary test shows that nanoporous 1,2-PB gains conductivity.

Generally cross-linking is needed to provide sufficient mechanical stability for the matrix which has glass transition temperature lower than room temperature. Insufficient cross-linking can lead to

collapse of pores after removal of the sacrificial component. However, with a low cross-linking degree, such collapsed matrixes may have reversible nanoporosity. A collapsed 1,2-PB matrix is prepared by cross-linking insufficiently before etching PDMS block away from a 1,2-PB-*b*-PDMS diblock copolymer precursor. Nanoporosity with ordered morphology is found to be re-established when the 1,2-PB matrix is subjected to a good solvent. Load and release of macromolecular chemicals in these 'latently porous' materials was demonstrated, which is of direct relevance for drug delivery applications.

Dansk resumé

Selv-organiseret blok copolymerer viser veldefinerede morfologier med karakteristiske længdeskalaer i nanometer området. Nanoporøse polymerer dannet via selektiv fjernelse af en blok fra selv-organiseret blok copolymerer fodrer et spændende teknologisk perspektiv på grund af deres mange anvendelsesmuligheder som fx membraner til separation og rensning, skabeloner for nanostrukturerede materialer, sensorer, substrater til katalyse, lav dielektrisk konstant materialer, fotoniske materialer og depoter for kontrolleret medicin afgivelse. Udviklingen af nanoporøse polymerer med kontrolleret poreoverflade funktionalitet er fortsat en stor udfordring på grund af begrænsninger i polymer syntese samt nanoskala confinement. Det vigtigste emne i denne afhandling er at udvikle metoder til fremstilling af funktionelle nanoporøse polymerer fra blok copolymer startmaterialer.

En metode er blevet udviklet, hvor anionisk polymerisering og atom transfer radikal polymerisation (ATRP) kombineres til at syntetisere en polydimetylsiloxan-*b*-poly(*tert*-butyl akrylat)-*b*-polystyren (PDMS-*b*-PtBA-*b*-PS) triblok copolymer. Vi har opdaget at vandfri hydrogenfluorid eller trifluoreddikesyre, kan på samme tid omdanne PtBA blokken til hydrofile polyakrylsyre (PAA) og kvantitativt ætse PDMS. Det resulterende materiale er nanoporøse PS med hydrofile PAA porer.

Overflade-initierede ATRP og klik kemi er henholdsvis blevet udnyttet som 'podning fra' og 'podning til' teknikker til fremstilling af funktionelle nanoporøse 1,2-polybutadien (1,2-PB). Nanoporøse 1,2-PB funktionaliseret med polyakrylater, polysulfoner og polyethylenglykoler blev forberedt vha. denne metode.

En metode til dampfase deponering i nanoporøse 1,2-PB af den elektriske ledende polymer, polypyrrol er også blevet udviklet. Dampfase polymerisering af pyrrol udføres resulterende i en tynd film af polypyrrole i nanoporøse 1,2-PB. De foreløbige test viser, at nanoporøse 1,2-PB bliver elektrisk ledende efter behandlingen.

Høj tværbindingsgrad er nødvendig for at tildele polymermatrixen tilstrækkelig mekanisk stabilitet for porøsitetsopretholdelsen over glasovergangstemperaturen. Lav tværbindingsgrad kan føre til sammenbrud af porerne efter ætsning af 'porogen' blokken. En sådan kollapsede matrix kan dog vise reversible nanoporøsitet. En kollapset PB matrix blev fremstillet vha. lav tværbindingsgrad før

ætsning af PDMS blokken fra en 1,2-PB-*b*-PDMS diblok copolymer. 1,2-PB matrixen i en god solvent viste nanoporøsitet med den forventede morfologi. Indkapsling og frigivelse af et kemisk stof i disse 'latente porøse' materialer blev påvist med klar interesse for drug delivery applikationer.

Acknowledgements

I would like to thank my supervisors, Senior Scientist Sokol Ndoni, Associate Professor Katja Jankova, Professor Martin E. Vigild and Professor Ole Hassager for their excellent guidance and support during this project. In particular, very special thanks to Sokol Ndoni and Katja Jankova for their endless patience, inspiring discussions, many research assistance, introducing me to the field of polymer science, and guiding me how to become a scientific researcher. Thanks to Martin E. Vigild for giving me the opportunity to start my scientific career as a PhD student at the Danish Polymer Centre (DPC). Thanks to Ole Hassager for having me at the DPC as a master student 6 years ago. The past 6 years has been a most valuable experience for me.

I am grateful to Lars Schulte, Piotr P. Szewczykowski, Li Li, Kaushal S. Sagar, Anton Berthold and other former and current members of the Nanoporous Group for their support, interesting discussions and advices throughout the project.

I want to thank Jens, W. Andreasen, Brian Pauw, and Jan Kehres for their assistance during the SAXS measurements at Risø DTU. I also want to thank Tomás S. Plivelic for his support in the SAXS measurements at beamline I711 at MAX-lab, Sweden, and Sandor Balog for his help during our SANS measurements at Paul Scherrer Institut, Switzerland.

I wish to express my appreciation to Anders E. Daugaard, Charlotte J. Fristrup, Irakli Javakhishvili, Professor Søren Hvilsted and Lab Coordinator Kim C. Szabo for their help on the polymer synthesis and characterization, and sharing the chemistry lab with me.

I would also like to thank all the staff at the DPC for a wonderful 6 years. I will miss the Thursday's cake, the Friday's hockey and beer, and the pizza seminar.

Last, but most importantly, thanks to my wife Nan, my daughter Xiqiao and my parents, Baocheng and Junhua for their love, support, and encouragement.

The project is financed by the Technical University of Denmark.

Abbreviations

AMPS	2-Acrylamido-2-methyl-1-propanesulfonic acid
AQ	Anthraquinone
ATRP	Atom transfer radical polymerization
BPB	Bromophenol blue
BPBriBu	Benzophenonyl bromoisobutyrate
*m*CPBA	*meta*-Chloroperoxybenzoic acid
CuAAC	Cu(I)-catalyzed azide-alkyne cycloaddition
D_3	Hexamethylcyclotrisiloxane
DCC	Dicyclohexylcarbodiimide
DCP	Dicumyl peroxide
DIBAL-H	Diisobutylaluminum hydride
DLP	Dilauroyl peroxide
DMAP	4-(Dimethylamino)pyridine
DMF	*N,N*-Dimethylformamide
DOG	Degree of grafting
2-EBP	Ethyl 2-bromo propionate
Fe(III)pTs	Iron (III) *p*-toluenesulfonate
FT-IR	Fourier transform -infrared spectroscopy
FTO	Fluorine-doped tin oxide
GYR	Gyroid
HEMA	2-Hydroxyethyl methacrylate
HEX	Hexagonally packed cylindrical structure
HPL	Hexagonally perforated lamellar
LAM	Lamellar
MeOH	Methanol
d-MeOH	*deuterated*-Methanol
MMA	Methyl methacrylate
d-MMA	*deuterated*-Methyl methacrylate
*M*n	Number-average molecular weight

MPEG	Methoxy poly(ethylene glycol)
N	Degree of polymerization
NaStS	Sodium 4-styrenesulfonate
NMR	Nuclear magnetic resonance
NMRP	Nitroxide-mediated radical polymerization
NMs	Nanoporous materials
NPs	Nanoporous polymers
ODT	Order disorder transition
OOT	Order order transition
PAA	Poly(acrylic acid)
PAMPS	Poly(2-acrylamido-2-methyl-1-propanesulfonic acid)
1,2-PB or PB	1,2-Polybutadiene
PCEMA	Poly(2-cinnamoylethyl methacrylate)
PDI	Polydispersity index
PDMA	Poly(N,N-dimethylacrylamide)
PDMS	Polydimethylsiloxane
PEG	Poly(ethylene glycol)
d-PEG	*deuterated*-Poly(ethylene glycol)
PEGMA	Poly(ethylene glycol) methacrylate
PEO	Poly(ethylene oxide)
P4FS	Poly(4-fluorostyrene)
PHEMA	Poly(2-hydroxyethyl methacrylate)
PI	Polyisoprene
PLA	Polylactide
PMDETA	*N*,*N*,*N*′,*N*″,*N*″-Pentamethyldiethylenetriamine
PMMA	Poly(methyl methacrylate)
PPEGMA	Poly(poly(ethylene glycol) methacrylate)
PPFS	Poly(pentafluorostyrene)
PPO	Poly(propylene oxide)
PPQ	Poly(phenylquinoxaline)
PPy	Polypyrrole
PS	Polystyrene

PSS	Poly(4-styrenesulfonate)
P*t*BA	Poly(*tert*-butyl acrylate)
RAFT	Reversible addition-fragmentation chain transfer polymerization
ROMP	Ring-opening metathesis polymerization
SALS	Samll angle light scattering
SANS	Small angle neutron scattering
SAXS	Small angle X-ray scattering
SEC	Size exclusion chromatography
SEM	Scanning electron microscopy
SLD	Scattering length density
TBAF	Tetrabutyl ammonium fluoride
TEA	Triethylamine
TEM	Transmission electron microscopy
TFA	Trifluoroacetic acid
THF	Tetrahydrofuran
UV-Vis	Ultra violet visible spectroscopy
VPP	Vapor phase polymerization
XPS	X-ray photoelectron spectroscopy

Contents

Chapter 1 General Introduction

1.1 Nanoporous polymers

Porous materials are widely used in many industries including chemistry, food, oil and gas, medicine and environment due to their unique properties, which the counterpart bulk materials don't possess. Nanoporous materials (NMs), which have pore diameters between 1 - 100 nm, are a subset of porous materials. NMs encompass both microporous materials (e.g. zeolites) and mesoporous materials (e.g. porous polymers, alumina and glass) for which the International Union of Pure and Applied Chemistry (IUPAC) has recommended the pore diameters range: smaller than 2 nm and 2 - 50 nm respectively.[1] According to chemical compositions, NMs can be classified as: inorganic materials such as aluminosilicates, metals, oxides, glass and carbon, and organic materials such as polymers. The common properties shared by these NMs are high specific surface area and large porosity. Nevertheless, different NMs do have their own potential applications depending on composition, pore size, pore distribution and porosity. For example, nanoporous TiO_2 has a strong photocatalytic effect due to its high selectivity and controlled large and accessible surface area.[2] Nanoporous carbon and zeolites can be used as adsorbents for hydrogen storage.[3] Materials with pores percolative to surface of the materials can be used in applications such as separation, adsorption and catalysis. Materials with isolated pores are useful in applications of thermal insulation, lightweight and low dielectric constant materials. Furthermore, depending on the preparation strategy, both ordered pore structures and irregular pore structures can be fabricated.

Generally nanoporous polymers (NPs) have relatively lower thermal and chemical stabilities, in comparison to inorganic nanoporous materials. However, some performance criteria may require materials with such properties. For example, NPs are good templates to synthesize other nanostructured materials, because they can be easily removed by either chemical or thermal treatment after growth of the nanostructured materials. The advantages of NPs are also obvious. They include low cost, ease of synthesis and controlled properties. For example, pore size, pore distribution and porosity can be well tuned by adapting different preparation methods and a diverse range of flexibility, conductivity, biocompatibility and hydrophilicity can be realized for NPs.

Nanoporous polymers can be prepared by different ways. Some methods belong to 'bottom-up' approaches, and some belong to 'top-down' approaches. Herein a short introduction to the different techniques is given.

Track etching. This technique involves two important steps: (i) irradiation is used to produce latent tracks; (ii) chemical etching is used to remove the latent tracks to form pore channel. Poly(ethylene terephthalate) or polycarbonate with tunable cylindrical pores and narrow pore size distribution is usually obtained by this technique. Pores in the range of 10 nm-10 μm and a pore density of 1 to 10^{10} cm^{-2} have been reported.[4] However, the pore density or porosity obtained with track etching is generally low, and possibility of generating different pore structures is limited. Track etching is a typical 'top-down' approach.

Organic-inorganic hybrid. Inorganic templates such as colloidal silica particles are dispersed in a polymer network, which is cross-linkable. After cross-linking the polymer phase and removing the silica particles, highly porous structure can be obtained and the size of the pores is similar to the size of silica nanoparticles.[5]

Micellar imprinting. In this technique, the reverse micelles are formed by stabilizing the organic phase which contains monomers/cross-linkers (continuous) and aqueous phase (dispersed by surfactants). The monomers are cross-linked to form a polymer matrix, followed by extracting reverse micelles from this matrix to get the nanoporous polymer. The nature of micelles directly influences the pore size and porosity of the final nanoporous polymers. Normally pores generated from this method are isolated and closed.[6,7]

Freeze drying. This technique is based on the principle that the solubility of polymer in a solvent depends upon temperature. By varying the temperature and composition of the polymer solution phase separation can be carried out. The morphology can be frozen by lowering temperature rapidly with liquid nitrogen. Then the solvent can be removed by freeze-drying to form porous materials.[8]

Carbon dioxide foaming. In this technique, polymers are saturated with a supercritical or gaseous carbon dioxide (CO_2) at high pressure. Then pressure is reduced or temperature is increased to 'freeze' the mixture of the polymer and gas into a supersaturated state. The gas cells nucleate and grow through the polymer matrix before the thermodynamic forces vanish. In this method, supercritical or gaseous CO_2 plays the role of a solvent.[9] The advantage of this method is that no toxic organic residues are left in nanoporous polymers.

Microemulsion. In this technique, a microemulsion system containing monomers, water and co-surfactant is used. Monomers are polymerized and then resultant polymers are solidified. Water can be extracted out before formation of nanoporous polymers.[10] The final formed porous morphology usually depends upon the microstructure of the microemulsion and phase separation. This microemulsion system can be extended to polymer blends. Monomer and water can be substituted with two immiscible homepolymer A and B, and co-surfactant can be replaced by a block copolymer AB. Phase separation occurs in the polymer blend. By cross-linking one phase and selectively removing the other phase, the nanoporous polymers can be generated.[11] This technique is considered as a 'bottom-up' approach.

Block copolymers. The thermodynamic immiscibility of block copolymers is the driving force for self-organization into ordered structure on the nanometer scale. Nanoporous polymers can be obtained by selectively removing one of the blocks (see figure 1.1). The structure of final nanoporous polymers depends on morphology of their block copolymer precursors.[12] Compared to other methods described above, employing the self-assembly of block copolymers allows designing and tailor-making nanoporous polymers at the molecular level. Thanks to the self-assembly, tunable pore size (5 - 50 nm), narrow pore size distribution and controlled pore shape can be obtained. In addition, various morphologies with the high degree of order can be achieved. The ability to control the size and structure of block copolymers on the nanometer scale offers the possibility to obtain desired properties. Using the self-assembly of block copolymers is a typical 'bottom-up' technique.

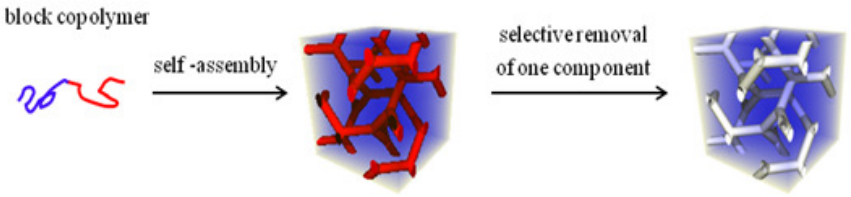

Figure 1.1 Schematic illustration of the preparation of nanoporous polymers from block copolymer precursors.

In this thesis the emphasis is on the preparation of nanoporous polymers from block copolymers. Block copolymer is the starting point for the thesis work, so it is necessary to briefly introduce the background knowledge about block copolymer before further discussion.

1.2 Block copolymers

Block copolymers consist of two or more chemically distinct homopolymer subunits (blocks), which are covalently connected at their ends. Block copolymers with two, three, four, and more blocks are called diblocks, triblocks, tetrablocks and multiblocks. They can be synthesized by using living polymerization techniques, such as living anionic or cationic polymerizations, atom transfer radical polymerization (ATRP), nitroxide-mediated controlled radical polymerization (NMRP), reversible addition-fragmentation chain transfer polymerization (RAFT) and ring opening metathesis polymerization (ROMP). In addition to living polymerization techniques, a recently developed 'click chemistry' is extensively applied to couple two blocks to form diblock copolymers.

Owing to a collective compromise between the blocks' immiscibility and their constraint as parts of the same molecules, a block copolymer can self assemble into structures on the nanometer scale. The periodicity of the structures is normally in the range of 5 - 50 nm,[13] which is a typical length scale for a polymer chain. As shown in Figure 1.2, the simplest case of block copolymers, an AB diblock copolymer, can form the following four equilibrium morphologies: body-centered cubic spheres (0D), hexagonal-packed cylinders (1D), lamellae (2D) or bicontinuous gyroid (3D) depending on the total block length, the composition of the blocks and the strength of interaction between the blocks.[14] The total block length is proportional to the total degree of polymerization, N. The composition of the blocks can be expressed in terms of the volume fractions of the blocks $f_A=V_A/V$, and $f_B=1-f_A$. The strength of interaction between the blocks can be represented by the Flory–Huggins interaction parameter, χ, which is inversely proportional to temperature. The value of χ stands for the incompatibility of the two blocks and the value increases for more incompatible blocks. Self assembly only takes place when the product χN exceeds a critical value, the order disorder transition (ODT).

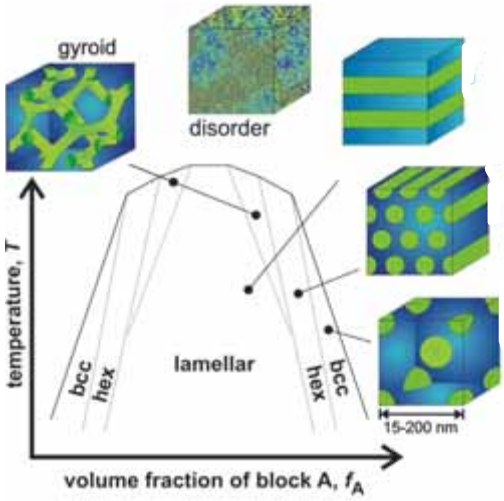

Figure 1.2 Theoretical phase diagram of linear AB block copolymers.[15]

With increasing number of the blocks, the equilibrium morphologies of block copolymers become more complex and diverse. For ABC triblock copolymers, the two composition variables (f_A and f_B, $f_A + f_B + f_C = 1$) and three interaction parameters (χ_{AB}, χ_{AC} and χ_{BC}) largely increase the range of morphological possibilities,[14] some of which can be seen in Figure 1.3.

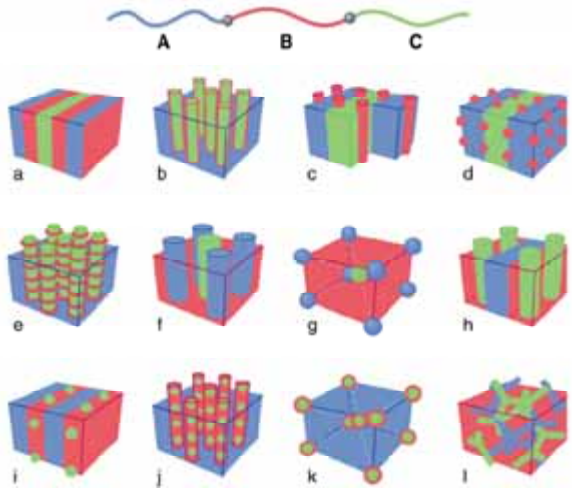

Figure 1.3 Schematic morphologies for linear ABC triblock copolymers.[14]

The self-organization of block copolymers can be exploited as a "bottom up" technique to create nanostructures for various applications. Apart from nanoporous polymers, many efforts have been made to utilize block copolymers for nanoparticle synthesis, photonic crystals, nanoreactors and high-density information storage media. There are several excellent reviews on the application of block copolymers in nanotechnology.[16-19]

1.3 Design of nanoporous polymers from block copolymers

There are four standard methods to create nanoporous polymers by selectively removing one block from block copolymers: (i) ozonolysis; (ii) thermal treatmeat; (iii) UV irradiation; (iv) chemical etching. The different representative approaches are listed here chronologically.

The first nanoporous polymer prepared from an ordered block copolymer was demonstrated in 1988 by Lee et al.[20] A poly(4-vinylphenyl-dimethyl-2-propoxysilane)-*b*-polyisoprene-*b*-poly(4-vinylphenyl-dimethyl-2 propoxysilane) (poly(1)-*b*-PI-*b*-poly(1)) triblock copolymer was synthesized by living anionic polymerization. The block copolymer was cast into a thin film with thickness of around 20 μm. Poly(1) block was cross-linked by hydrolysis of the alkylsiloxane group, and PI block was removed via ozonolysis. The authors claimed that the obtained layered-like (lamellar) porous structure is similar to that of segregated microphase of the original block copolymer. Since then, ordered nanoporous polymers have attracted considerable attention, and numerous polymer architecture and etching methods have been developed. The method of removing PI was later generalized to ozonolysis of polydienes. A series of nanoporous polystyrene (PS) was prepared from PS-*b*-polydiene block copolymers.[21,22]

In 1993, Hedrick et al. reported the preparation of nanoporous poly(phenylquinoxaline) (PPQ) with spherical morphology.[23] The block copolymer precursors were either poly(methyl methacrylate)-*b*-PPQ-*b*-poly(methyl methacrylate) (PMMA-*b*-PPQ-*b*-PMMA) or poly(propylene oxide)-*b*-PPQ-*b*-poly(propylene oxide) (PPO-*b*-PPQ-*b*-PPO) prepared by condensation polymerization techniques. The phase separation was obtained, but the degree of order was low. Heating the block copolymers above the decomposition temperatures of the degradable blocks, PMMA or PPO, generated closed-cell voids. The obtained nanoporous PPQ had potential application for low dielectric constant materials.

In 1997, Liu et al. published work on the formation of nanoporous poly(2-cinnamoylethyl methacrylate) (PCEMA) with poly(acrylic acid) (PAA) cylindrical cavities from PCEMA-*b*-poly(*tert*-butyl acrylate) (PCEMA-*b*-P*t*BA).[24] The copolymer precursors were exposed to UV irradiation firstly to cross-link PCEMA phase. Then precursors were treated in a CH_2Cl_2 solution of trimethylsilyl iodide to hydrolyze *tert*-butyl groups. Poly(acrylic acid) was formed after the hydrolysis, and surprisingly pores were generated at the same time due to the leave of *tert*-butyl groups.

In 2000, Thurn-Albrecht et al. used PS-*b*-PMMA to render nanoporous PS.[25] A thin (1 μm) film of block copolymer was placed between two electrodes. Hexagonally packed PMMA cylinders standing perpendicularly to the surface of the thin film were obtained by electric field alignment. UV irradiation was employed to crosslink the PS block and etch the PMMA block. Acetic acid was used to wash the film after UV irradiation to give aligned nanopores in PS matrix.

In 2001, Zalusky et al. prepared nanoporous PS from PS-*b*-polylactide (PS-*b*-PLA) diblock copolymer.[26] The synthesis of the block copolymer precursor was accomplished by using a combination of anionic and ring-opening polymerization techniques. Films of the block copolymer with macroscopic thickness were placed in a water/methanol solution of sodium hydroxide at 65 °C for about one week. 65 °C is the temperature between two glass transition temperatures of PLA and PS. Selectively hydrolytic degradation of PLA block can be completed after one week. This etching method offers the possibility of the preparation of monolithic nanoporous polymers.

In 2003, Ndoni et al. reported the preparation of nanoporous PS with bicontinuous gyroid morphology or body-centered cubic spheres morphology from PS-*b*-polydimethylsiloxane (PS-*b*-PDMS) block copolymers, which were synthesized by sequential anionic polymerization.[27] Films of the block copolymer with 0.5 mm thickness were placed in anhydrous hydrogen fluoride (HF) at 0 °C for 2 hours. Selective and quantitative cleavage of PDMS block was confirmed by NMR, SEC and XPS analyses. Later a less harmful etching agent, tetrabutyl ammonium fluoride (TBAF) was also used at room temperature to remove PDMS block from PI-*b*-PDMS block copolymers.[28,29]

More details about the development of nanoporous polymers derived from block copolymers can be found in two reviews by Hillmyer.[12,30]

1.4 Potential applications of nanoporous polymers

During last two decades, tremendous number of articles discussing potential applications of nanoporous polymers have been published. Here most representative and exciting works are presented.

Templates for nano objects. Nanoporous polymers with well oriented periodic arrays derived from block copolymers can be used as templates for synthesizing nanostructured materials. Pore size, pore distribution, pore shape and morphology of nanoporous polymers are important factors for growing nanostructured material with desired structures and properties. These factors can be controlled from design of block copolymer precursors, for example, by manipulating the block length, composition of blocks and even chemical structures of blocks.

One of the most cited papers in the field of nanoporous polymer templating (886 times so far) was by Thurn-Albrecht et al. The authors synthesized a PS-*b*-PMMA diblock copolymer by living anionic polymerization. This block copolymer has PMMA cylinders hexagonally packed in a PS matrix. By applying an electric field across a 1 μm thick polymer film, PMMA cylinders were oriented perpendicularly to electrodes. The PMMA block was degraded and the PS block was cross-linked by UV radiation. The degraded PMMA was then removed by acetic acid. The resulting nanopores with diameter of 14 nm were then filled with cobalt by electrodeposition (see Figure 1. 4). The Co nanowires with a length of about 500 nm were grown in the pore. This magnetic nanowire array shows promise for use as ultrahigh-density recording media (approaching one terabit per square inch).[25]

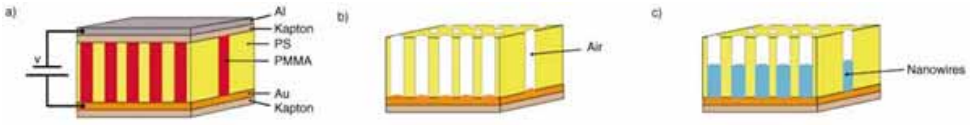

Figure 1.4 Schematic of high-density nanowire formation. (a) PS-*b*-PMMA diblock copolymer is annealed above the glass transition temperature of the copolymer between two electrodes under an applied electric field, (b) after removal of the minor component, the PMMA block, a nanoporous PS is formed, (c) nanowires are formed by electrodeposition in the pores.[25]

An ordered bicontinuous gyroid TiO_2 network was generated by using nanoporous poly(4-fluorostyrene) (P4FS) as a template. The obtained TiO_2 network with back-filled organic hole transporting materials formed a dye-sensitized solar cell and 1.7% power conversion efficiency could be reached.[31] The continuous connectivity of all electronically active phases to the device electrodes is particularly crucial for the performance of solar cell. This can be fulfilled by bicontinuous gyroid structure provided by self-assembly of block copolymers. The gyroid morphology has monodisperse pore diameters in which all channels and struts are fully interconnected. Edward et al. synthesized P4FS-*b*-PLA diblock copolymer with gyroid structure. The block copolymer was coated on conductive fluorine-doped tin oxide (FTO) glass substrates. The PLA block was etched in a base solution. TiO_2 was subsequently deposited in the nanoporous P4FS template via anodic oxidative hydrolysis of aqueous $TiCl_3$ by electrochemistry. Afterwards, calcination at 500 ºC lead to crystallization of TiO_2 as well as removal of the P4FS template. Absorption of Ru dyes onto the TiO_2 network and infiltration of a hole conducting material into the TiO_2 network made it ready for assembly of a solar cell.[31] (see Figure 1.5)

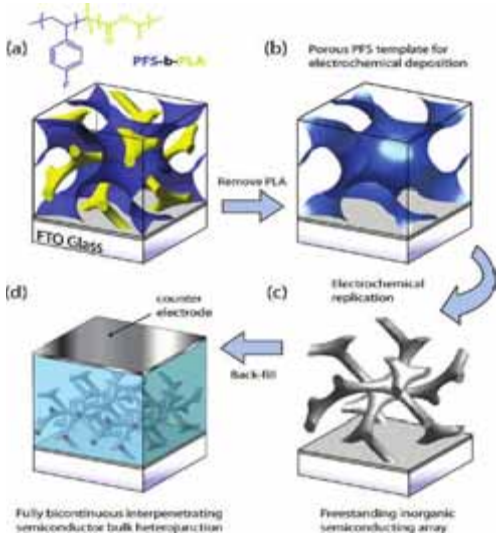

Figure 1.5 Schematic representation of assembly of hybrid solar cells from nanoporous gyroid templates. (a) P4FS-*b*-PLA film with gyroid morphology on a glass substrate with transparent conducting oxide coating (FTO glass). (b) nanoporous P4FS gyroid template and electrochemical replication. (c) freestanding gyroid TiO_2 network after removal of the P4FS template. (d) back-filling of the array hole transporting material and capping with a suitable counter electrode.[31]

Separation membranes. Separation with membranes has low energy consumption, high efficiency, and good transport selectivity and does not require additives compared to other conventional separation techniques, such as distillation, crystallization, and centrifugation. Owing to their controlled pore size, narrow pore size distribution, and high order functionality, nanoporous polymers from block copolymer precursors are ideal candidates or models for separation and filtration applications.

Liu et al. prepared a P*t*BA-*b*-PCEMA diblock copolymer with densely hexagonal packed P*t*BA cylinders inside the PCEMA matrix.[32] After UV crosslinking of PCEMA, the *tert*-butyl groups of P*t*BA were hydrolyzed with CH_2Cl_2 solution of trimethylsilyl iodide, leaving hydrophilic poly(acrylic acid) chains in the packed nanometer-sized cylinders. The resulting nanoporous polymers showed selective permeability of water depending on pH. At both low (1-2) and high (13) pH the membrane had high water permeability, while at intermediated pH values (3-6), the membrane exhibited permeability with several orders of magnitude lower. The authers explained that the observed water permeability variation may be caused by the PAA gel formation changes with pH.

In 2006, Yang et al. demonstrated the preparation of nanoporous membranes with ultrahigh selectivity and flux from block copolymer precursors for the separation of viruses.[33] Instead of pure block copolymers, a mixture of PS-*b*-PMMA diblock copolymer with PMMA homopolymer was employed to have cylindrical PMMA microdomains oriented perpendicular to the surface in the film. After selectively removing PMMA phase with acetic acid, a well-ordered array consisting of about 15 nm diameter pores was created. As shown in Figure 1.6, the membrane completely prevented the HRV14 virus (colored green) with a size of about 34 nm from penetrating into the pores, while proteins, such as bovine serum albumin (colored yellow) with a size of about 7.2 nm, could pass freely through the pores in the membrane.

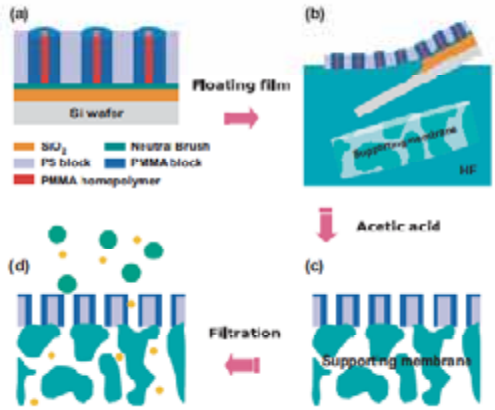

Figure 1.6 Schematic depiction of the procedure for the fabrication of asymmetric nanoporous membranes.[33]

Szewczykowski used nanoporous 1,2-polybutadiene (1,2-PB) as membranes to separate polymers with different sizes. [34] The nanoporous 1,2-PB was prepared from block copolymer 1,2-PB-*b*-PDMS by cross-linking the 1,2-PB block and etching the PDMS block. The specific cross-linking temperature of 140 ºC was chosen to obtain bi-continuous gyroid morphology for the membrane. Average pore diameter was around 14 nm. A solution of poly(ethylene glycol) (PEG) with molecular weight of 1, 10 and 230 kg/mol in methanol/water (80/20 v%) was used as pressed through the nanoporous membrane. The results shown in Figure 1.7 suggested that the membrane is only permeable for PEG with molecular weight of 1 kg/mol.

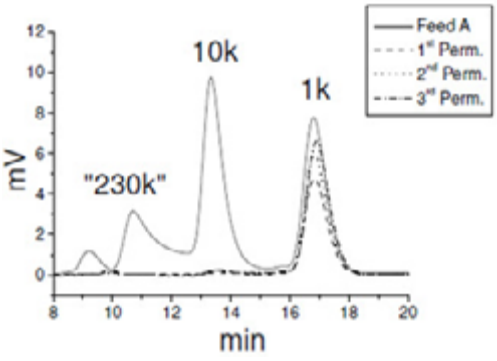

Figure 1.7 Size exclusion chromatography results of filtration of PEG with different sizes by nanoporous 1,2-PB membrane.[34]

Ultra-low dielectric constant materials. Ultra-low dielectric constant materials are known to decrease power dissipation, lower cross-talk noise, and reduce resistance–capacitance (RC) delays when incorporated in device systems.[35] Nanoporous polymers with uniform pore size distribution are attractive for preparing ultra-low dielectric constant materials.

Fu et al. described the generation of ultra-low dielectric constant materials from nanoporous poly(pentafluorostyrene) (PPFS).[36] PPFS-*b*-PMMA diblock copolymers were first synthesized by ATRP. PPFS matrix with closed spheres of PMMA inside was obtained. The copolymer film was exposed to UV radiation to selectively etch PMMA block, leaving porous films with pore diameters of 30 – 50 nm. The resulting nanoporous PPFS exhibits a dielectric constant of about 1.8, while the dielectric constant of a pristine PPFS film was about 2.2.

Bucholz et al. also managed to fabricate nanoporous PPFS with hexagonal cylinder morphology for ultra-low dielectric constant materials.[37] The block copolymer precursors in this case were PPFS-PLA. The PLA block was removed by acid-catalyzed hydrolysis. The resulting dielectric constant with a range from 1.6 to 1.9 was obtained for nanoporous PPFS films.

Liquid-core waveguides. Another potential application of nanoporous polymers is in design of liquid-core waveguides. Ndoni et al. demonstrated a methodology by combination of molecular self-organization as a bottom-up procedure for the production of nanoporous polymers with UV patterning as a top-down procedure for changing the chemical composition of the concentrated polymer-air interface to create liquid-core waveguides. 1,2-PB-*b*-PDMS diblock copolymers were synthesized by living anionic polymerizations. Hydrophobic nanoporous 1,2-PB could be rendered by cross-linking the PB block with dicumyl peroxide (DCP) and selectively etching the PDMS block with TBAF. Hydrophilic pore cavities were obtained by exposing nanoporous 1,2-PB films to UV radiation. By utilizing appropriate masks on the films, patterning of hydrophilic regions into hydrophobic 1,2-PB surroundings was realized. When submerged into water nanoporous films wet exclusively the irradiated zones. The added water increases the refractive index in the hydrophilic regions from 1.30 (dry state) to 1.43 (wet state). The refractive index contrast between the water-filled regions and hydrophobic regions allows light guiding at total internal reflection.[38] (see Figure 1.8)

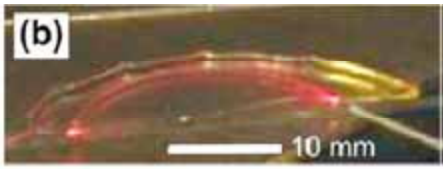

Figure 1.8 Demonstration of principle of 630 nm laser light guiding along a wet nanoporous zone.[38]

1.5 Synthesis of block copolymers

In order to achieve well-defined phase separations from block copolymers, low polydispersity and controlled molecular weight are two of the prerequisites. Living/controlled polymerization techniques are able to produce polymers with predictable molecular weight and narrow molecular weight distribution. They include as previously mentioned (see page 4) mainly living anionic polymerization, living cationic polymerization, ATRP, NMRP, RAFT and ROMP. In this thesis, living anionic polymerization and ATRP were applied to synthesize polymers, so herein I only introduce these two polymerization techniques.

Living anionic polymerization. Anionic polymerization is widely used to synthesize linear homopolymers, block copolymers, star polymers and polymers with other more complex architectures since the initial discovery by Szwarc.[39] The principle of anionic polymerization is outlined in Scheme 1.1. An anionic polymerization starts with a reaction of a monomer with an initiator capable of forming carbanion or an element with a negative ion. This first step is called initiation. The most used initiators are the alkyllithiums due to their high electronegativity, high ionization potential and small radius.[40] The amount of active initiators determines the number of polymer chains. Then reaction of this group with another monomer molecule results in the formation of a covalent bond, and simultaneously regenerates the negatively charged ion on the newly added molecule. Such a repetitive covalent bonding of the monomer to the active end group produces a growing polymer chain. This repetitive growing step is called propagation. The monomers must form stable carbanionic species under the polymerization conditions. The double bonds of the monomer should have the substituents which can stabilize the negative charge by charge withdrawing.[41] When the active end group is disappeared by reacting with a positively charged compound, the polymer chain will stop propagating, hence termination occurs. Depending on what kind of functional end group is desired, corresponding terminator can be chosen.

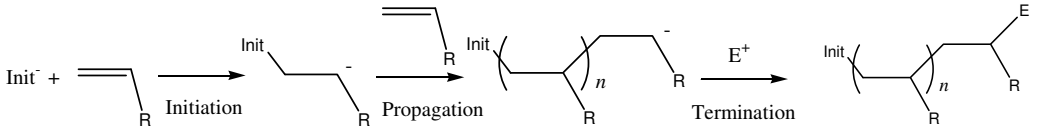

Scheme 1-1. The general scheme for anionic polymerization

To keep the "living" property, there are several conditions which must be kept in mind: i) the rate of chain initiation should be much faster than the rate of chain propagation; ii) chain termination should be absent; iii) chain transfer reactions should be avoided; iv) all the 'living' polymer chain ends have equal reactivity.[42] Therefore reactive initiator and strictly dry and oxygen-free conditions are necessary during polymerizations. Both high vacuum[41] and inert atmosphere[43] techniques have been successfully used for anionic polymerization. Overpressure inert (Ar) atmosphere is employed in this thesis to synthesize polymers, because in comparison with high vacuum technique, it is simpler and faster to prepare polymers with larger quantities by inert atmosphere technique.

For synthesis of block copolymers, the "living" chain end of the polymer A can also be used to initiate polymerization of a secondary monomer B, then an AB diblock copolymer can be prepared by sequential addition of monomers. Furthermore, ABC triblock and ABCD tetrablock copolymers can also be prepared in such addition manner. However, the order of monomer addition must be paid attention, because the reactivity of different monomer to a specific anionic chain end can be varied significantly. If the "living" chain end of polymer A is not basic enough to add to a secondary monomer B, crossing over to monomer B and starting propagation of monomer B is not possible. For example, it is very difficult to synthesize subsequent block onto poly(ethylene oxide) PEO block by anionic polymerization, because the oxy anion of the 'living' PEO chains has relative lower nucleophilicity compared to carbanions of other 'living' polymer chains.[44] In order to overcome the restriction on order of block in anionic polymerization, other 'living' polymerization methods have been introduced. For instance, ATRP has been combined with anionic polymerization to synthesize ABC and ABA triblock copolymers with PEO as a middle B block.[44,45]

ATRP. The mechanism of ATRP is very different from that of living anionic polymerization. ATRP is based on the principle of reversible activation-deactivation cycles in which a halide group emigrates fast between the growing polymer chain and transition metal complex. The general scheme for ATRP is shown in Scheme 1-2. Most ATRP reactions require the addition of four

components: (i) a initiator with at least one transferable atom (X); (ii) a transition metal (Mt^n) that can catalyze a reversible redox process; (iii) a ligand (L) that forms a complex with the transition metal and controls solubility of the complex in the reaction mixture; and (iv) one or more radically polymerizable monomers.[46] Polymer chains (P_n^*) are generated by the addition of the intermediate radicals to monomers with the rate constant of propagation (k_p) in a reversible redox reaction.

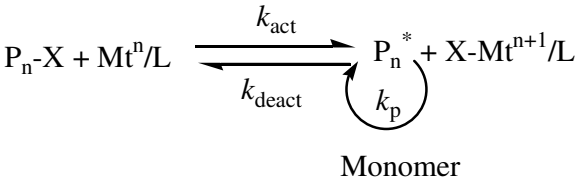

Scheme 1-2. Transition-Metal-Mediated ATRP[46]

The fast initiation and rapid reversible deactivation are necessary to control the polymer growth. Similar to anionic polymerization, the amount of the initiator determines the number of initiation chains in ATRP. Alkyl halides (R-X) are typically used as initiators in ATRP. Catalyst is very important in ATRP, because it determines the position of the atom transfer equilibrium and the dynamics of exchange between the dormant and active species.[47] A variety of transition metal complexes have been applied in ATRP, like copper, chromium, rhenium and iron halides. Most transition metal catalysts can not dissolve well in organic solvents. To increase the solubility of these metal catalysts in a relatively non-polar media, ligands normally are added. Another advantage of adding ligands is to adjust the atom transfer dynamics.[47] Nitrogen ligands are the most common used in ATRP. Many vinyl monomers, such as styrenes, (meth)acrylates, (meth)acrylamides and acrylonitrile are suitable for ATRP. All of these monomers contain a substituent on the α-carbon stabilizing the growing radicals through resonance or induction.

ATRP has two different routes to prepare block copolymers. One is sequential monomer addition technique like in anionic polymerization. When the polymerization of first monomer reaches a high conversion (92-95% in a solution polymerization), the second monomer is added. The other one is using macroinitiators. The presence of an activated alkyl halide at a polymer chain end enables to perform ATRP of another monomer. And the polymer with such kind of alkyl halide at the end is so called a macroinitiator. A macroinitiator can be synthesized by the same method, ATRP, or

initiating groups for ATRP can be inserted in polymers prepared by other methods. The advantage of this method for synthesis of block copolymers is that the first block can be fully characterized prior to the adding of the second block.

Surface-initiated ATRP is an attractive technique to modify surfaces by grafting functional polymer moieties. Once ATRP initiators are immobilized on the surface, the grafted polymer composition, molecular weight and polymer architecture can be controlled.

Click chemistry. Click chemistry was employed in the thesis in order to introduce functionality onto pore walls, but its suitability to design functional (block co) polymers will be mentioned below too. Click reactions, including the 1,3-dipolar azide – nitrile cycloaddition, 1,3-dipolar azide-alkyne cycloaddtion, Diels –Alder cycloaddition, ring opening of epoxides and thiol-oxidative coupling, have mild reaction conditions, quantitative yields and high tolerance to a variety of functional groups. The 1,3-dipolar azide-alkyne cycloaddition originally described by Huisgen[48] has received the most attention in polymer chemistry since it was demonstrated by Meldal[49] and Sharpless.[50] The reaction rate of the azide-alkyne cycloaddition can be dramatically accelerated by Cu(I) catalysis to yield 1,4-disubstituted 1,2,3-triazoles at ambient temperature. The scheme for Cu(I)-catalyzed azide-alkyne cycloaddition (CuAAC) is shown in scheme 1-3.

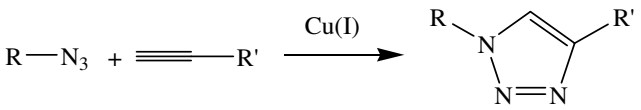

Scheme 1-3. General scheme for CuAAC

CuAAC has been employed to prepare a variety of dendrimers. Normally high monomer concentrations and many chromatographic separation procedures are needed for preparation of dendrimers. CuAAC is very suitable for dendrimer synthesis due to its high efficiency and simple purification. Using monomer containing alkyne and azide groups, dendrimers with well-defined structures can be prepared by CuAAC.[51,52] The combination of ATRP and CuAAC has been extensively used to prepare functional polymers. For example, various AB or ABC linear block copolymers have been prepared by coupling azide- and alkyne-terminated polymers by CuAAC, and these azide- or alkyne- functionalized polymers can be synthesized by ATRP prior to click chemistry.[53-55] Star polymers synthesized by combination of ATRP and CuAAC has also been

reported. Azido-telechelic polymers were coupled with the bi, tri, and tetravalent alkynes respectively to form star-type polymers respectively.[56] Furthermore, due to the high reactivity in heterogeneous reaction system and the ease of implementation, CuAAC has also been widely used in surface science. Planar metal,[57] glass[58] and polymer substrates,[59,60] nanoparticles,[61] and carbon nanotubes[62] have been successfully modified by CuAAC. In order to conduct CuAAC, the azide or alkyne groups need to be attached to the surface. Depending on the nature of surface, various methods are used to immobilize the functional group. The subsequent click reaction can then provide a library of polymers to be grafted on the surface.

1.6 Characterization techniques

Attenuated total reflectance-Fourier transform infrared spectroscopy (ATR-FTIR). ATR-FTIR is a routine analytical technique to investigate the chemical compositions of synthesized polymeric materials in the thesis. ATR-FTIR is the method of IR spectroscopy, which is a well-known and widely used tool to identify the structure of organic compounds and chemical functionalities. The term “infra red” covers the range of the electromagnetic spectrum between 0.78 and 1000 μm, but only the range from 2.5 to 25 μm is of interest in polymer science. All molecules have a certain amount of energy distributed throughout their structure. The amount of energy a molecule contains is quantized. That means, the vibration only occur at a specific frequency. When a molecule is irradiated with electromagnetic radiation, energy is absorbed if the frequency of the radiation matches the frequency of the vibration. Since each frequency absorbed by a molecule corresponds to a specific molecular vibration, the corresponding types of bonds in the compound can be found. Therefore, IR spectroscopy can result in a qualitative analysis of materials. In addition, the intensity of absorption in the IR spectrum is proportional to the amount of the material present, which makes it possible to carry out a quantitative analysis.

FTIR is a technique that employs an optical device called interferometer to guide IR beam and measure all of the infrared frequencies simultaneously. The measured signal is a so called interferogram, which can be converted to a frequency spectrum by performing a Fourier transformation on the signal date.

Traditionally IR spectrometers have been used to analyze materials by means of transmitting the IR radiation directly through the sample. There are many challenges on sample preparation and

spectral reproducibility by this transmission method.[63] An ATR-FTIR allows measuring the totally internally reflected infrared beam when the beam contacts with a sample (see Figure 1. 9) An IR beam travels into a crystal, which normally is a diamond, at a certain angle. An evanescent wave can be generated by this internal reflectance. When the sample absorbs energy, the wave will be attenuated. The wave with attenuated energy passes to the detector in the IR spectrometer and generates a spectrum. A few μm in the surface of the sample can be detected by ATR-FTIR, so the sample must have a good contact with the crystal surface.

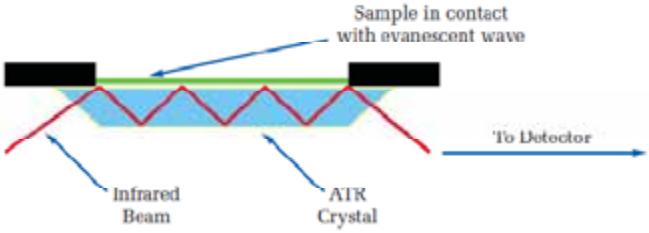

Figure 1.9 Schematic depiction of an ATR-FTIR system.[63]

Small angle scattering techniques. Small angle X-ray (SAXS) and neutron (SANS) scattering techniques are heavily used in this thesis to study the structural features of block copolymers and corresponding nanoporous polymers. SAXS and SANS together with small-angle light scattering (SALS) form a family of small-angle scattering with the collection of scattered waves at very low angles. The principle of the scattering by these three techniques is the same: interaction of radiation with matter. The difference is scattering of x-rays is caused by differences in electron densities between different molecular substances in the matter, scattering of neutrons is caused by differences in scattering power of different nuclei and scattering of light is caused by differences in refractive index. The information about size, shape and orientation of components of the sample can by obtained through the scattering results. The typical length scale of structure investigated by SAXS and SANS ranges from a few to several hundred nanometers, while the length scale probed by SALS is larger than one hundred nanometers. The intricate structures of block copolymers usually show a dimension in the range of 1-100 nm, which is ideal to be studied by SAXS and SANS.

One of the fundamental equations for SAXS and SANS is the Bragg's law:

$$2d \sin\theta = n\lambda \qquad (1.1)$$

where d is the characteristic repeat distance of a structure, θ is the scattering angle, n is an integer, and λ is the radiation wavelength.

The equation of scattering wave vector can be expressed as:

$$|q| = \frac{4\pi}{\lambda}\sin(\theta/2) \qquad (1.2)$$

Substituting the Equation 1.2 to 1.1 yields the following expression:

$$d = (\frac{2\pi}{|q|}) \cdot n \qquad (1.3)$$

The spatial correlations in the sample can be revealed by SAXS and SANS measurements. An illustration of a SAXS setup and examples of 1D and 2D collected scattering profiles are shown in Figure 1.10. Before the X-ray beam is directed at a sample, the divergent X-ray source is aligned into a fine focused beam through monochromating optics and pinholes in a collimator. Some of the incident beam is scattered by the sample, some is absorbed and some is transmitted. The scattered and transmitted beam pass through a vacuum flight tube and then the scattered beam is collected by a 2D detector and the transmitted beam is absorbed by a beam-stop to avoid the damage of the detector. The recorded 2D scattering images can be azimuthally integrated to a 1D plot of intensity versus scattering wave vector. The principle of SANS instrument is very similar to the SAXS instrument. The resolution obtained from SAXS in general is much better than that obtained from SANS. For example, SAXS shows many more high-order Bragg reflections than SANS for ordered systems.[65] On the other hand, scattering contrast can be enlarged by deuterium labeling for SANS if electron density contrast of the investigated system is very small for SAXS.

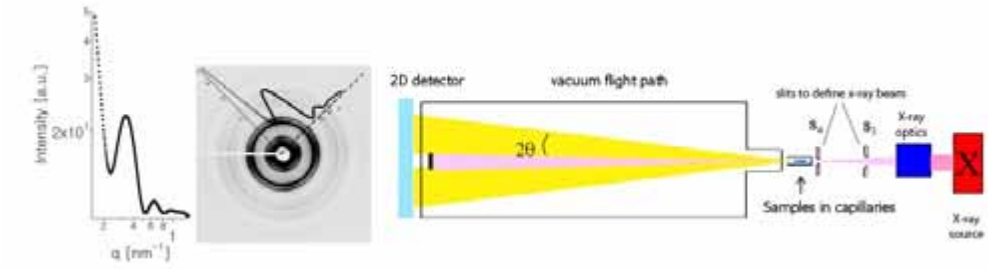

Figure 1.10 Schematic illustration of a SAXS instrument and examples of 1D and 2D SAXS profiles.[64]

Electron Microscopy. Electron microscopes are used to view objects on a very small scale, which can not be reached by light microscope. The resolution of the light microscope is limited due to the wavelength of the light. Since electrons have much smaller wavelength than visible light, much greater resolution can be obtained by electron microscopes. There are two main types of electron microscope: the scanning electron microscopy (SEM) and the transmission electron microscopy (TEM). Both SEM and TEM use electron gun to generate the electron beam. Samples are examined under vacuum in both microscopes.

In a SEM instrument (indicated in Figure 1.11), the electron beam with typical energy between 1 and 40 keV is focused to a size of 0.4 - 10 nm by condenser lenses. When the beam hits the sample surface, secondary electrons, backscattered electrons and X-rays can be emitted back out of the sample. The emission can be detected by specific detectors. By scanning the reflected beam across the surface of a sample an image can be generated. Unlike the SEM, the image is recorded by detecting the electrons passing though the sample and there are lenses after the sample to project a magnified image of the sample onto the imaging system in the TEM. Therefore the examined sample for TEM has to be extremely thin (less than half μm).

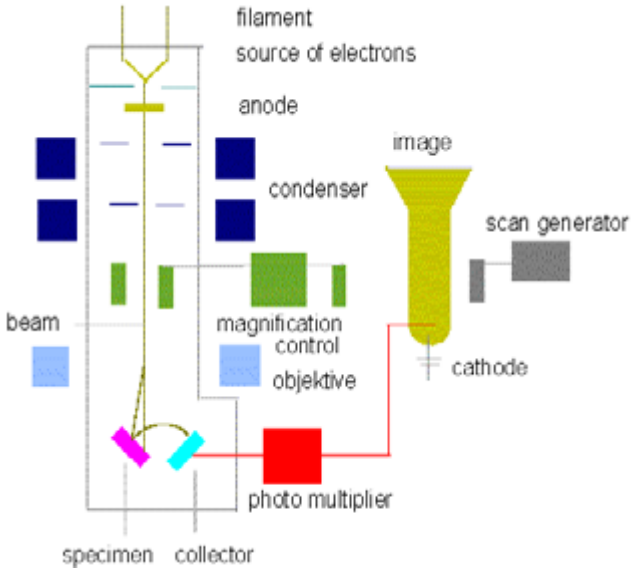

Figure 1.11 Schematic drawing of a SEM instrument.[66]

1.7 Thesis outline

The aim of this thesis was to prepare functional nanoporous polymers from block copolymer precursors. The thesis started with the preparation of nanoporous PS matrix with hydrophilic pores. Difficulty in film forming and low resistance to solvents limit the use of nanoporous PS in many applications. So emphasis of thesis was changed to cross-linked nanoporous 1,2-PB. Due to its good mechanical stability, reactive pendant double bonds and transparence, various functional nanoporous polymers were built based on nanoporous 1,2-PB. The following chapters contain:

Chapter 2 describes the preparation of nanoporous PS with hydrophilic PAA pores from di- and triblock copolymer precursors. The precursor material is either a poly(*tert*-butyl acrylate)-*b*-polystyrene (P*t*BA-*b*-PS) diblock copolymer synthesized by atom transfer radical polymerization (ATRP) or a polydimethylsiloxane-*b*-poly(*tert*-butyl acrylate)-*b*-polystyrene (PDMS-*b*-P*t*BA-*b*-PS) triblock copolymer synthesized by a combination of living anionic polymerization and ATRP. After deprotection of PtBA and degradation of PDMS by one-step operation, nanoporosity could be obtained. The chemical compositions and structures of resulting nanoporous polymers are investigated.

Chapter 3 presents the preparation of nanoporous 1,2-PB with different cross-linking degrees and different morphologies from 1,2-PB-*b*-PDMS diblock copolymer precursors. The cross-linking is required to improve the mechanical stability of the 1,2-PB matrix. Effect of cross-linking on structure and properties of nanoporous 1,2-PB is discussed. Different porous morphologies, such as hexagonally packed cylinders, gyroid and a metastable phase morphologies are obtained.

Chapter 4 focuses on the preparation of functional nanoporous 1,2-PB via surface-initiated ATRP and click chemistry. Two different methodologies for immobilizing ATRP monolith initiators are presented. Different functional polymer brushes, such as hydrophilic polyacrylates and proton conducting sulfonated polymers are grafted onto the pore walls of 1,2-PB by surface-initiated ATRP. Poly(ethylene glycol) with known chain length is clicked to the pore walls of 1,2-PB by click chemistry.

The topic of Chapter 5 is using nanoporous 1,2-PB as a scaffold to prepare conductive polymers. Polypyrrole, which is a conductive polymer, thin film is deposited on the pore walls of 1,2-PB by vapor phase polymerization. The electro activity of the modified nanoporous 1,2-PB is examined.

Chapter 6 extents the work from Chapter 3. A collapsed cross-linked 1,2-PB with gyroid morphology is prepared. It is found that the nanoporosity can be recovered when the collapsed 1,2-PB matrix is in the gel state. The possible application on load-release of chemicals for collapsed 1,2-PB is investigated.

Final Chapter 7 is the summary of the thesis work.

Appendix A describes the preliminary work on coupling primary amines onto the pore walls of 1,2-PB by UV irradiation.

Appendix B shows some interesting SANS results of nanoporous 1,2-PB, collapsed 1,2-PB and modified nanoporous 1,2-PB, and these results are not included in the chapters.

1.8 References

1. Rouquérol, J.; Avnir, D.; Fairbridge, C. W.; Everett, D. H.; Haynes, J. H.; Pericone, N.; Ramsay, J. D. F.; Sing, K. S. W.; Unger. K. K. *Pure Appl. Chem.* **1994**, *66*, 1739.

2. Jiang, D.; Zhao, H.; Zhang, S.; John, R. *J. Phys. Chem*. **2003**, *107*, 12774.

3. Zuttel, A. *Mater. Today* **2003**, *9*, 24.

4. Apel, P. *Radiation Measurements* **2001**, *34*, 559.

5. Weber, J.; Antonietti, M.; Thomas, A. *Macromolecules*, **2007**, *40*, 1299.

6. Zhu, X. X.; Banana, K.; Yen, R. *Macromolecules* **1997**, *30*, 3031.

7. Zhu, X. X.; Banana, K.; Liu, H. Y.; Krause, M.; Yang, M. *Macromolecules* **1999**, *32*, 277.

8. Zhang, H.; Cooper, A. I. *Adv. Mater.* **2007**, *19*, 1529.

9. Krause, B.; Sijbesma, H.J.P.; Munuklu, P.; van der Vegt, N. F. A.; Wessling, M. *Macromolecules* **2001**, *34*, 8792.

10. Chieng, T. H.; Gan, L. M.; Chew, C. H.; Ng, S. C. *Polymer* **1995**, *36*, 1941.

11. Zhou, N.; Bates, F.S.; Lodge, T.P. *Nano Letters*, **2006**, *6*, 2354.

12. Hillmyer, M. A. *Adv. Polym. Sci.* **2005**, *190*, 137.

13. Loge, T. P.; Bang, J.; Li, Z.; Hillmyer, M. A.; Talmon, Y. *Faraday Discuss.* **2005**, *128*, 1.

14. Bates, F. S.; Fredrickson, G. H. *Physics Today*, **1999**, *32*, 52.

15. Vigild, M. E.; Ndoni, S.; Mortensen, K. *Dansk Kemi*, **2004**, *11*, 32.

16. Park, C.; Yoon, J.; Thomas, E. L. *Polymer* **2003**, *44*, 6725.

17. Hamley, I. W. *Angew. Chem. Int. Ed.* **2003**, *42*, 1692.

18. Hamley, I. W. *Nanotechnology* **2003**, *14*, 39.

19. Sagalman, R. A. *Mater. Sci. Eng. R* **2005**, *48*, 191.

20. Lee, J.-S.; Hirao, A.; Nakahama, S. *Macromolecules* **1988**, *21*, 274.

21. Hashimoto, T.; Tsutsumi, K.; Funaki, Y. *Langmuir* **1997**, *13*, 686.

22. Park, M.; Harrison, C.; Chaikin, P. M.; Register, R. A.; Adamson, D. H. *Science* **1997**, *276*, 1401.

23. Hedrick J.L.; Labadie J.: Russell T.; Hofer D.; Wakharker V. *Polymer* **1993**, *34*, 4717.

24. Liu, G.; Ding, J.; Guo, A.; Herfort, M.; Bazett-Jones, D. *Macromolecules* **1997**, *30*, 1851.

25. Thurn-Albrecht, T.; Schotter, J.; Kastle, G. A.; Emley, N.; Shibauchi, T.; Krusin-Elbaum, L.; Guarini, K.; Black, C. T.; Tuominen, M. T.; Russell, T. P. *Science* **2000**, *290*, 2126.

26. Zalusky, A. S.; Olayo-Valles, R.; Taylor C. J.; Hillmyer, M. A. *J. Am. Chem. Soc.* **2001**, *123*, 1519.

27. Ndoni, S.; Vigild, M. E.; Berg, R. H. *J. Am. Chem. Soc.* **2003**, *125*, 13366.

28. Hansen, M. S.; Vigild, M. E.; Berg, R. H.; Ndoni, S.; *Polymer Bulletin* **2004**, *51*, 403.

29. Cavicchi, K. A.; Zalusky, A. S.; Hillmyer, M. A.; Lodge, T. P. *Macromol. Rapid Commun.* **2004**, *25*, 704.

30. Olson, D. A.; Cheng, L.; Hillmyer, M. A. *Chem. Mater.* **2008**, *20*, 869.

31. Crossland, E. J. W.; Kamperman, M.; Nedelcu, M.; Ducati, C.; Wiesner, U.; Smilgies, D. M.; Toombes, G. E. S.; Hillmyer, M. A.; Ludwigs, S.; Steiner, U.; Snaith, H. J. *Nano Letters* **2009**, *9*, 2807.

32. Liu, G.; Ding, J. *Chem. Mater.* **1999**, *11*, 2233.

33. Yang, S. Y.; Ryu, I.; Kim, H. Y.; Kim, J. K.; Jang, S. K.; Russell, T. P. *Adv. Mater.* **2006**, *18*, 709.

34. Szewczykowski, P. P. *Ph. D. Thesis*, Technical University of Denmark, DK-2800 Kgs. Lyngby, Denmark, **2009**.

35. Shamiryan, D.; Abell, T.; Iacopi, F.; Maex, K. *Mater. Today* **2004**, *7*, 34.

36. Fu, G. D.; Yuan, Z.; Kang, E. T.; Neoh, K. G.; Lai, D. M.; Huan, A. C. H. *Adv. Fun. Mater.* **2005**, *15*, 315.

37. Bucholz, T. L.; Li, S. P.; Loo, Y. L. *J. Mater. Chem.* **2008**, *18*, 530.

38. Ndoni, S. ; Li, L.; Schulte L.; Szewczykowski, P. P.; Hansen, T. W.; Guo, F.; Berg, R. H.; Vigild, M. E.; *Macromolecules*, **2009**, *42*, 3877.

39. Zwarc, M. *Nature* **1956**, *178*, 1168.

40. Rundle, R. E. *J. Phys. Chem.* **1957**, *61*, 45.

41. Hadjichristidis, N.; Iatrou, H.; Pispas, S.; Pitsikalis, M. *J. Polym. Sci. Part A: Polym. Chem.* **2000**, *38*, 3211.

42. Morton, M. *Anionic Polymerization: Principles and practices*, Academic Press, **1983**.

43. Ndoni, S.; PaPadakis, C. M.; Bates, F. S.; Almdal, K. *Rev. Sci. Instrum.* **1995**, *66*, 1090.

44. Mahajan, S.; Cho, B. K.; Allgaier, J.; Fetters, L.; Coates, G.; Wiesner, U. *Macroml. Rapid Commun.* **2004**, *25*, 1889.

45. Jankova, K.; Chen, X.; Kops, J.; Batsberg, W. *Macromolecules* **1998**, *31*, 538.

46. Coessens, V.; Pintauer, T.; Matyjaszewski, K. *Prog. Polym. Sci.* **2001**, *26*, 37.

47. Matyjaszewski, K.; Xia, J. *Chem. Rev.* **2001**, *101*, 2921.

48. Huisgen, R. *Angew. Chem., Int. Ed.* **1963**, *2*, 565.

49. Tornoe, C. W.; Christensen, C.; Meldal, M. *J. Org. Chem.* **2002**, *67*, 3057.

50. Rostovtsev, V. V.; Green, L. G.; Fokin, V. V.; Sharpless, K. B. *Angew. Chem., Int. Ed.* **2002**, *41*, 2596.

51. Joralemon, M. J.; ONReilly, R. K.; Matson, J. B.; Nugent, A. K.; Hawker, C. J.; Wooley, K. L. Macromolecules **2005**, *38*, 5436.

52. Wu, P.; Feldman, A. K.; Nugent, A. K.; Hawker, C. J.; Scheel, A.; Voit, B.; Pyun, J.; Frechet, J. M. J.; Sharpless, K. B.; Fokin, V. V. *Angew. Chem. Int. Ed.* **2004**, *43*, 3928.

53. Opsteen, J. A.; van Hest, J. C. M. *Chem. Commun.* **2005**,*1*, 57.

54. Opsteen, J. A.; van Hest, J. C. M. J. *Polym. Sci., Part A: Polym.Chem.* **2007**, *45*, 2913.

55. Quemener, D.; Davis, T. P.; Barner-Kowollik, C.; Stenzel, M. H. *Chem. Commun.* **2006**, *48*, 5051.

56. Gao, H.; Matyjaszewski, K. *Macromolecules* **2006**, *39*, 4960.

57. Lee, J. K.; Chi, Y. S.; Choi, I. S. *Langmuir* **2004,** *20*, 3844.

58. Sun, X. I.; Stabler, C. I.; Cazalis, C. S.; Chaikof, E. L. *Bioconjug. Chem.* **2006**, *17*, 52.

59. Bakbak, S.; Leech, P. J.; Carson, B. E.; Saxena, S.; King, W. P.; Bunz, U. H. F. *Macromolecules* **2006**, *39*, 6793.

60. Daugaard, A. E.; Hvilsted, S.; Hansen, T. S.; Larsen, N. B. *Macromolecules*, **2008**, *41*, 4321.

61. Fleming, D. A.; Thode, C. J.; Williams, M. E. *Chem. Mater.* **2006**, *18*, 2327.

62. Li, H.; Cheng, F.; Duft, A. M.; Adronov, A. *J. Am. Chem. Soc.* **2005**, *127*, 14518.

63. Technical note, FT-IR spectroscopy, PerkinElmer.

64. http://www.mrl.ucsb.edu/~safinyaweb/XRD.htm.

65. Mortensen K. *Structural Studies of Polymer Systems Using Small-Angle Neutron Scattering*. **2001**, Gordon & Breach Science Publishers.

66. Lecture slides, Department of materials, University of Oxford.

Chapter 2 Nanoporous PS with Hydrophilic Pores from Di- and Triblock Copolymers

2.1 Introduction

Since the first nanoporous material preparation from an ordered block copolymer by Lee et al. in 1988,[1] a number of nanoporous polymers (NPs) with hydrophobic cavities have been described. However, many possible applications such as drug delivery, growth of bacteria, and selective separation will require the NPs to work in an aqueous environment. Due to the limitation of available polymer synthesis and the nanoscale confinement of the porous cavities, only a limited number of NPs with hydrophilic pores have been prepared to date. Liu and co-workers reported the preparation of nanoporous films from poly(2-cinnamoylethyl methacrylate)-*b*-poly(*tert*-butyl acrylate) (PCEMA-*b*-P*t*BA) and polyisoprene-*b*-poly(2-cinnamoylethyl methacrylate)-*b*-poly(*tert*-butyl acrylate) (PI-*b*-PCEMA-*b*-P*t*BA)/P*t*BA polymer blend. In both cases PCEMA was cross-linked by UV irradiation. The P*t*BA homopolymer was extracted in dichloromethane and the *tert*-butyl groups in the copolymer were hydrolyzed in a dichloromethane solution of trimethylsilyl iodide followed by a methanol/water solution either in a two-pot or a one-pot procedure.[2,3] Hillmyer and co-workers prepared nanoporous polystyrene-*b*-poly(ethylene oxide) (PS-*b*-PEO) by treating PS-*b*-PEO/polystyrene-*b*-polylactide (PS-*b*-PLA) polymer blends in a sodium hydroxide water/methanol solution, which lead to cleavage of the PLA component.[4] In 2005, Hillmyer and his co-workers proposed a new strategy for obtaining such nanoporous polymers based on ABC triblock copolymers. An ABC triblock copolymer that forms a cylindrical morphology contains A block which is a mechanical stable matrix, hydrophilic middle B block, and degradable C block. After selective etching of sacrificial C block, pores with hydrophilic B block "coating" can be generated. They obtained nanoporous polystyrene-*b*-poly(N,N-dimethylacrylamide) (PS-*b*-PDMA) by etching PLA block from PS-*b*-PDMA-*b*-PLA triblock copolymer.[5]

Inspired by Hillmyer's work, we prepared triblock copolymers of polystyrene, poly(*tert*-butyl acrylate), and polydimethylsiloxane (PS-*b*-P*t*BA-*b*-PDMS) by combined atom transfer radical and living anionic polymerizations. PDMS can be degraded by HF or TBAF, and P*t*BA can be hydrolyzed to render hydrophilic poly(acrylic acid) (PAA). Diblock copolymers of PS and P*t*BA

This part of the work has been published in *Macromolecules* **2008**, *41*, 1486.

(PS-*b*-P*t*BA) were also synthesized by ATRP, since pores could be formed as a result of removing *tert*-butyl groups which have 44% of the P*t*BA polymer mass. Both the strong acid - hydrogen fluoride (HF) and the weak acid - trifluoroacetic acid (TFA) were used separately to deprotect the *tert*-butyl ester groups and degrade PDMS, leaving the structurally and chemically intact PS matrix.

2.2 Synthesis of block copolymer precursors

PS-*b*-P*t*BA

The synthesis of P*t*BA-*b*-PS diblock copolymers through ATRP is outlined in Scheme 2-1. Ethyl 2-bromo propionate (2-EBP) was used as initiator for polymerizing *t*BA in bulk by ATRP. After purification, P*t*BA macroinitiator was used for the subsequent ATRP of styrene in xylene.

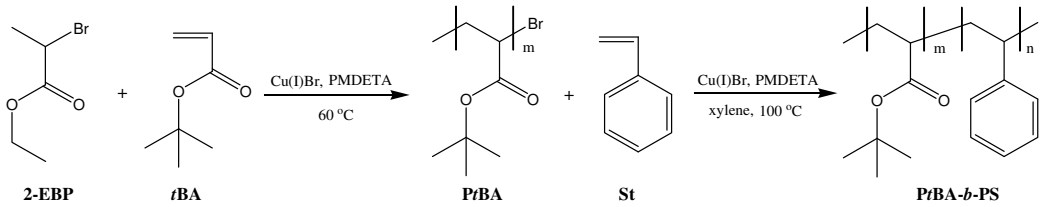

Scheme 2-1. Synthesis of P*t*BA-*b*-PS diblock copolymers by ATRP.

Here two P*t*BA-*b*-PS diblock copolymers are presented: AS-1 and AS-3. AS-1 has a number-average molecular weight M_n of 14.5 kg/mol, a polydispersity index (PDI) of 1.17, and mass fraction of P*t*BA of 0.54. AS-3 has a number-average molecular weight M_n of 25.0 kg/mol, a PDI of 1.20 and mass fraction of P*t*BA of 0.31. The molecular weight was determined by SEC and ^{1}H NMR, PDI was obtained from PS SEC calibration and mass fraction was calculated from ^{1}H NMR spectra. The same P*t*BA macroinitiator was used for both AS-1 and AS-3. The size exclusion chromatography (SEC) traces of P*t*BA, AS-1 and AS-3 are shown in Figure 2.1.

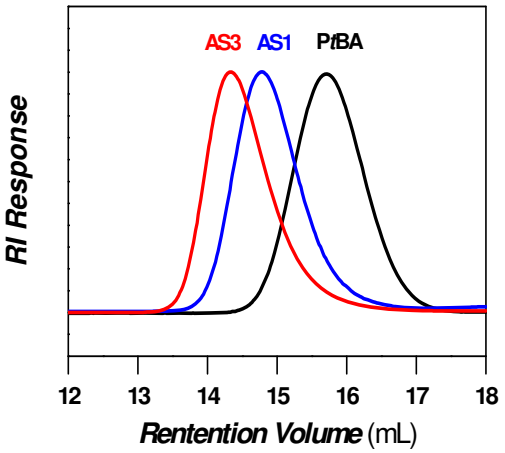

Figure 2.1. SEC traces of P*t*BA, AS-1 and AS-3.

Small angle x-ray scattering (SAXS) analysis of the annealed diblock copolymer samples revealed lamellar structure with average period of 25 nm in AS-1, and hexagonally packed cylindrical structure with principal spacing of 27 nm in AS-3.

PS-*b*-P*t*BA-*b*-PDMS

PDMS-*b*-P*t*BA-*b*-PS triblock copolymer was synthesized by a combination of living anionic polymerization and ATRP according to Scheme 2-2. PDMS macroinitiators for ATRP have previously been prepared by anionic polymerization.[6-8] Afterwards, a modified three-step procedure has been chosen. The product of living anionic polymerization of hexamethylcyclotrisiloxane (D_3) was end-capped with chlorodimethylsilane, as shown in reaction step ii of Scheme 2-2. The yielded **PDMS-H** was coupled with allyl alcohol in the presence of Karstedt's catalyst[9] (see reaction step iii in Scheme 2) producing PDMS with a hydroxyl end group (**PDMS-OH**). Further reaction with α-bromoisobutyryl bromide[10] turned the obtained **PDMS-OH** into a bromoisobutyrate PDMS (**PDMS-Br**), shown in reaction step iv. **PDMS-Br**'s role as a macroinitiator for ATRP is well documented.[6-8,10]

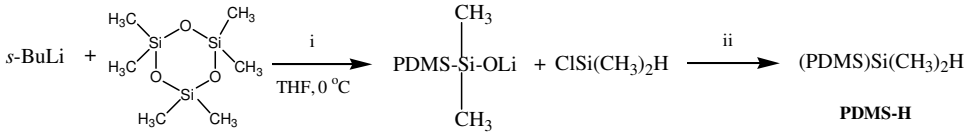

(Living anionic polymerization)

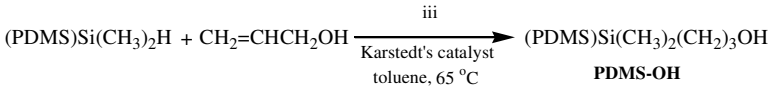

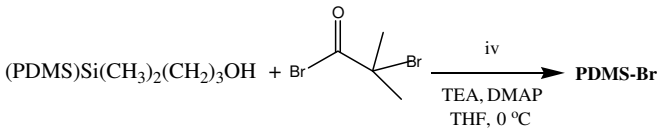

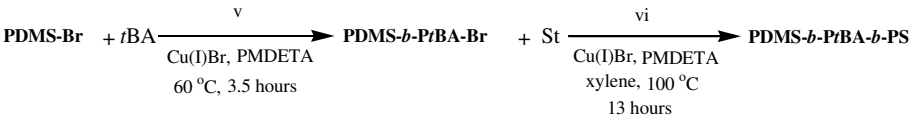

(ATRP)

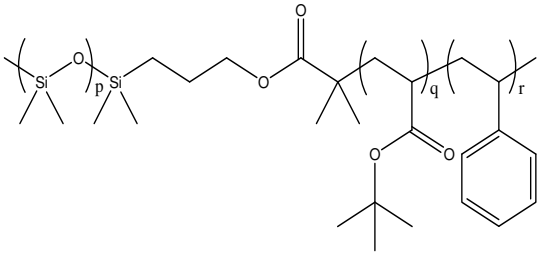

Scheme 2-2. Synthesis of PDMS-*b*-P*t*BA-*b*-PS Triblock Copolymer by a Combination of Living Anionic Polymerization and ATRP (Chemical Structure of the Final Triblock Copolymer Is Shown in the Last Row).

The complete conversion of the mentioned groups in the functional PDMS through each of the steps was evidenced by ^{1}H NMR, as shown in Figure 2.2. The characteristic Si-H proton peaks in the hydrosilyl end group of **PDMS-H** at 4.7 ppm were found to disappear, and a new resonance with the double relative intensity at 3.6 ppm appeared, corresponding to the CH_2 adjacent to the hydroxyl

unit in **PDMS-OH**. Furthermore, the signals for the CH_2 with the same relative intensity were shifted from 3.6 to 4.1 ppm as a result of replacing hydroxyl group by α-bromoisobutyryloxy group in the preparation of the macroinitiator. This is an indication of a virtually quantitative Si-H end group conversion to a brominated end group. As a direct check, the areas under the peaks *a* and *d* in the bottom panel of Figure 2.2 have the same value within the measurement accuracy. The group of peaks *a* represents the six methyl protons of the initiator and the peak *d* the six methyl protons of the Br-containing end group. In the top two spectra of Figure 2.2 the peaks at 3.7 and 1.8 ppm are from traces of THF in the polymer, and peaks around 3.5 and 1.6 ppm are caused by impurity of methanol and H_2O, respectively.

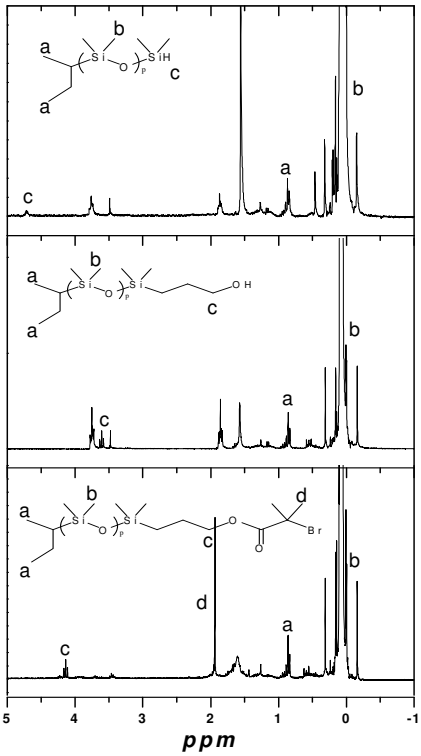

Figure 2.2. ^{1}H NMR spectra of PDMS-H (top), PDMS-OH (middle) and PDMS-Br (bottom).

The obtained **PDMS-Br** was used to consecutively polymerize *t*BA and St blocks by ATRP. The SEC traces illustrating increased molecular weight from the macroinitiator (trace *a*) to the diblock

(trace *b*) and finally to the triblock (trace *c*) are shown in Figure 2.3. The final PDMS-*b*-P*t*BA-*b*-PS triblock copolymer (DAS-1) has a number-average molecular weight *M*n of 59.5 kg/mol and mass fractions of PDMS, P*t*BA, and PS of 0.17, 0.16, and 0.67, respectively, as determined by ^{1}H NMR. A PDI of 1.29 relative to PS calibration was estimated by SEC. Hexagonally packed cylindrical morphology with domain spacing of 47 nm for DAS-1 sample was evidenced by SAXS measurement. The organization of PDMS and P*t*BA within the cylindrical domains of DAS-1 is assumed to be of core-shell type with PDMS occupying the core.

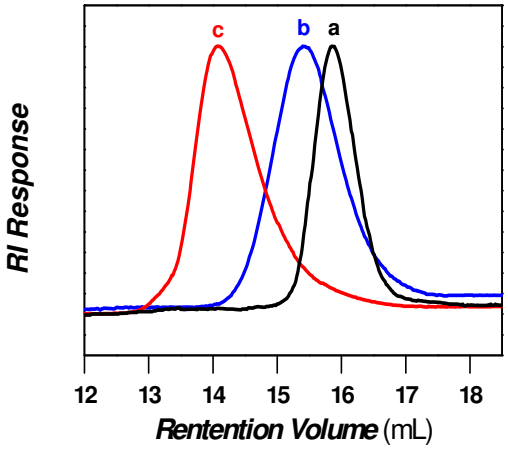

Figure 2.3. SEC monitoring the synthesis of triblock copolymer. (a) PDMS-Br (PDI= 1.08), (b) PDMS-*b*-P*t*BA (PDI =1.20), (c) PDMS-*b*-P*t*BA-*b*-PS (PDI =1.29).

The data on the molecular weight, molecular weight distribution and composition for the two P*t*BA-*b*-PS diblocks and the one PDMS-*b*-P*t*BA-*b*-PS triblock are summarized in columns 2-6 of Table 2.1. The structure and the characteristic spacings of the three block copolymers, as determined by SAXS, are shown in the last two columns of Table 2.1.

Table 2.1. Molecular and bulk morphological characteristics of the P*t*BA-*b*-PS and PDMS-*b*-P*t*BA-*b*-PS samples.

sample	M_n (NMR) (g/mol)	PDI (SEC)	w_{PS}	w_{PtBA}	w_{PDMS}	Morphology [a] (SAXS)	d_{SAXS} [b] (nm)
AS-1	14500	1.17	0.46	0.54	-	LAM	25
AS-3	25000	1.20	0.69	0.31	-	HEX	27
DAS-1	59500	1.29	0.67	0.16	0.17	HEX	47

[a] LAM-LAMellar, HEX- HEXagonally packed cylindrical structure. [b] Principal spacings d_{10} or lamellar spacing period d from SAXS.

2.3 Deprotection and etching

The use of HF as a PDMS degrading agent in block copolymers was first reported a few years ago.[11] HF quantitatively cleaves the Si-O bonds transforming them into Si-F bonds and was used to create nanoporous PS and polydiene materials.[11,12] Anhydrous HF is a strong protonating acid with acidity function (H_0) of about -11.[13] Our idea was to prepare a hydrophilic nanoporous material from a P*t*BA-*b*-PS diblock copolymer simply by deprotecting the P*t*BA block (i.e., creating PAA by cleaving the *tert*-butyl group). Obviously, the deprotection of P*t*BA should happen as a heterogeneous reaction in conditions of solid state (nonsolvent) for PS. HF successfully deprotected P*t*BA in both the P*t*BA-*b*-PS diblock and the PDMS-*b*-P*t*BA-*b*-PS triblock. Furthermore, the HF treatment also caused the already established degradation of PDMS in the case of the triblock copolymer. The deprotection reaction mechanism of P*t*BA by HF is expected to be a typical acidic deprotection for the case, involving a *tert*-butyl cationic intermediate and the final production of isobutylene.[14-16] *tert*-Butyl alcohol is also a possible byproduct in the presence of water liberated by the cleavage of the Si-O bonds.[11] Treatment by excess HF constitutes the first one-step route of fabrication of hydrophilic nanoporous PAA-*b*-PS.

The use of HF is hazardous and should only be undertaken following strict safety precautions.[11] A known route for acidic deprotection of P*t*BA is the use of anhydrous TFA in dichloromethane[17-19] or concentrated hydrochloric acid in dioxane.[20,21] The tentative treatment of the PDMS-*b*-P*t*BA-*b*-PS triblock copolymer with pure TFA (without any solvent) turned out to deprotect P*t*BA and simultaneously remove PDMS. The first interpretation of these results evokes acydolysis by TFA of

all the ester bonds in the triblock copolymer, including the chain-backbone ester bond connecting PDMS with PtBA (see the last line in Scheme 2-2). Yet, this ester bond is expected to be stable to TFA; therefore, at present we do not have a good explanation for the surprising quantitative removal of the PDMS block by TFA. Furthermore, and most surprisingly, we have experienced that TFA actually removes PDMS even from anionically prepared PS-*b*-PDMS and polybutadiene-*b*-PDMS block copolymers (data not shown), where the transition bond from the hydrocarbon to the PDMS block is expected to be a carbon-silicone bond. Treatment by excess TFA constitutes the second one-step route of fabrication of hydrophilic nanoporous PAA-*b*-PS.

Two instances were traced in the literature, reporting the combined use of TFA and PDMS. First, TFA has been described as a catalyst in cationic polymerization of cyclosiloxanes.[22,23] Second, DeSimone et al. used TFA with supercritical carbon dioxide to remove PDMS from a PS-*b*-PDMS block copolymer, which was prepared with a "weak" carbon-oxygen-silicone link between the blocks. The TFA was attributed to be able to cleave this link and the following treatment removed the PDMS.[24,25]

Our preliminary results hint to the use of TFA as a general PDMS-cleaving agent in block copolymers. The findings on the creation of hydrophilic nanoporous polymers are summarized in Scheme 2-3.

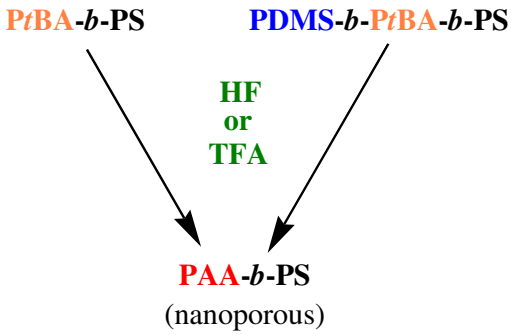

Scheme 2-3. Deprotection and etching of diblock P*t*BA-*b*-PS or triblock PDMS-*b*-P*t*BA-*b*-PS copolymers (by HF or TFA) creates nanoporous PAA-*b*-PS.

Within 1-5% the mass loss after acidolysis, as measured by the ratio $\Delta m/\Delta m_{max}$ between the observed mass loss and the maximal expected value, was consistent with either the fraction of *tert*-

butyl groups for diblock copolymer precursors (AS-1 and AS-3) or the fraction of its sum with the PDMS block for the triblock copolymer precursor (DAS-1).

Detailed information on the chemical composition changes for DAS-1 after HF and TFA treatments was acquired by the FT-IR spectra shown in Figure 2.4. Only the absorbance range of interest is presented in the figure. The spectrum of PDMS-*b*-P*t*BA-*b*-PS (DAS-1) shows absorption bands related to the PDMS: CH_3 bending, Si-O-Si stretching, and C-Si-C stretching peaks located at 1261, 1092-1088, and 800 cm^{-1}, respectively. C=O (ester) stretching peak at 1730 cm^{-1}, CH_3 (*t*Bu) bending peak at 1394/1368 cm^{-1}, C-C-O stretching (O*t*Bu) at 1259 cm^{-1}, and C-O (O-*t*Bu) stretching peak at 1151 cm^{-1} represent *tert*-butyl group in P*t*BA. The characteristic absorption peaks associated with PS are at 1489, 1454, 760, and 700 cm^{-1}. After deprotection and etching in HF for 2 h (DAS-1-HF), the characteristic peaks for PS remained intact, while the peaks related to PDMS (CH_3 bending and C-O stretching) and peaks originating from *tert*-butyl group disappeared entirely. The sharp peak (*a* in Figure 2.4) corresponding to the ester carbonyl group (C=O) was broadened after HF treatment due to the formation of carboxylic acid carbonyl group. The spectrum confirms that PDMS and *tert*-butyl groups were completely removed and PS was stable under HF treatment conditions. This shows that HF was also able to deprotect P*t*BA (yielding the hydrophilic PAA block) in addition to etching of PDMS. Identical chemical composition changes follow from TFA treatment (DAS-1-TFA) as shown in Figure 2.4. After HF treatment, both AS-1 and AS-3 samples exhibit the same change in IR spectra as DAS-1. Peaks for PS remained, peaks for *tert*-butyl group disappeared entirely and the sharp peak for ester carbonyl group was broadened. (data not shown)

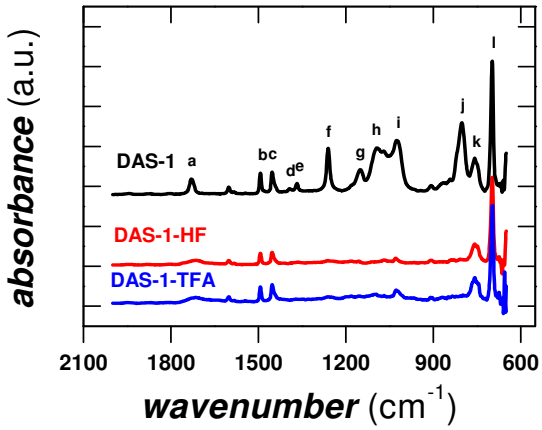

Figure 2.4. FT-IR spectra of DAS-1 precursor sample (top line), after HF treatment (middle line) or after TFA treatment (bottom line). Peaks are identified as follows: (a) C=O stretching (1730 cm^{-1}) in ester group, (b and c) CH stretching (1489 cm^{-1}, 1454 cm^{-1}) in monosubstituted phenyl group, (d and e) CH_3 bending (1394 cm^{-1}, 1368 cm^{-1}) in *t*Bu group, (f) CH_3 bending (1261 cm^{-1}) in Si-CH_3 and C-C-O stretching (1259 cm^{-1}) in O-*t*Bu, (g) C-O stretching (1151 cm^{-1}) in O-*t*Bu, (h to i) Si-O-Si stretching (1088-1092 cm^{-1}), (j) C-Si-C stretching (800 cm^{-1}) and (k and l) monosubstituted phenyl group (760 cm^{-1},700 cm^{-1}).

Figure 2.5 shows SAXS 1D profiles of AS-1, AS-3, and DAS-1 before and after degradation. DAS-1 was treated with TFA and HF, and both curves are shown in panel c of Figure 2.5. The ratios of scattering peak positions for the HF-treated samples were identical to those for the original diblock and triblock precursors. But the scattering intensity was significantly increased after HF or TFA treatment for all three samples, though at different degrees. This is due to an increased electron density contrast as a result of replacing the removed chain parts by vacuum. The SAXS data give evidence for the creation of nanoporous structures of the same morphologies as that of the respective diblock and triblock precursors. The nanoporous structures in more detail will be discussed in the following section.

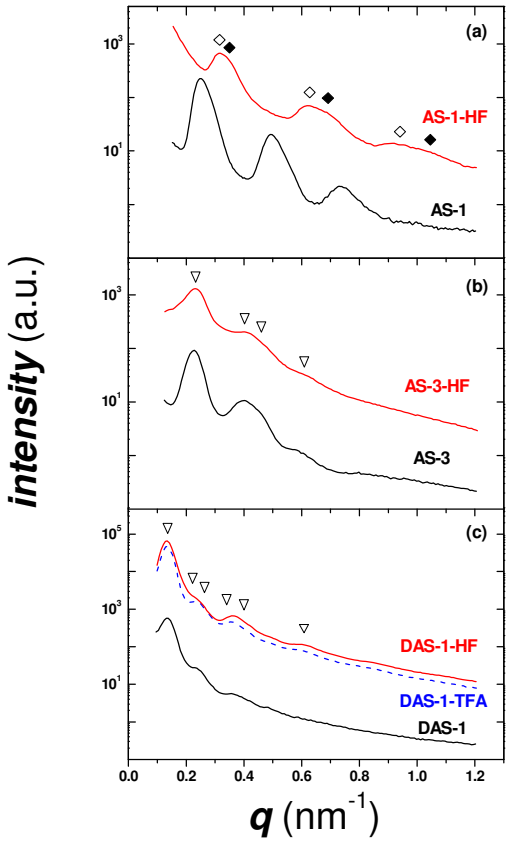

Figure 2.5. SAXS 1D profiles of (a) AS-1, (b) AS-3 and (c) DAS-1 before and after degradation. In panel (a) the expected reflections for a lamellar morphology are marked by diamonds (1:2:3) and in panels (b) and (c) some of the expected reflections for a hexagonally cylindrical morphology are marked by triangles ($1:3^{1/2}$: $4^{1/2}$:$7^{1/2}$:$9^{1/2}$:$21^{1/2}$). The filled diamonds in panel (a) mark the calculated q-scale for collapsed lamellae (see first paragraph of the **Nanoporous structures** section).

2.4 Nanoporous structures

The positions of the primary peak q^* for AS-3-HF, DAS-1-HF, and DAS-1-TFA after HF treatment or TFA treatment matches the positions of the primary peak before etching, as can be seen from Figure 2.5 b, c. These three samples all have cylindrical hexagonal morphology, which is invariant

to the deprotecting procedure because of the glassy state of the matrix formed by the majority block (PS). However, for the lamellar sample AS-1-HF the peak position is not invariant to the deprotection of the minority block. The position of the primary peak for AS-1-HF increased from 0.253 to 0.321 nm^{-1} as can be seen in Figure 2.5 a. This peak shift indicates that there was shrinkage of AS-1-HF during the degradation procedure. According to the incoherent scattering (at high q), the scattering contrast between AS-1-HF and AS-3-HF compared to their precursors are in the same order of magnitude, so we assume that both the etched samples have similar electron density profile although they are not of similar morphologies. The scattering peaks of AS-1-HF became broader and asymmetrical, which indicates that the lamellar morphology in the nanoporous AS-1-HF is not as well-defined as in the AS-1 precursor. This might be because there is no physical stabilizing spacer between the lamellar polymeric sheets, and the individual sheets of polystyrene can skew up a little and not be perfectly parallel, as illustrated in Figure 2.6.

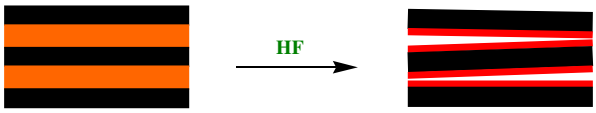

Figure 2.6. Schematic illustration of the lamellar structure in AS-1 before and after deprotection: - PS, - P*t*BA, - PAA. PS is thought to remain unchanged during HF-treatment. The P*t*BA (orange in the left panel) looses 44% by mass during HF-acydolysis, converting into PAA (red in the right panel). The generated free volume gives rise to inter-lamellar nanocavities in the dry state, but the lamella packing gains disorder as schematized in the right panel and discussed in the text.

For this reason the scattering peaks of AS-1-HF are expected to show a broad distribution of lamella spacing with the collapsed lamellae spacing as the lower boundary (marked by filled symbol in Figure 2.5 a), i.e., lamellae without real cavity in between, where the PAA chains from adjacent sheets overlap. Detailed information on electron density profiles that could be used to substantiate or reject such a possibility are currently missing. The position and width of the primary peaks were obtained by Lorentzian fit of each scattering profile.

The reason for the observed shrinkage of AS-1-HF could be related to the negative pressure generated by the urge of surface energy minimization and by the hydrogen bonds among the formed carboxylic acid groups. In the presence of water the major part of the shrinkage disappeared, as will be shown in the paragraph on water uptake.

In order to check the stability between the lamellar polymeric sheets for AS1 after degradation, one extreme case with shear aligned AS1 film was prepared. SAXS 1D profiles of shear aligned AS1 sample and one AS1 sample without shearing are shown in Figure 2.7. For the shear aligned AS1 sample, the X-ray beam is normal to the shear direction. No any structure features observed from scattering pattern from shear aligned sample indicates a good shear alignment.

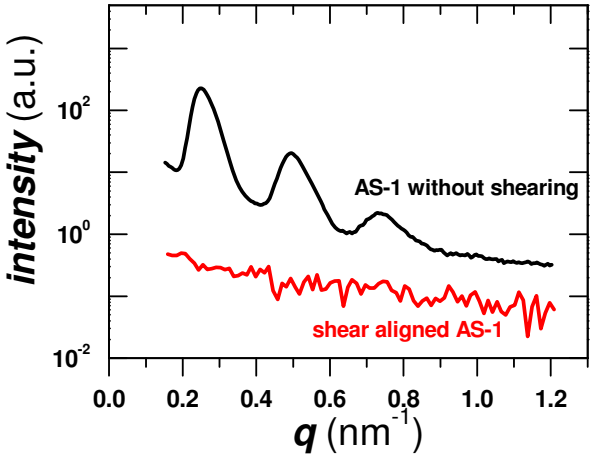

Figure 2.7. SAXS 1D profiles for AS-1 without shearing (top line) and shear aligned AS-1 (bottom line) in the direction normal to the shear direction.

The shear aligned AS1 sample was then placed in large molar excess of TFA relative to *tert*-butyl groups for 3 hours on a shaker. For comparison one AS1 sample without shearing was also placed in TFA for 3 hours. The pictures of shear aligned AS1 and AS1 without shearing in TFA for 30 minutes are shown in Figure 2.8. We can see that AS1 sample without shearing at the left keeps its shape in TFA after 30 minutes; while the shear aligned AS1 at right has totally disintegrated after 30 minutes in TFA forming a hazy solution，indicating that the aligned lamellae structures were not stable.

Figure 2.8. AS1 without shearing in TFA for 30 mins (left) and shear aligned AS1 in TFA for 30 mins (right).

A closer look at the SAXS profile in Figure 2.5 reveals that broadening of the primary peak also occurs in the case of the AS-3-HF sample but not at all in the case of DAS-1-HF. Both samples show hexagonal morphology, but the nano cavities are expected to be different. Assuming unaltered PS matrix the observed peak broadening indicates that the Bragg scattering planes are less well-defined in AS-3-HF than in its precursor AS-3. This could be due to heterogeneous cavity size and cavity filling by PAA in the etched sample, a combined effect of dispersities in polymer mass/composition and most importantly PAA conformational freezing. The last effect stands for the irreversible PAA structure freezing in the glassy state during sample drying (the glass transition temperature of bulk PAA is around 100 °C). The nanoporous sample cannot be annealed without deleting nanoporosity; therefore, the effect of PAA conformational freezing is difficult to erase in the dry state. However, in the presence of water filling the cavities the PAA chains become dynamically flexible and the freezing effect disappears. In the case of the triblock copolymer, PDMS is totally removed, and this leaves an empty volume in the center of the cylinders, with the consequence that the presence of cavities is less sensitive to the PAA conformational freezing and the Bragg planes are well-defined also in the nanoporous sample. This interpretation is supported by electron microscopy of the dry samples and SAXS in the presence of water (see the discussion relative to Figures 2.9 and 2.10).

SEM micrographs of AS-3-HF and DAS-1-HF are shown on the same scale of magnification in Figure 2.9. The fractured surface investigated in AS-3-HF was very rough as can be seen in Figure 8a, which is due to increased sample brittleness correlating with the low molecular weight of the matrix polymer, PS. Both samples show hexagonal patterns of pores, with the distinct difference that the cavities for DAS-1-HF are larger and wider spread apart compared to the cavities for AS-1-HF. This is as expected from the molecular weights of the two samples and from the fact that the triblock sample sacrifices a larger portion of the molecule during degradation. The domain spacing (27 ± 3 and 46 ± 2 nm for AS-3-HF and DAS-1-HF, respectively) and pore radii (6 ± 1 and 11 ± 2 nm for the same samples, respectively) estimated from the SEM pictures were in good agreement with those obtained from the SAXS analysis (domain spacing, 27 and 47 nm, and pore radii, 6 and 14 nm, for the same samples, respectively), as listed in Table 2.2. Some of the pores in Figure 2.9 are visibly blocked or show lower contrast relative to the matrix. This feature is more pronounced in the case of sample AS-3-HF (Figure 2.9 a). The significant surface roughness of this sample hinders a clear analysis. The fast Fourier transform (FFT) of Figure 2.9 a hints to less well defined Bragg planes than in the case of Figure 2.9 b. This is in accordance with the SAXS profile of Figure 2.5 b showing broadening of the structural peaks in the case of the AS-3-HF sample. Freeze fracture samples were prepared from AS-1-HF, but no successful micrographs were recorded. Both the lamellar morphology and the quite low molecular weight of PS concur to produce high sample brittleness.

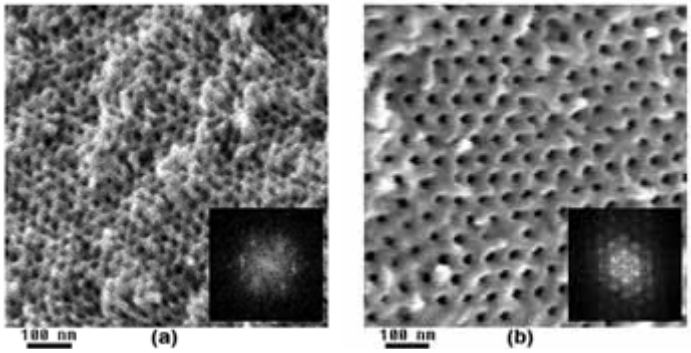

Figure 2.9. SEM pictures of (a) AS-3-HF and (b) DAS-1-HF. The inset in (a) shows a Fourier transform of a 330 nm × 330 nm region in the SEM picture of AS-3-HF and the inset in (b) shows a Fourier transform of a 550 nm × 550 nm region in the SEM picture of DAS-1-HF.

The deprotection reaction removes 44% of the P*t*BA polymer mass transforming it into PAA. The contour length and the number of chains are expected to be conserved in the process, but the way the PAA chains pack and their mass density in the nanoporous polymers are unknown. Expected cavity volume fractions after degradation are listed in the second and third columns of Table 2.2. Two values were calculated on the basis of SAXS data for the etched samples and the copolymer composition values. The first was calculated under the assumption that the generated PAA has the same density as PAA's bulk density reported in the literature and the second under the rather arbitrary assumption of PAA density equal to 1 g/cm^3. Qualitatively, this last assumption followed by the appreciation that the PAA chain density in the interface with PS is the same as the chain density of the bulkier P*t*BA precursor; therefore, the density of PAA in the etched samples is expected to be lower than the bulk density of PAA. In the next section on water uptake it will be seen that the pore volumes calculated with the lower density value of PAA are in satisfactory agreement with the observed volumes of absorbed water. Columns 4-7 in Table 2.2 list the characteristic length scale for the etched samples in the dry state as investigated by SAXS and SEM.

Table 2.2. Characterization data of HF-treated and TFA-treated samples in the dry state and in the presence of water.

sample	expected cavity volume [a] (v%) dry		d_{SAXS} [b] (nm) dry	d_{SEM} [c] (nm) dry	r_{SAXS} [d] (nm) dry	r_{SEM} [e] (nm) dry	d_{SAXS} [f] (nm) wet	expected water uptake [g] (v%)	observed water uptake (v%)
	$_{PAA}$=1.22	$_{PAA}$=1.00							
AS-1-HF	12	5.4	20	no [h]	1 [i]	-	24	21	21
AS-3-HF	17	14	27	27±3	6.1	6±1	27	14	13
DAS-1-HF	27	25	47	46±2	14	11±2	47	25	24
DAS-1-TFA	27	25	47	-	14	-	47	25	24

[a] Based on SAXS results of the dry etched samples and block composition. The density values used to calculate the cavity volume were: ρ_{PS} = 1.05 g/cm^3 [26], ρ_{PtBA} = 1.00 g/cm^3 [27], ρ_{PAA} = 1.22 g/cm^3 [26] (left) or ρ_{PAA} = 1.00 g/cm^3 (right), see text; ρ_{PDMS} = 0.966 g/cm^3 [26,28]; [b] Principal spacings d_{10} or lamellar spacing period d from SAXS; [c] Principal d_{10} spacings from SEM; [d] Pore radii calculated as shown in the text from d_{SAXS} and composition, assuming ρ_{PAA} = 1.00 g/cm^3; [e] Pore radius from SEM; [g] Based on d_{SAXS} and block composition. The density of PAA block plus water is arbitrarily taken 1.00 g/cm^3; [h] It was not possible to recognise any structure by SEM; [I] expected lamellar cavity height, d_{cavity}.

Assuming identical matrix structure before and after acid treatment, the pore radii of AS-3-HF, DAS-1-HF, and DAS-1-TFA from the SAXS profiles were calculated to 6, 14, and 14 nm (see column 6 in Table 2.2) by using the following relation:

$$r_{SAXS} = d_{SAXS} \times \sqrt{\frac{2}{\pi\sqrt{3}}(1 - f_{PS} - f_{PAA})} \qquad (2.1)$$

f_{PS} and f_{PAA} are volume fraction of PS and PAA block, respectively, and d_{SAXS} is the principal domain d_{10} spacing. The assumption of unchanged matrix is reasonable for the three samples with HEX structure, given the constancy of the respective scattering vectors before and after the acid treatments. Obviously, this assumption is not true for sample AS-1-HF. The concept of matrix is meaningless in this case. An average cavity height d_{cavity} of roughly 1 nm (see first entry in column 6) could be calculated for this sample by

$$d_{cavity} = d_{SAXS(AS-1-HF)} - d_{SAXS(AS-1)} \times (f_{PS} + f_{PAA}) \qquad (2.2)$$

on the basis of the SAXS lamella periods for the etched sample (first entry in column 4 of Table 2.2) and for the block copolymer precursor (first entry in the last column of Table 2.1), combined with volume composition data. The volume fraction f_{PAA} in the above relations was calculated assuming a PAA density of 1 g/cm^3.

2.5 Water uptake

A direct proof of hydrophilicity for the nanoporous materials presented here was the spontaneous uptake of water. The four nanoporous PAA-*b*-PS samples AS-1-HF, AS-3-HF, DAS-1-HF, and DAS-1-TFA were placed into glass vials containing distilled water. For comparison, a gyroid nanoporous PS sample prepared from PS-*b*-PDMS diblock copolymer precursor[11] was also placed into a glass vial containing pure water. After soaking in water for 1 day, the four PAA-*b*-PS samples sank down to the bottom of their respective vials. Volumes of water uptake for AS-3-HF, DAS-1-HF, and DAS-1-TFA were close to the expected volumes (see the last two columns in Table 2.2). The gyroid nanoporous PS sample from PS-*b*-PDMS precursor floated on the surface of water

and was not able to take any water within 3 weeks. This confirms that hydrophilic nanopores were created in the four PS-*b*-PAA samples.

The morphologies of the three nanoporous PAA-*b*-PS samples in water were investigated by SAXS, and Figure 2.10 shows the resulting data.

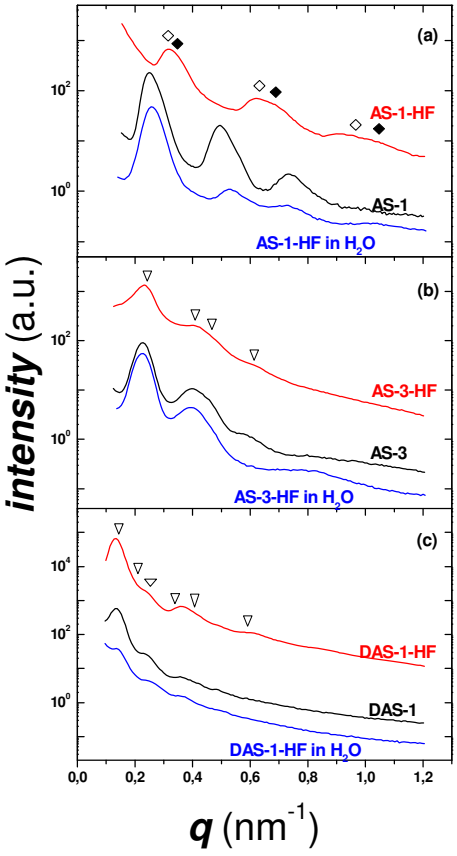

Figure 2.10. SAXS 1D profiles of (a) AS-1, AS-1-HF and AS-1-HF in H_2O (b) AS-3, AS-3-HF and AS-3-HF in H_2O and (c) DAS-1, DAS-1-HF and DAS-1-HF in H_2O. The scattering from the wet samples is observed at water uptake saturation.

Compared to the dry state the position of the primary peak for AS-1-HF in water shifted back to a smaller q value (0.260 nm^{-1}) and the scattering peaks became narrower, indicating expansion in the lamellar structure during water uptake. The primary scattering peak in water is similar to that of the original AS-1 diblock copolymer, while the higher order reflections are reduced. This suggests that water penetrates the sample and fills up the space originally occupied by the *tert*-butyl groups, and the lamellar morphology of the PS matrix is restored, though with reduced long-range ordering. The lamellar structure shows memory in the presence of water. The reason that AS-1-HF did not disintegrate is quite probably due to the missing of lamella alignment; some kind of topological interlocking of the lamellae would then be responsible for the observed sample stability. It cannot be excluded that morphological defects such as lamella ramifications also play a stabilizing role.

Within ±1%, the positions of primary peaks for AS-3-HF and DAS-1-HF do not change before and after water uptake. Soaking these samples in water produces to some degree reverse effects in the scattering profiles relative to the creation of nanoporosity by degradation. For example, the scattering from the samples AS-3-HF and DAS-1-HF in Figure 2.10 (panels b and c) show an overall drop in scattering intensity in the presence of water due to a reduced scattering contrast. The SAXS profile of the wet sample AS-3-HF in H_2O is quite similar to the profile of the precursor AS-3. The principal peak is of similar width in the two cases. This indicates that the Bragg planes in the wet sample are better defined than in the dry AS-3-HF sample. At a PAA mass concentration of roughly 50%, as is the case with water filling the cavities, the glass transition temperature of PAA falls below room temperature, rendering the chains dynamically flexible; the electron density profiles in the different pores become more similar, and therefore the definition of the Bragg planes is reestablished. The effect of reduced electron density (ρ_e) contrast is especially visible for the DAS-1-HF sample in water where the structural peaks are quite weak. Given the larger mass fraction of water in the cavities of this sample, the average ρ_e in the cavities can be estimated as that of water (0.556 mol/cm^3). This value is quite close to the ρ_e for PS (0.565 mol/cm^3). The electron density difference $\rho_{e,PS}$ - $\rho_{e,H2O}$ is 4-5 times lower in this case than the electron density difference between PS and PDMS ($\rho_{e,PDMS}$ =0.522 mol/cm^3) in the unetched sample.

2.6 Conclusion

Nanoporous PS with hydrophilic PAA cavity surfaces were successfully prepared from P*t*BA-*b*-PS and PDMS-*b*-P*t*BA-*b*-PS copolymer precursors. The combination of living anionic polymerization

and ATRP allows synthesizing PDMS-*b*-P*t*BA-*b*-PS triblock copolymer with a center P*t*BA block, which can be modified to the hydrophilic PAA and PDMS block that can be fully degraded. Deprotection of *tert*-butyl groups in P*t*BA and selective etching of PDMS chains were accomplished by applying HF or TFA in one step. Two different morphologies, lamellae and cylinders, have been achieved through the self-assembly of block copolymers as evidenced by SAXS. The hydrophilic property of nano cavity surfaces in the PAA-*b*-PS block copolymers was verified by water uptake measurements. The nanoporous polymers prepared in this work are expected to broaden the spectrum of possible applications of such materials in cases, which require aqueous or biological environment. In prospect, both the bulkiness of the protecting group in the acrylate polymer (*tert*-butyl in the present case) and the length of the PDMS chain can be used as controlling handles for the porosity and pore size.

2.7 Experimental

Materials. Tetrahydrofurane (THF) (Merck, ≥ 99%, stabilized with 0.025% butylated hydroxytoluene) was passed through a column of active aluminum oxide and then was refluxed over sodium in the presence of benzophenone until a deep purple color was attained. The building block of PDMS (hexamethylcyclotrisiloxane, D_3) (Sigma-Aldrich, 98%) was stirred over calcium hydride (CaH_2) for 4 hours at 65 °C and distilled into a flask containing vacuum-dried dibutyl magnesium. After stirring for another 4 hours, D_3 was distilled off again in an ampoule just before use. The two monomers *t*BA (Fluka, ≥ 98%) and styrene (St) (Sigma-Aldrich, 99%) were passed through a column of active aluminum oxide. The monomers as well as m-xylene (Sigma-Aldrich, 99+%) or triethylamine (TEA) were then stirred over CaH_2 for 4 hours at room temperature, and distilled before use. Anhydrous HF (Holz+Co, Germany) or TFA (Sigma-Aldrich, 98%) were used as received as degradation reactants. All other chemicals were received from commercial sources and used without further pretreatment.

Synthesis of P*t*BA-*b*-PS diblock copolymers by ATRP. The polymerizations were performed in 2-necked round-bottom flasks connected to the vacuum line and an Argon inlet and equipped with a rubber septum. In a typical polymerization of *t*BA, the flask was charged with 11.6 g (90.50 mmol) of *t*BA, 86.2 mg (0.60 mmol) of Cu(I)Br, and 75.7 μL (0.58 mmol) of Ethyl 2-bromo propionate (2-EBP). Oxygen was removed by three freeze-pump-thaw cycles and 122.5 μL (0.59 mmol) of

N,N,N',N'',N''-pentamethyldiethylene triamine (PMDETA) was added. Two additional freeze-pump-thaw cycles turned the color of the solution dark blue. Then the flask was immersed into a silicon oil bath, preheated to 60 °C. After 2.5 hours the flask was removed from the silicon oil bath and cooled down rapidly by using an isopropanol/dry ice bath. The reaction mixture was diluted with THF; the Cu-catalyst was filtrated while directly precipitating in methanol/water (7:3 vol.), and the polymer was dried in vacuum. The homopolymers were further employed as macroinitiators for block copolymerization with styrene in xylene solution. 0.7 g (0.09 mmol) of P*t*BA, 24.8 g (238.12 mmol) of styrene, 9.1 mg (0.06 mmol) of Cu(I)Br and 13 μL (0.06 mmol) PMDETA were added into 12.5 mL of xylene in a flask. After three freeze-pump-thaw cycles, the flask was immersed in a silicon oil bath, preheated to 100 °C where the block copolymerization took place. The polymerization was stopped after the desired time and the block copolymer was isolated in the same way as the homopolymer.

Synthesis of PDMS-*b*-P*t*BA-*b*-PS triblock copolymer by a combination of anionic polymerization and ATRP. *PDMS-H by anionic polymerization*. The polymerization was performed using an inert atmosphere system. 700 mL of purified THF was distilled into the reactor. 2.6 mL of *sec*-butyl lithium was added to the system using a syringe and upon the addition of initiator the color of the solution became yellowish. The reactor was cooled down to -5 °C in an isopropanol/dry ice bath. Then 12.4 g of D_3 was introduced as a 20 wt. % THF solution into the reactor and the color disappeared immediately, indicating that the polymerization started. After 3 days at 0 °C, the polymer was terminated with 1.3 mL of chlorodimethylsilane. The homopolymer (PDMS-H) was precipitated using methanol and dried in vacuum.

PDMS-Br macroinitator. Hydroxyl-terminated PDMS was firstly prepared: 8 mL of toluene, 0.41 mL of allyl alcohol and 0.016 mL of Pt catalyst were charged into a reactor with stirring. The reactor was heated to 50 °C in an oil bath. Then 8 g of PDMS-H was introduced into the reactor dropwise by a syringe, and the temperature was raised to 65 °C for 2 hours. Toluene and excess allyl alcohol were removed under vacuum at 100 °C. After cooling down to room temperature, the resultant mixture was diluted with THF, and the product PDMS-OH was precipitated in methanol and dried in vacuum. The synthesis of PDMS-Br was then performed. 0.047 g of 4-(dimethylamino)pyridine (DMAP), 0.228 g of bromoisobutyrylbromide and 50 mL of dry THF were charged into a two-necked round-bottom flask equipped with a stirrer bar, condenser and a dropping funnel, and 0.14 mL of dry TEA were added under nitrogen through the septum of the

dropping funnel with a long needle. The flask was cooled down to 0 °C in an ice bath. 6.61 g of PDMS-OH in 50 mL dry THF was then transferred to the dripping funnel and slowly added to the flask under stirring for 1 hour. The temperature was allowed to rise to room temperature. The mixture was stirred overnight and then the THF was evaporated. The crude product was dissolved in 100 mL of CH_2Cl_2 and purified by washing several times with water (5 wt% aq. $NaHCO_3$) and water again. The solution was dried overnight with $MgSO_4$, filtered and the CH_2Cl_2 was evaporated. A slightly yellow liquid product (PDMS-Br) was obtained, which was dried in vacuum.

PDMS-b-PtBA macroinitator. In the block copolymerization with *t*BA a Schlenk tube equipped with a magnetic stirrer bar was charged with 0.60 g (0.06 mmol) of PDMS-Br, 9 mg (0.06 mmol) of Cu(I)Br, 9.45 g (73.73 mmol) of *t*BA and 15 μL (0.07 mmol) of PMDETA. The system was degassed 3 times. The tube under nitrogen was immersed in a preheated oil bath at 60 °C for 3.5 hours. The mixture was precipitated in water/methanol (9:1 vol.), and dried in vacuum for several days.

PDMS-b-PtBA-b-PS triblock copolymer. 0.315 g (0.02 mmol) of PDMS-*b*-P*t*BA, 6 g (57.42 mmol) of styrene, 3.8 mg (0.03 mmol) of Cu(I)Br, 5 μL (0.02 mmol) of PMDETA and 3.5 mL of xylene were used in ATRP of styrene with the synthesized PDMS-*b*-P*t*BA macroinitiator as described above for the ATRP of styrene with P*t*BA macroinitiator.

Annealing. Diblock P*t*BA-*b*-PS and triblock PDMS-*b*-P*t*BA-*b*-PS copolymers were dissolved in THF and the solutions were poured into Petri dishes. The solutions were left for 3 days to evaporate slowly under a slight flow of Argon at room temperature. The solvent cast samples were annealed in a home made gas-tight steel cylinder under Argon at 130 °C for 5 days, and then gradually cooled down to room temperature.

Alignment. AS1 film was put between two microscope slides with 0.5 mm thickness aluminum foil as spacer. After heating under nitrogen at 140 ^{o}C for 25 minutes, AS1 film was oscillatory shear aligned by moving the two microscope slides with shear amplitude roughly 1000%.

Deprotection of P*t*BA and etching of PDMS. *With HF*. The deprotection of P*t*BA and etching of PDMS with anhydrous HF was accomplished using standard HF equipment for cleaving synthetic peptide-resins[29] at 0 °C for 2 hours. The detailed procedure is the same as the one described in ref. 11.

With TFA. The PDMS-*b*-P*t*BA-*b*-PS triblock copolymer film was stirred for 3 hours in large molar excess of TFA relative to PDMS repeating unit. Afterwards the sample was washed in methanol for 24 hours before drying under an Argon stream at room temperature.

Characterization Methods. SEC experiments were performed at room temperature with two mixed-D columns from Polymer Laboratories. Stabilized THF was used as a solvent with a flow rate of 1 mL/min. The calibration line was constructed from SEC data of PS narrow molecular weight standards in the range 7×10^2 - 4×10^5 g/mol. Molecular weight distributions relative to PS calibration were determined by processing the differential refractive index signal from a Viscotek model 200 detector. ^{1}H NMR spectra were recorded in $CDCl_3$ on a 250 MHz Avance DPX 250 Bruker instrument. FT-IR spectra were measured on a Perkin-Elmer SpectrumOne FT-IR spectrometer. SAXS patterns were acquired at the Risø National Laboratory using Cu KR X-rays with a wavelength of λ = 1.54 Å. SEM measurements were done on a Zeiss 1540 EsB Gemini instrument at the Center for Microtechnology and Surface Analysis at the Danish Technological Institute. The samples for SEM were prepared by freeze fracturing in liquid nitrogen. 2-3 nm gold layer was sputtered onto the samples prior to imaging. Water uptake experiments were carried out by placing dry samples in glass vials containing water and kept under gentle stirring at room temperature. After being submerged for a certain time, a fine tissue was used to dry the surfaces of the sample quickly before weighing.

2.8 References

1. Lee, J.-S.; Hirao, A.; Nakahama, S. *Macromolecules* **1988**, *21*, 274.
2. Liu, G.; Ding, J.; Guo, A.; Herfort, M.; Bazett-Jones, D. *Macromolecules* **1997**, *30*, 1851.
3. Liu, G.; Ding, J.; Stewart, S. *Angew. Chem. Int. Ed.* **1999**, *38*, 835.
4. Mao, H.; Arrechea, P. L.; Bailey, T. S.; Johnson, B. J. S.; Hillmyer, M. A. *Faraday Discussions* **2005**, *128*, 149.
5. Rzayev, J.; Hillmyer, M. A. *Macromolecules*, **2005**, *38*, 3.
6. Nakagawa, Y.; Miller, P. J.; Matyjaszewski, K. *Polymer* **1998**, *39*, 5163.
7. Miller, P. J.; Matyjaszewski, K. *Macromolecules* **1999**, *32*, 8760.
8. Kurjata, J.; Chojnowski, J.; Yeoh, C.-T.; Rossi, N.A.A.; Holder, S.J. *Polymer* **2004**, *45*, 6111.
9. Rutnakornpituk, M.; Ngamdee, P., Phinyocheep, P. *Polymer* **2005**, *46*, 9742.
10. Jankova, K.; Chen, X.; Kops, J.; Batsberg, W. *Macromolecules* **1998**, *31*, 538.
11. Ndoni, S.; Vigild, M. E.; Berg, R. H. *J. Am. Chem. Soc.* **2003**, *125*, 13366.
12. Schulte, L.; Szewczykowski, P.P.; Guo, F.; Andersen, K.; Vigild, M. E.; Berg, R. H.; Ndoni, S. *Submitted to Polym. Sci. Part A: Polym. Chem.*
13. Hyman, H. H.; Garber, R. A. *J. Am. Chem. Soc.* **1959**, *81*, 1847.
14. Willson, C. G.; Ito, H. *J. Electrochem. Soc.* **1986**, *133*, 181.
15. MacDonald, S. A.; Willson, C. G.; Fréchet, M. J. *Acc. Chem. Res.* **1994**, *27*, 151.
16. Ichikawa, R.; Hata, M.; Okimoto, N.; Oikawa-Handa, S.; Tsuda, M. *J. Polym. Sci. Part A: Polym. Chem*. **1998**, *36*, 1035.
17. Bryan, D. B.; Hall, R. F.; Holden, K. G.; Huffman, W. F.; Gleason, J. G. *J. Am. Chem. Soc.* **1977**, *99*, 2353.
18. Clements, J. H.; Weber, S. E. *J. Phys. Chem. A* **1999**, *103*, 2513.
19. Ma, Q.; Wooley, K. L. *J. Polym. Sci. Part A: Polym. Chem*. **2000**, *38*, 4805.
20. Davis, K. A.; Matyjaszewski, K. *Macromolecules* **2000**, *33*, 4039.
21. Yang, D.; Li, L.; Wang, C. *Mater. Chem. Phys.* **2004**, *87*, 114.
22. Wilczek, L.; Chojnowski, J. *Macromolecules* **1981,** *14*, 9.
23. Sigwalt, P. *Polymer J.* **1987**, *19*, 567.
24. DeSimone, J. M.; Paisner, S. N. *US Patent Appl. Pub.* **2003,** 20030180522 A1.
25. Paisner, S. N.; DeSimone, J. M. *Abstracts of Papers*, **2002**, 224th ACS National Meeting, Boston, MA, United States, August 18-22, 2002
26. Mark, J. E. Editor, *Polymer Data Handbook* **1999**, Oxford University Press, New York.

27. van Krevelen, D. W.; Hoftyzer, P. J. *Properties of Polymers* **1976**, Elsevier, Amsterdam, Oxford, New York, Tokyo.

28. Brandrup, J.; Immergut, E. H. *Polymer Handbook, 3rd ed.* **1989**, John Wiley & Sons, New York.

29. Merrifield, R. B. *J. Am. Chem. Soc*. **1963**, *85*, 2149.

Chapter 3 Nanoporous 1,2-Polybutadiene with Different Cross-linking Degrees

3.1 Introduction

The most common nanoporous polymers are prepared from PS containing block copolymers where the PS matrix block remains in the glassy state.[1-4] Such materials do not need chemical modification of the matrix phase such as cross-linking because the phase is mechanically stable as a glass. However there are some drawbacks of these glassy-matrix materials, such as lack of thermal stability and low resistance to solvents. These will limit their use in many specific applications, where high temperatures or the presence of solvent are unavoidable. Nanopores will collapse as the temperature approaches the glass transition of the matrix materials,[5] and obviously the matrix dissolves when exposed to solvents.

A nanoporous material of a chemically cross-linked matrix will be advantageous for many applications. Cross-linking the matrix phase increases the thermal and mechanical stability and also improves resistance to solvents. If cross-linking degree can be controlled, corresponding properties of the nanoporous polymers can be tuned to meet the requirements of different applications. Furthermore, cross-linking can warrant 'memory' of the nanoporous morphology even at high temperature or in good solvents.

6 years ago, Ndoni with his co-workers and Hillmyer with his co-workers independently reported the preparation of nanoporous cross-linked polyisoprene (PI) from PI-*b*-PDMS precursors.[6,7] Most polydienes show *Tg* below 0 °C and therefore are unstable as nanoporous polymers at room temperature. Cross-linking of the polydiene before the removal of PDMS is necessary and feasible in a controlled way. Compared to PI nanoporous polymers, the amount of cross-linker needed to prepare nanoporous 1,2-PB samples with similar mechanical properties is reduced by factors in the range 30-100. Therefore 1,2-PB-*b*-PDMS diblock copolymers are a more attractive source of cross-linked nanoporous polymers. They can be prepared in a highly controlled way by living anionic polymerization, the 1,2-PB block is easily amenable to cross-linking, and the PDMS block can be quantitatively and selectively removed. Since 1,2-PB has a glass transition temperature below 0 °C, the cross-linking degree plays a key role in the stability of the nanopores. The cross-linking

---

The first half part of this chapter has been published in *Macromolecules* **2007**, *40*, 3669.

performed at a certain temperature 'freezes' the sample morphology stable at that temperature and therefore is an additional control parameter of nanoporous polymers' morphology.

Two groups of 1,2-PB-*b*-PDMS diblock copolymer precursors were prepared. At 140 °C they have hexagonally packed cylindrical morphology or gyroid morphology. Cross-linking degree of 1,2-PB can be controlled by changing the amount of cross-linker and the cross-linking time. Effect of cross-linking on structure and properties of nanoporous 1,2-PB was investigated on the samples with hexagonal cylindrical morphology derived from the first group precursor. Nanoporous 1,2-PB with gyroid and a metastable phase morphologies were obtained by cross-linking 1,2-PB of the second group precursor at different temperatures.

3.2 Hexagonal cylindrical nanoporous 1,2-PB with different cross-linking degrees

All 1,2-PB-*b*-PDMS block copolymers used in this thesis research were prepared by Lars Schulte. Briefly, sequential anionic polymerization of 1,2-PB and then D_3 in THF was employed. The 1,2-PB-*b*-PDMS block copolymer particularly used in this subsection was named as BD4 and had the following properties: The number-average molecular weight (M_n) was 15 kg/mol, as determined by SEC and ^{1}H NMR. The volume fraction of PDMS (f_{PDMS}) was 0.29, and 90.5% of the repeating units in the polybutadiene block were 1,2-units, as determined by ^{1}H NMR spectroscopy. The polydispersity index (PDI) of BD4 relative to PS SEC calibration was 1.22. Rheology trace of a temperature scan of BD4 shown in Figure 3.1 suggests that from 17 °C, *G'* and *G''* decrease smoothly up to an order to disorder transition temperature (ODT) at 260 °C. This block copolymer exhibits a single ordered phase, which according to the SAXS pattern shown in Figure 3.1, is hexagonal cylindrical morphology (HEX), in agreement with the composition.

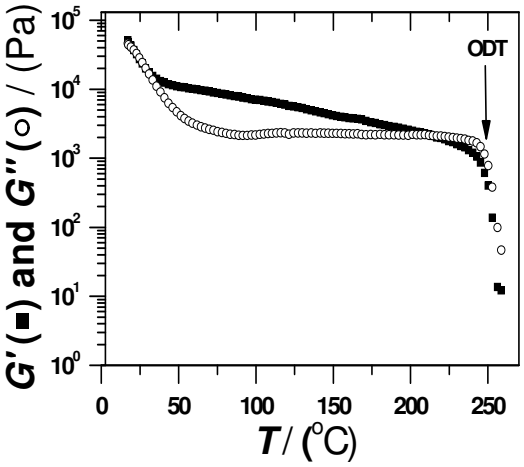

Figure 3.1. Temperature dependence of dynamic shear moduli of BD4 at shearing conditions ω =1 rad/s and heating at 2.5 °C/min.

The first step of sample preparation was to produce a series of variously cross-linked samples from the block copolymer precursor. Dicumyl peroxide (DCP) was used as cross-linker. Table 3.1 lists the cross-linking conditions and characterization data for the cross-linked BD4 samples, which are named by the prefix "X" followed by a numeral. For each sample the numeral identifies the ratio between the concentration of double bonds which were consumed during the cross-linking procedure ($n_{db,c}$) relative to the concentration of original double bonds in the BD4 precursor sample ($n_{db,0}$). Below the explanation on how this ratio ($n_{db,c}/n_{db,0}$) is measured and how it can be related to the degree of cross-linking will be given.

The cross-linking of 1,2-PB is a chain reaction,[8] which is the reason why only few molar percent of DCP relative to the double bonds is sufficient to generate a well cross-linked network. Generally the trend for the cross-linked samples in Table 3.1 is that an increased fraction of double bonds is consumed as the cross-linker (DCP) concentration and/or the cross-linking time increases.

Table 3.1. Cross-linking conditions (at 140 °C) and characteristics of cross-linked samples. The M_c values calculated from Eq. 3.1 are listed in the last column.

	cross-linking conditions		double bond ratio ($n_{db,x}/n_{db,0}$) [b]			
Sample	conc.($n_{DCP}/n_{db,0}$)[a]	time (h)	from FT-IR	from Raman	equilibrium swelling ratio [c] in toluene	$M_{c,\,Flory}$ [d] (g/mol)
X 0.11	0.004	1	0.89	0.90	3.60±0.03	5522
X 0.15	0.002	1	0.85	0.80	2.13±0.04	1230
X 0.34	0.001	2	0.66	0.63	1.60±0.02	478
X 0.41	0.008	1	0.59	n.m. [e)]	1.42±0.01	305
X 0.52	0.01	1	0.48	n.m.	1.28±0.01	196
X 0.58	0.002	2	0.42	0.37	1.26±0.02	183
X 0.62	0.008	2	0.38	n.m.	1.20±0.01	143
X 0.82	0.02	2	0.18	0.20	1.15±0.01	113

[a] n_{DCP} is mole of DCP molecules and $n_{db,0}$ is mole of double bonds in virgin material; [b] $n_{db,x}$ is mole of double bonds in cross-linked material; [c] Equilibrium swelling ratio is the mass ratio between equilibrium of the swollen and the dry sample; [d] $M_{c,Flory}$ is the average molecular weight between neighbouring cross-links as calculated from the Flory scheme (see text). [e] Not measured.

This trend is also illustrated in Figure 3.2, where the FT-IR spectra of the original 1,2-PB-*b*-PDMS and samples X 0.11, X 0.41, and X 0.62 are shown. The DCP concentration used in the cross-linking of sample X 0.11 was half of that used for sample X 0.41, and the cross-linking time was 1 h in both cases. The concentration of DCP was the same in the cross-linking of X 0.41 and X 0.62, but the cross-linking time of X 0.62 was 2 h. In the case of sample X 0.11 the fraction of consumed double bonds is lower than in the case of sample X 0.15, despite the higher concentration of DCP in the first case (see data on the first two samples in Table 3.1). This discrepancy at the low end of DCP concentration range is probably due to slight differences in the sample temperature during the cross-linking reaction of the two samples. Another possibility is the presence of different (though very low) oxygen concentrations in the two cases. The important point is that an increased consumption of double bonds correlates to an increased cross-linking degree for all the samples, as will be discussed below in relation to the swelling degree of the samples in toluene.

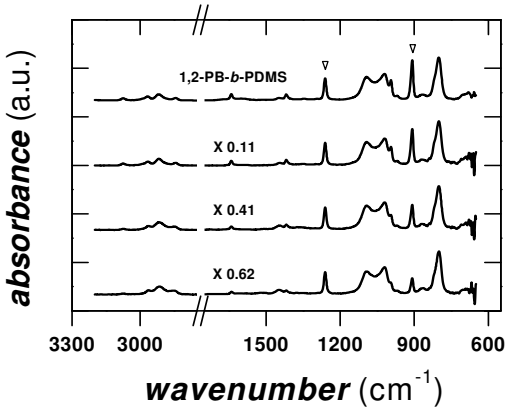

Figure 3.2. FT-IR spectra of (a) 1,2-PB-*b*-PDMS (BD4), (b) X 0.11, (c) X 0.41 and (d) X 0.62. Bottom-up triangles mark the absorption bands at 908 cm^{-1} (out of plane C-H bending peak in $=CH_2$) and 1261 cm^{-1} (CH_3 bending in PDMS), which were used for the quantification of double bond concentration. The absorbance in the range between 2750 and 1750 cm^{-1} for all the samples is completely flat and omitted for clarity.

Two peaks in the FT-IR spectra were selected to quantify the concentration of double bonds in the samples after crosslinking relative to the precursor polymer. The out-of-plane C-H bending peak in $=CH_2$ at 908 cm^{-1} represents the double bonds of 1,2-PB, and the CH_3 bending peak at 1261 cm^{-1} represents PDMS (see marked peaks in Figure 3.2). Separate measurements (not shown) indicate that the cross-linking does not affect the PDMS block which allows us to take the PDMS peak as an internal standard.[6] Therefore, the ratio between the intensities at 908 and 1261 cm^{-1} is directly proportional to the number of 1,2-PB double bonds present in the samples. The ratio of the number of double bonds ("db") in a cross-linked sample ($n_{db,x}$) relative to the number of double bonds in the mother polymer ($n_{db,0}$) is easily found by comparison of FT-IR data of cross-linked samples and the unreacted mother polymer. The ratios $n_{db,x}/n_{db,0}$ are listed in the fifth column of Table 3.1, and the fraction of double bonds consumed by the cross-linking, $n_{db,c}/n_{db,0}$, is simply $n_{db,c}/n_{db,0} = 1 - n_{db,x}/n_{db,0}$. The FT-IR results are in good agreement with the results obtained by Raman spectroscopy, which are shown in the sixth column of Table 3.1. Depending on DCP concentration and cross-linking time, the fraction of consumed double bonds varies in the range from 11% to 82%.

Clearly, the swelling ratio of cross-linked 1,2-PB-*b*-PDMS samples in toluene must reflect the cross-linking of the samples. The values of weight equilibrium swelling ratio for the different samples are shown in the sixth column of Table 3.1. These results reveal that the equilibrium swelling is dependent on the fraction of consumed double bonds in the cross-linked 1,2-PB matrix. Notice that the swelling ratio is only 1.15 for the sample with the highest cross-linking degree X 0.82. The plot of swelling ratio vs fraction of consumed double bonds is shown in Figure 3.3.

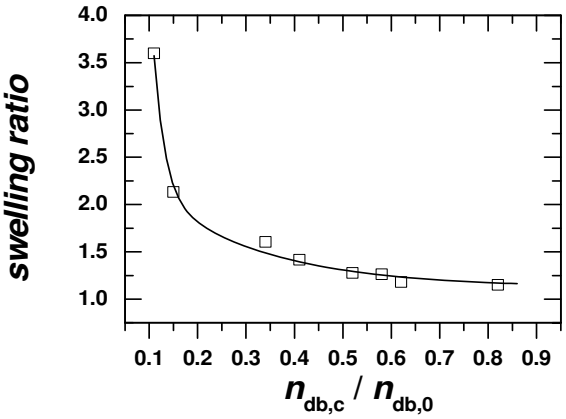

Figure 3.3. The plot of swelling ratio in toluene vs. fraction of consumed double bonds for cross-linked 1,2-PB-*b*-PDMS. The curve is a guide to the eye. The swelling ratio is the mass ratio between equilibrium of the swollen and the dry sample.

The more double bonds consumed during sample preparation, the higher the degree of cross-linking of the resulting network, which physically leads to less swelling of the samples in toluene. Neither the loss of double bonds during cross-linking nor the degree of swelling readily gives us a parameter which describes the molecular structure of the resulting network. In search of such a model parameter the average molecular weight M_c between neighboring network cross-links was considered. Well aware of possible shortcomings of the model as applied to the present situation, we nevertheless attempt to describe the swelling data in the form required by the Flory model.[9] The system dealt with is a block copolymer system, micro-phase segregated with only one of the blocks being cross-linked. This is not directly included in the domain of application of the Flory scheme. For the samples with highest cross-linking degree the cross-linking degree is too high, again

pushing the system outside the applicability of the Flory scheme. In addition, the 1,2-PB is expected to changes of the chemical structure (cycle formation on the main chain) during the cross-linking reaction[8] and this makes the use of a unique interaction parameter questionable. Taken these points into consideration, of course we have our doubts on whether there is a direct physical meaning related to the calculated network strand M_c. On the other side, to test the applicability of the model, eight samples of 1,2-PB homopolymer were cross-linked at the same conditions as the block copolymer samples. The swelling degree of the homopolymer as a function of consumed double bonds is similar to that found for the block copolymer (data not shown). The Flory model states

$$M_c = - \rho[V_1 (v_2^{1/3} - \omega v_2)] / [\ln (1- v_2) + v_2 + \chi_{12} v_2^2] \qquad (3.1)$$

where M_c is the average molecular weight between neighboring cross-links, ρ is the overall density, V_1 is the molar volume of solvent (107 cm^3/mol for toluene), v_2 is the polymer volume fraction at equilibrium swelling, χ_{12} is the solvent-polymer interaction parameter (0.47 for toluene - 1,2-PB[10]) and ω is twice the inverse of the cross-link functionality (here, we take ω as 0, which is the limit for very high cross-linking functionality). Polymer volume fractions at equilibrium swelling can be calculated from the swelling ratios, and values of M_c are listed in the last column of Table 3.1. The molecular weight between cross-links (the same as a network strand) can easily be transformed into an average degree of polymerization per strand N_c by: $N_c = M_c / M$, where M is the molar mass of the PB monomeric unit. Figure 3.4 shows the dependency of the consumed fraction of double bonds on the inverse of the average polymerization degree per network strand $1/N_c$. This relationship is, to a good approximation, linear, and it serves as a justification for using the fraction of the consumed double bonds in 1,2-PB as a direct measure of the cross-linking degree of this polymer from which we will prepare nanoporous materials.

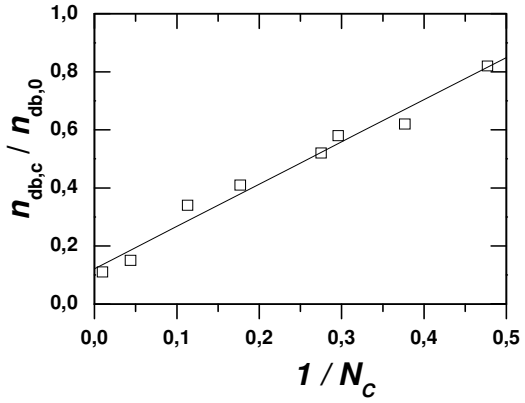

Figure 3.4. The relationship between the consumed fraction of double bonds and the inverse of the calculated average polymerization degree per network strand $N_{c,\,Flory}$. The equation of the linear fit is: $y = 1.45\,x + 0.12$ with $R = 0.99$.

The etched samples are named by adding the prefix "E" to the name of the corresponding cross-linked sample. TBAF in THF was used as etching reagent for the cross-linked BD4 samples. FT-IR was used to monitor the chemical composition changes of BD4 after etching. Figure 3.5 shows a sequence of absorbance spectra on samples illustrating the progression of preparation: the FT-IR spectra of original BD4, the cross-linked sample X 0.58, and the corresponding etched sample E-X 0.58. The complete removal of PDMS is clearly evidenced by the disappearance of the characteristic absorbance bands for PDMS at the five marked peaks. An accurate determination of the change in double bond concentration as a result of the etching reaction is difficult to obtain alone from the FT-IR spectra of the sample before and after etching. In a separate experiment, a solution of the precursor block copolymer in THF was reacted for 36 h with TBAF, under similar conditions as those applied for the cross-linked samples. No double bonds were observed lost after the reaction, within the ^{1}H NMR accuracy. This was taken as an indication that virtually all of the double bonds in cross-linked BD4 prevail after etching. These remaining double bonds offer the possibility of changing the surface characteristics of pore walls by chemical reactions with other functional groups.

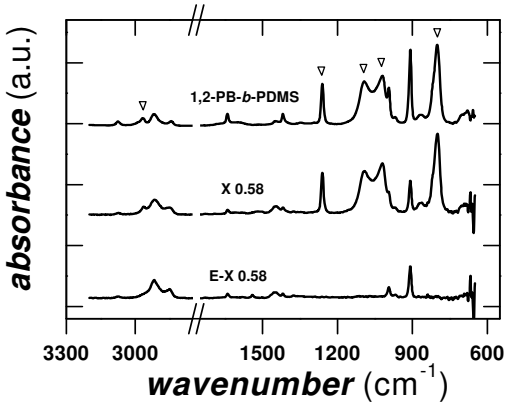

Figure 3.5. FT-IR spectra of (a) 1,2-PB-*b*-PDMS, (b) X 0.58 and (c) E-X 0.58. Five characteristic peaks of absorbance for PDMS are marked by bottom-up triangles.

Figure 3.6 shows SAXS 1D profiles of the same series of samples shown in Figure 3.4, illustrating the progression of preparation. The scattering pattern is consistent with a morphology of hexagonally packed cylinders. Four characteristic peaks are marked in the figure for the etched material. The scattering intensity of the primary peak for the etched sample has increased significantly relative to that of the cross-linked sample. This is due to the removal of PDMS during etching, which causes an increased electron density contrast as a result of PDMS replacement by vacuum ($\rho_e \approx 0$). The data confirm the preparation of nanoporous 1,2-PB with hexagonal cylindrical morphology. Figure 3.6 also reveals the small length change of the principal scattering vector q^*. The scattering vector length increases slightly from 0.298 nm^{-1} before cross-linking to 0.319 nm^{-1} after cross-linking and finally to 0.324 nm^{-1} after etching. This corresponds to a domain spacing between principal Bragg planes (d_{10}) of 21.1, 19.7, and 19.4 nm, respectively. The decrease of domain spacing is most pronounced over the cross-linking step. This could be caused by shrinkage of the matrix as a result of the cross-linking.

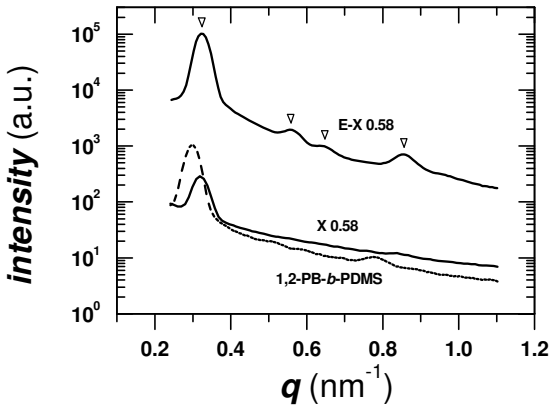

Figure 3.6. SAXS 1D profiles of E-X 0.58, X 0.58 and 1,2-PB-*b*-PDMS (dashed line) showing the scattered intensity as a function of the scattering vector length q. The characteristic peaks for hexagonally packed cylinder morphology are marked (q–ratios relative to the principal peak: 1, $3^{1/2}$, $4^{1/2}$, $7^{1/2}$).

Figure 3.7 depicts SAXS 2D profiles of a solvent-cast sample (E-X 0.58, Figure 3.7 a) and a shear-aligned sample (E-X 0.62, Figure 3.7 b). The rings on the scattering patterns illustrate the random orientation of domains of the hexagonal cylinders in E-X 0.58. While the presence of two arcs of reflection with the beam perpendicular to the shear direction (**x**) indicates that there is a preferential orientation of the hexagonal cylinders in E-X 0.62, the arcs of intensity are located along the neutral or vorticity direction (**z**) in the shear-aligned sample.

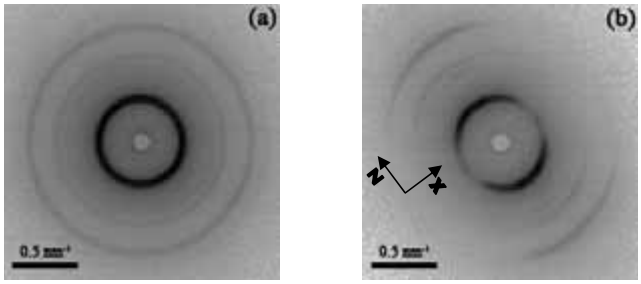

Figure 3.7. SAXS 2D profiles of (a) solvent cast sample E-X 0.58 and (b) shear-aligned sample E-X 0.62. The shear direction (**x**) and the neutral direction (**z**) of the extrusion is noted on (b).

The degree of orientation was characterized by the second order orientation factor, F_2, calculated from the SAXS 2D profile.[11,12] The azimuthal SAXS profile at q^* is shown in the Figure 3.8. The values of the azimuthal angle on the x-axes are chosen such that the shear direction is at 0°. The profile is evidently bimodal and it has been fitted by two Lorentzian curves, also shown on the plot. The Lorentzian peaks are at 74º and 100º, respectively. This double alignment is expected to relate to the flow geometry within the extruder. The alignment parameter F_2 was calculated for each of the two directions separately and for the overall scattering profile. The calculated values of the overall and the two partial orientation factors were 0.62, 0.72, and 0.73, respectively.

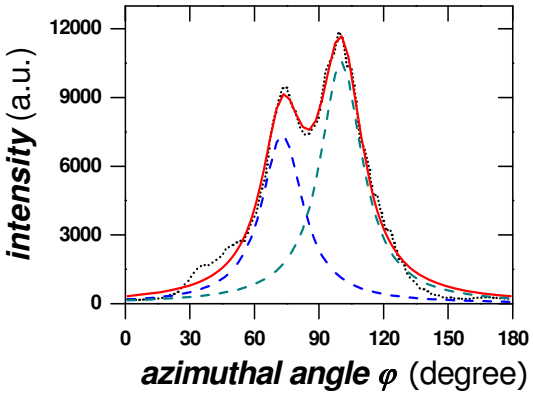

Figure 3.8. The SAXS scattering profile at q^* (dotted line) as a function of the azimuthal angle ϕ and its fit as a sum (red line) of two Lorentzians (segmented blue and green lines). The shear direction is at 0º (180º).

Figure 3.9 shows SEM pictures of the solvent-cast sample E-X 0.82 (Figure 3.9 a) and the shear-aligned E-X 0.62 (Figure 3.9 b, c). The SEM micrographs cover roughly sample areas of 0.4 μm^2 and show directly the evidence for nanoporous structure in both samples. It is possible to observe a change in cylinder axis direction (a kink) of the solvent-cast sample in Figure 3.9 a. On the other hand, the shear-aligned sample in Figure 3.9 b showed a unique orientation of cylindrical channels. The same good alignment was observed in the micrometer length scale as the sample was shifted hundreds of microns inside the microscope. Figure 3.9 c is an end-on SEM micrograph of the same shear aligned sample, clearly showing hexagonally packed pores. Being 2D projections of the surface of a 3D body, SEM pictures like those shown in Figure 3.9 give a realistic image of

alignment on flat areas of the observed surface at micron length scale. The overall alignment at macroscopic length scales is more appropriately characterized by SAXS as discussed in the previous paragraph. It was not possible to observe any porosity from the SEM of sample E-X 0.41. The samples with lower cross-linking degree were not analyzed by SEM (see Table 3.2).

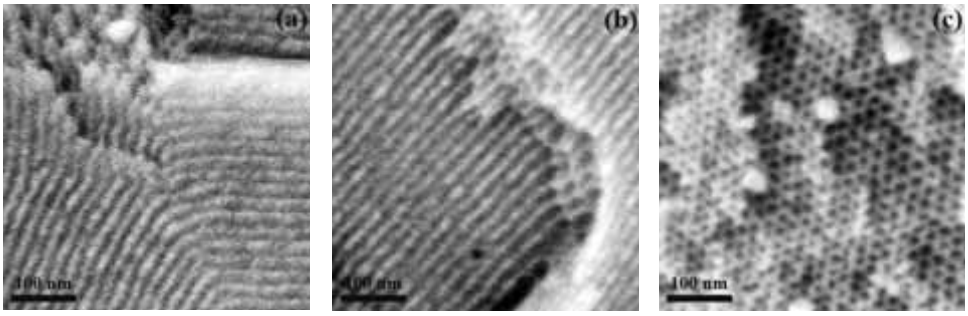

Figure 3.9. SEM pictures of (a) the solvent cast sample E-X 0.82, (b) edge-on view of the shear-aligned sample E-X 0.62 and (c) end-on view of the shear-aligned sample E-X 0.62. The micrograph in (a) displays different orientations of the hexagonal domains.

Table 3.2 lists results of X-ray scattering, microscopy, and solvent uptake of the etched 1,2-PB samples. The swelling ratios of the etched samples in toluene are listed in the second column of Table 3.2. It is clear that the swelling behavior of the etched samples follows the same tendency as that of the cross-linked samples in Table 3.1. The ratio between the swelling ratios for the lowest and highest cross-linked samples is roughly 3, which is similar to the corresponding ratio for the cross-linked samples in Table 3.1. Furthermore, all swelling ratios for the etched samples are larger than those for the corresponding cross-linked ones. This is expected as the cavities formed after the PDMS cleaving allow for higher toluene uptake.

Table 3.2. The data on solvent uptake, SAXS and SEM measurements for etched 1,2-PB samples.

Sample	equilibrium swelling ratio in toluene	equilibrium methanol uptake [a] (v%)	d_{SAXS} [b] (nm)	d_{SEM} [c] (nm)	r_{SEM} [d] (nm)
E-X 0.11	4.59±0.12	1±1	no peak	n.m. [e]	n.m.
E-X 0.15	3.25±0.44	1±1	no peak	n.m.	n.m.
E-X 0.34	1.87±0.08	12±2	17.6±0.1	n.m.	n.m.
E-X 0.41	1.77±0.01	18±2	17.7±0.1	n.m.	n.m.
E-X 0.52	1.64±0.02	30±1	18.9±0.1	no porosity[f]	no porosity
E-X 0.58	1.65±0.03	29±1	19.4±0.1	n.m.	n.m.
E-X 0.62	1.60±0.03	29±1	19.3±0.2	19.9±1.7	4.7±1.3
E-X 0.82	1.54±0.04	29±2	19.5±0.2	18.2±3.0	5.0 ±1.0

[a] Volume fraction of methanol uptake; [b] Principal domain d_{10} spacings from SAXS; [c] Principal domain d_{10} spacings from SEM; [d] Pore radius from SEM. [e] Not measured. [f] No porosity observed by SEM.

Figure 3.10 illustrates the trend of the SAXS profiles from the etched samples with different cross-linking degrees. The two top profiles in Figure 3.10 show the scattering of samples E-X 0.82 and E-X 0.52 and display similar features as the SAXS profile shown for sample E-X 0.58 in Figure 3.6. The SAXS profile for sample E-X 0.62 (not shown) also shows the same features. These scattering profiles represent scattering from nanoporous materials, with a strong principal peak of scattering and some higher-order reflections. The lower profile in Figure 3.10 shows the scattering of sample E-X 0.15. This profile does not show any evidence for structured features that can be detected by SAXS. This suggests that there is no nanoporous structure and that the sample is collapsed during etching. Most probably, the 1,2-PB matrix is not cross-linked sufficiently to counteract the tendency of surface area minimization after the removal of PDMS. The remaining profile in Figure 3.10 represents the scattering of sample E-X 0.41 and shows a weak principal peak at $q^* = 0.355$ nm^{-1}. The scattering intensity of the primary peak for sample E-X 0.41 is increased by ~1 order of magnitude, comparing it to the scattering from its related cross-linked sample X 0.41 (data not shown). This is much less than the expected increase in scattering strength due to the greater contrast factor as mentioned above for the nanoporous polymers. The scattering of sample E-X 0.34 showed a principal peak of scattering (data not shown) similar to E-X 0.41. These two samples

exhibit scattering which clearly is not indicating a nanoporous structure (as seen in the well cross-linked samples) because of the relatively weak Bragg peak. On the other hand, the scattering does not resemble the scattering of the collapsed structures (as seen in the very weakly cross-linked samples) because there is still a significant peak in the scattering profile. The structure of these samples must be different from the nanoporous and the collapsed structures. We will return to the discussion of the nature of this structure after the presentation of the methanol uptake in Figure 3.11.

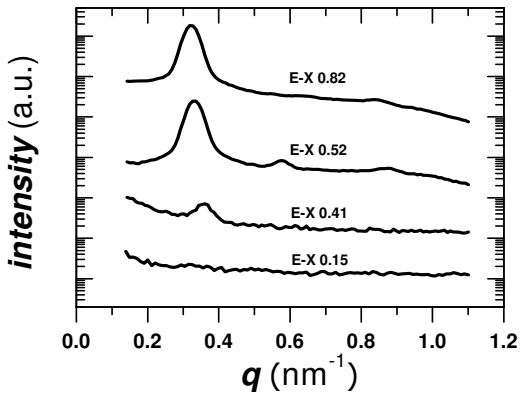

Figure 3.10. SAXS 1D profiles of four different etched samples with various crosslinking degrees. The plots have been shifted vertically to ease comparison.

The fourth column of Table 3.2 lists the principal d_{10} spacing for all the etched samples as obtained from SAXS measurements. The table shows that the samples have *d*-spacings from 17.6 to 19.5 nm depending on the degree of cross-linking and suggests that within a range of 10% it is possible to change the domain lattice spacing via cross-linking. The fifth column of Table 3.2 lists the principal d_{10} lattice spacings of samples E-X 0.62 and E-X 0.82 from SEM micrographs. They show good agreement with the data obtained by SAXS. The pore radii obtained from SEM for these two samples are shown in the last column of Table 3.2.

Methanol uptake was used to investigate the porous properties of the etched samples. The volume fraction of the methanol uptake was calculated from the following expression: $V_{mu}/V_0=(m_{mu}/0.791)/(m_{mu}/0.791 + m_e/0.902)$, where V_{mu} is the volume of methanol uptake (mu), V_0 is the original volume of the mother block copolymer, m_{mu} is the mass of methanol uptake, 0.791 g/cm^3 is the density of methanol, 0.902 g/cm^3 is the density of 1,2-PB,[13] and m_e is the mass of the

dry etched sample. The values for the equilibrium methanol uptake are listed in the third column of Table 3.2.

Figure 3.11 shows the time-resolved data for methanol uptake of the different samples with varying cross-linking degree. Methanol was chosen on the basis of two reasons: First, being a non solvent for 1,2-PB, it would permit to fill the nanopores without swelling the bulk of the polymer. Second, having a surface contact angle with 1,2-PB less than 90°, the capillary forces would permit methanol to actually penetrate the nanopores. The four sets of data shown in Figure 3.10 correspond to the uptake after four different contact times with methanol: 2, 24, 50, and 150 h. The samples follow three different behaviors: (i) Samples with high cross-linking degree (data with $n_{db,c}/n_{db,0} > 0.5$) show a saturated amount of methanol uptake at all plotted times. This saturation appeared for times shorter than 10 min (data not shown). (ii) Samples in the middle segment of cross-linking degree (data with $0.3 < n_{db,c}/n_{db,0} < 0.45$) show an increasing methanol uptake with time over the 150 h time span. (iii) Samples of lowest cross-linking degree (data with $n_{db,c}/n_{db,0} < 0.2$) do not take up more than few volume percent of methanol in the time span of 150 h. The volume fraction of methanol uptake for the samples in the first group is around 30%. This figure is close to the volume fraction of PDMS (29.4%) in the precursor block copolymer. These data indirectly prove that the PDMS was removed by TBAF and that pores exist in the etched samples. The uptake of methanol for the samples in the second group is a slow process. Both a thermodynamic equilibrium (related, e.g., to slight lowering of interfacial energy in the presence of methanol compared to the surface energy of the dry samples) and a kinetic argument relying on the diffusion barriers for methanol in the PB matrix could be the basis of such a process.

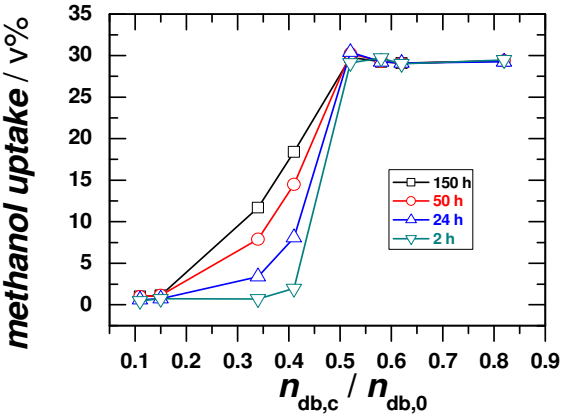

Figure 3.11. Volume fraction of methanol uptake for etched samples with varying cross-linking degrees after four different times (2 h, 24 h, 50 h and 150 h).

The three sample categories described here also followed different sinking behavior. Samples E-X 0.11 to E-X 0.41 sank down to the bottom of the vial immediately after soaking in methanol, while E-X 0.52 to E-X 0.82, which could take up methanol to the expected limit, floated on the surface of methanol for about 30 s before sinking down to the bottom. This observation suggests a test procedure which may be used as a rapid indicator of nanoporosity for dry samples. Because of the existence of pores, the dry nanoporous samples have overall densities smaller than methanol (0.791 g/cm^3); an overall density of roughly 0.7 g/cm^3 is expected for the samples with high cross-linking degree. As a result, such a sample will float in first contact with methanol; it will actually remain floating as long as the quantity of methanol penetrating into the nanopores does not push the overall density above 0.791 g/cm^3. For the highly cross-linked samples this corresponds to methanol filling more than roughly 1/3 of the pore volume.

A combination of the structural features from SAXS measurements with the behavior diversity during methanol uptake points to a characterization scheme of the differently cross-linked 1,2-PB material. The samples E-X 0.34 and E-X 0.41 are singled out by both the SAXS scattering and the methanol uptake behavior. FT-IR data (not shown) give evidence that all PDMS is removed from these samples. The SAXS profile hints to the absence of real nanocavities, but the methanol uptake shows that some amount of methanol does indeed penetrate into the sample over time. We speculate that the removed PDMS leaves a trace behind, which may be only a modulation of the PB density in

the diblock copolymer after etching with lower density values in the location of the PDMS. This density modulation gives rise to a corresponding electron density modulation which is the cause of scattering SAXS peak and also accommodates penetration of methanol into the sample. We call this intermediate structure a "traced" structure in this polymer system.

Accordingly, the material can take on one of the following three structures: nanoporous, traced, or collapsed. The borderline between the traced and the collapsed states is expected to be solvent-dependent. The nanoporous samples are E-X 0.52 to E-X 0.82, which take up methanol to the saturation level within 10 min. The saturation volume is close to the volume of the removed PDMS microphase. The scattering from the dry samples is strong with intense Bragg peaks. The traced morphology samples are E-X 0.34 and E-X 0.41, which slowly take up methanol over an extended time span (150 h). The volume of methanol uptake for the sample E-X 0.41 reaches ~60% of the expected maximum limit V_{PDMS}. The SAXS profile from the E-X 0.34 and E-X 0.41 dry samples shows scattering 1-2 orders of magnitude weaker than the scattering from the dry nanoporous samples. The collapsed samples are E-X 0.11 and E-X 0.15, which do not take up appreciable volumes of methanol and display no peak in the SAXS profile.

3.3 Bicontinuous gyriod and a metastable phase nanoporous 1,2-PB

The 1,2-PB-*b*-PDMS block copolymer used in this subsection was named as BD14 and had a number-average molecular weight (M_n) of 10.7 kg/mol, a polydispersity (PDI) of 1.04, and an PDMS volume fraction (f_{PDMS}) of 0.39. The rheology data of the sample shown in Figure 3.12 shows the existence of multiple ordered phases. At about 60 °C, both *G'* and *G''* start to increase and *G'* has a higher slope, which suggests an OOT form one ordered phase to another ordered phase. At 105 °C, *G''* decreases significantly, indicating a second OOT. At 180 °C, there is another point of inflection in *G''*, indicating a third OOT. Finally, both *G'* and *G''* decrease dramatically at 205 °C, which is ODT temperature. There are three different OOT during the temperature range from room temperature to 205 °C.

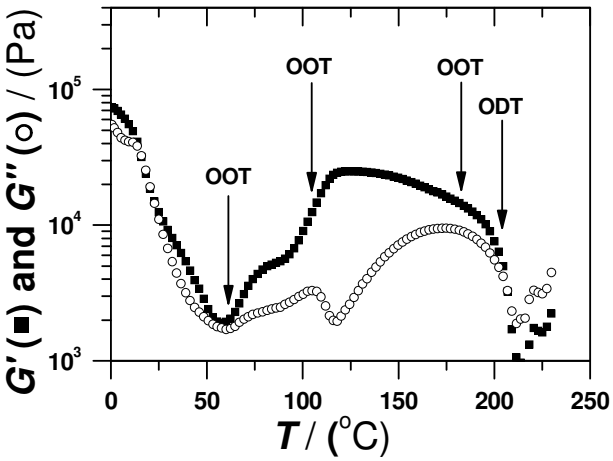

Figure 3.12. Temperature dependence of dynamic shear moduli of BD14 at shearing conditions ω =1 rad/s and heating at 2 °C/min.

SAXS measurements were applied to elucidate the assignments of the ordered morphologies of the block copolymer sample. Figure 3.13 shows SAXS 1D profiles of the sample at 27 °C, 80 °C, and 120 °C. Due to very low electron density contrast between 1,2-PB and PDMS blocks, the obtained high-order scattering peaks are very week. However, we still can distinguish the major difference among these SAXS patterns with this resolution. The pattern at 27 °C is for lamellar (LAM) morphology: a primary peak at q^* = 0.29 nm^{-1} and a second-order peak at q= 0.58 nm^{-1}. From rheology curves, both *G'* and *G''* have the same order of magnitude at low temperature range, indicating a LAM structure. When temperature is raised to 80 °C, two weak shoulders of the primary peak and an additional peak at q= 0.51 nm^{-1} show up. All the five scattering peaks can be indexed according to the hexagonally perforated lamellar (HPL) structure, which is a metastable phase, with an ABCABC stacking: 0.89q^* for (101), q^* for (003), 1.21q^* for (102), 1.76q^* for (104) and 2q^* for (006).[14] Three-parameter index was used here to describe the hexagonal structure. The spacing between three 1,2-PB lamellae can be calculated as c = 65.0 nm from q value of (003) reflection, and distance between two pores can be calculated as a = 30.2 nm from (101) and (003) reflections. The obtained *c/a* ratio is 2.15, which is very close to that found by Loo et al. (2.24) for ABCABC stacking of polystyrene-*b*-poly(ethylene-alt-propylene)[15] and by Zhu et al. (2.13) for polystyrene-*b*-poly(ethylene oxide)[16]. The metastable HPL phase causes higher magnitude for *G'* than *G''*, because arrays of pores have been introduced into previous pure LAM structure. When the

sample is heated to 120 °C, the characteristic scattering peaks (q^* and $8/6^{½}$ q^*) for gyroid (GYR) morphology are observed from the top SAXS trace. From rheology measurement, *G'* is significantly larger than *G''*, confirming the formation of solidlike GYR. And the *G'* of the GYR phase is higher than that of the HPL phase because the GYR has a 3 dimensional bicontinuous structure and HPL has a monocontinuous layer structure. Unfortunately valid SAXS patterns were not recorded above 160 °C, due to the oxidation of the polymer melt. We could not proof the existence of the third OOT through SAXS.

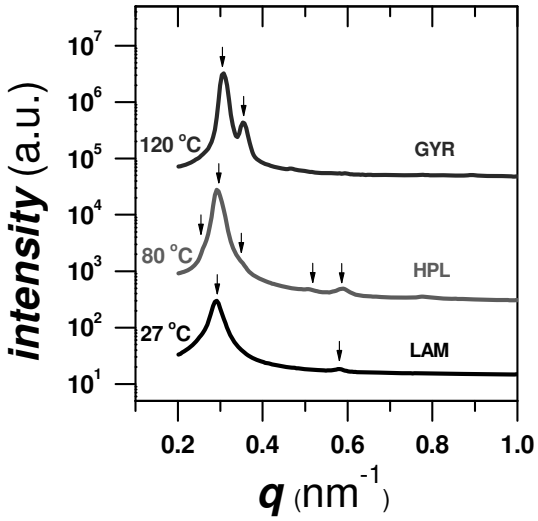

Figure 3.13. SAXS 1D profiles of BD14 at 27, 80, and 120 °C.

In order to capture nanoporosity with HPL and GYR morphologies, two different cross-linking procedures were used. For GYR morphology, DCP was used to cross-link 1,2-PB at 140 °C for 2 hours. For HPL morphology, an equimolar mixture of dilauroyl peroxide (DLP) and dicumyl peroxide (DCP) was used as cross-linker to cross-link 1,2-PB in two steps: the sample was first cross-linked at 80 °C for 8 hours to 'freeze' the HPL morphology, then the temperature was raised up to 140 °C for 2 hours to make sure cross-linking degree is high enough to avoid pore collapse. The use of mixture of DLP and DCP in this case is because their half life times for 10 hour are at 60 °C and 115 °C, respectively.[17,18] TBAF was then employed to etch PDMS away for both cross-linked samples.

Figure 3.14 shows the 1-D and 2-D SAXS profiles of the nanoporous sample BD-x(140ºC)-E. The 1-D scattering curve is indexed to match the reflections of the gyroid morphology. The lattice constant of the cubic lattice calculated from the position of the first allowed SAXS diffraction peak was 47.5 nm. Scanning and transmission electron microscopy pictures of BD-x(140ºC)-E are shown in Figure 3.14. The SEM micrograph shows the (211) projection known also as 'knitting pattern', while the (111) or the 'wagon wheel' projection is visible in the TEM micrograph. The crystallographic cell size estimated from the TEM micrograph was 47 ± 6 nm, in good agreement with the one calculated from SAXS. A pore radius of 6 nm was roughly estimated from the SEM image. From methanol uptake, the porosity of the gyroid nanoporous polymer was calculated to be 40%. The specific surface area of the sample was 260 ± 30 m^2/g measured from N_2 adsorption.

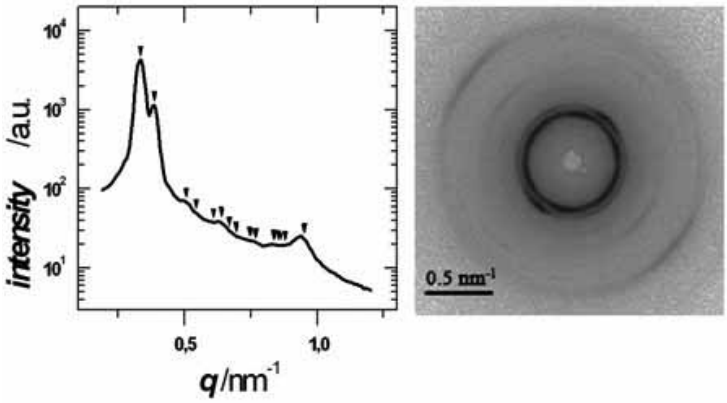

Figure 3.14. 1-D and 2-D SAXS profiles of a nanoporous sample *BD-x(140ºC)-E*. The [211], [220] and other characteristic peaks for the gyroid morphology are marked in the 1-D profile (the marked positions, expected for scattering from gyroid have the following q ratios: $6^{1/2}$, $8^{1/2}$, $14^{1/2}$, $16^{1/2}$, $20^{1/2}$, $22^{1/2}$, $24^{1/2}$, $26^{1/2}$, $30^{1/2}$, $32^{1/2}$, $38^{1/2}$, $40^{1/2}$, $42^{1/2}$, $50^{1/2}$). The lattice constant is 47.5 nm.

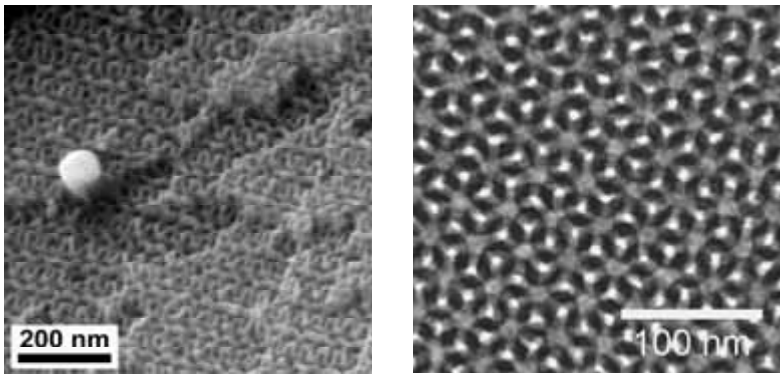

Figure 3.15. SEM and TEM images of BD-x(140°C)-E clearly showing gyroid morphology. Projection (211) known also as knitting pattern is clearly visible in the SEM micrograph; (111) or wagon wheel pattern is clearly visible in the TEM micrograph.

Figure 3.16 shows the SAXS 1D profile of the nanoporous sample BD-x(80ºC)-E. For comparison the SAXS pattern of BD-x(140ºC)-E is also included. The relative ratios of five scattering peaks for BD-x(80ºC)-E are 1, $(8.3/6)^{1/2}$, $3^{1/2}$, $4^{1/2}$, $7^{1/2}$. The SAXS pattern is different to that obtained from the block copolymer precursor at 80ºC (see the middle curve in Figure 3.13). This is out of our expectation. With the exception of the second peak the above ratios are typical for the hexagonal cylinder morphology (see Figure 3.6). The second peak is not at exactly the same position as the second allowed peak of the gyroid symmetry shown in the top curve in Figure 3.16, even though these two positions are very close. The SAXS pattern looks like a superposition of scattering from HEX and GYR structures. Figure 3.17 is the SEM image of the sample BD-x(80ºC)-E. A pattern of cylinders packed in some 'disturbed' hexagonal symmetry is found in the image. Hexagonally perforated lamella (HPL) or GYR structure can not be observed from the image. One of the possible reasons for not obtaining HPL structure is that the morphology of 1,2-PB-PDMS block copolymer might be 'frozen' at higher temperature rather than 80 ºC. The cross-linking of 1,2-PB is a chain reaction, at 80 ºC there might not be enough thermal energy gained for opening double bonds in 1,2-PB. A metastable phase, which is related to HPL phase, in the transition between the thermodynamically stable LAM and GYR micro-phase between can be captured at another temperature during the two steps of cross-linking.

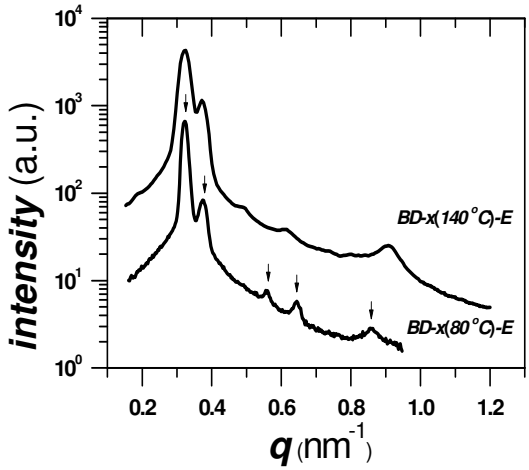

Figure 3.16. SAXS 1D profile of the nanoporous sample BD-x(80ºC)-E and BD-x(140ºC)-E.

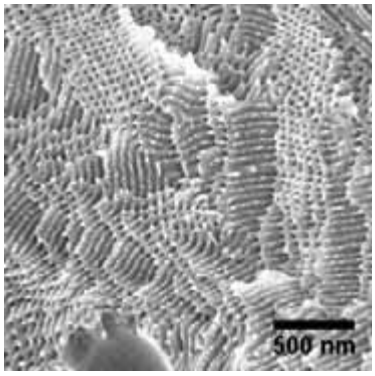

Figure 3.17. SEM image of nanoporous sample BD-x(80ºC)-E.

3.4 Conclusion

Nanoporous 1,2-PB with hexagonally packed cylinder, gyroid and metastable phase morphologies were prepared from diblock copolymers 1,2-PB-*b*-PDMS. The 1,2-PB matrix was stabilized by cross-linking before removing the PDMS block. Thermal scission of peroxides (DCP or DLP) was used to initiate the cross-linking of 1,2-PB. TBAF in THF was used subsequently for the selective degradation of PDMS.

The influence of cross-linking degree on the structure and properties of selectively etched polymers with HEX morphology was investigated. A simple relation between "Flory cross-linking degree" and the fraction of consumed double bonds during the cross-linking reaction was found, based on data on the swelling degree of cross-linked block copolymers in toluene. The combination of morphological results from SAXS with data on time-dependent methanol uptake suggested the presence of three different structures dependent on the cross-linking degree of the 1,2-PB matrix. In order of increasing degree of cross-linking, these three structures were designated as collapsed, traced, and nanoporous. By applying cross-linking, the thermal and mechanical stabilities of nanoporous polymers were improved. Furthermore, the nanoporosity with ordered structure could survive when the polymers were subjected to different solvents.

Different morphologies of block copolymers can be reached by changing either the total length of the blocks, the composition of the blocks or temperature. In this chapter, the preparation of nanoporous 1,2-PB with gyroid and a metastable phase morphologies obtained by controlling the temperature of cross-linking reaction of same block copolymer precursor were discussed. Compared to other morphologies, gyroid structure has advantages on connectivity in 3D, huge area surface and large porosity. Rest of the thesis work is based on the nanoporous 1,2-PB with gyroid structure.

3.5 Experimental

Synthesis of 1,2-PB-*b*-PDMS. The 1,2-PB-*b*-PDMS diblock copolymer precursors were synthesized by sequential living anionic polymerization in THF. *Sec*-butyllithium was used as initiator. The polymerization of 1,3-butadiene was performed at -20 ±3 ºC for 3 hours. Then D_3, was added to the reactor and the temperature was raised up to 0 ºC. The polymerization of D_3 took 3 days before termination with chlorotrimethylsilane.

Solvent casting. 1,2-PB-*b*-PDMS samples were dissolved in THF and the solutions were poured into Petri dishes. The solutions were left for 3 days to evaporate slowly under a slight flow of Argon at room temperature.

Shear Alignment. One of the 1,2-PB-*b*-PDMS (BD4) samples was aligned through a home-made extrusion device with a rectangular die. A film with 0.5 mm thickness and 10 mm width was obtained by pressing the block copolymer through the die.

Cross-linking of 1,2-PB. DCP and DLP (both from Merck) were used as received for the cross-linking of 1,2-PB. For DCP alone used as cross-linker, the cross-linker was co-dissolved with the block copolymer in THF in 0.1 - 2 % molar amounts (n_{DCP}) relative to the moles of the double bond ($n_{db,0}$) in the mother polymer. The ratio (n_{DCP}/ $n_{db,0}$) was one of the parameters varied in order to obtain differently cross-linked samples. The other parameter was the reaction time. The solutions were left under an argon flow and the solvent evaporated overnight. The cross-linking of the solvent cast blends was conducted under argon at 140 °C for 1-2 hours in a home made gas-tight steel cylinder. For one single sample, *BD-x(80ºC)-E,* an equimolar mixture of DLP and DCP was used to carry the cross-linking reaction in two steps: the sample was first kept at 80 °C for 8 hours then at 140 °C for 2 hours.

Etching of PDMS. 1.0 M tetrabutylammonium fluoride (TBAF) in THF (from Sigma-Aldrich) was used as cleaving reactant for PDMS. Cross-linked samples were stirred for 36 hours in a volume of THF solution containing 5 times molar excess TBAF relative to PDMS repeating unit. Afterwards the samples were washed with fresh THF and methanol for 24 hours before drying under an Argon flow at room temperature.

Chromatography and spectroscopy. The molecular weight of 1,2-PB-*b*-PDMS was determined by a combination of SEC and ^{1}H-NMR. The chemical composition and the number of double bonds surviving after cross-linking and etching of the 1,2-PB-PDMS samples were monitored by Fourier transform infrared FT-IR (PerkinElmer Spectrum) and Raman (Renishaw system 3000) spectroscopies. Specimens of 1 cm x 1 cm of 0.5 to 1 mm thickness were prepared for the measurements.

Rheology. The morphology of the diblock copolymers was investigated by isothermal and temperature-gradient dynamic mechanical measurements on a Rheometrics RS 800 using parallel plate geometry.

Swelling studies and pore accessibility. Swelling behaviour of cross-linked and etched samples and pore accessibility of etched samples were investigated by the uptake of either toluene or methanol. Dry samples (25-62 mg) were placed in glass vials containing 15 ml of toluene or methanol and kept under gentle stirring at room temperature. After being submerged for a certain time a fine tissue was used to dry the surfaces of the sample quickly before the sample mass was measured and the sample placed back in the liquid. Data was collected as a function of time as the weighing

procedure was repeated. Toluene and methanol uptake measurements were carried out until the mass of the wet sample stabilized and did not change by more than 0.1 mg over 24 hours. The swelling ratios at different times were calculated for each sample by the mass ratio between swollen and dry sample.

SAXS. Except for the temperature-dependent SAXS measurements of block copolymer BD14 (Figure 3.12), all other SAXS measurements were done at the Danish Polymer Centre, Risø National Laboratory using Cu K_α X-rays with a wavelength of λ = 1.5418 Å. Radiation was generated by a rotating anode operating at 3 kW and focused and filtered (only Cu K_α is selected) by a multilayer X-ray mirror and collimated by 3 pinholes. The scattered radiation was collected with a 2D position-sensitive gas proportional, delay line detector. 2D data was integrated azimuthally to give 1D scattering profiles of the scattered intensity as a function of the scattering vector. SAXS measurements of BD14 at different temperatures were carried out at beamline 7-11 at MAX-lab synchrotron radiation source in Lund, Sweden, with a wavelength of λ = 1.5418 Å.

Electron Microscopy. A typical sample for scanning electron microscopy (SEM) was prepared by first freeze fracturing a piece of nanoporous polymer film in liquid nitrogen; the pieces were then mounted onto an aluminum specimen mount using Ted Pella double coated carbon conductive tabs and CCC Carbon Adhesive (Electron Microscopy Science). Each sample was sputter-coated with 2-3 nm gold layer in a Polaron SC7640 and kept under vacuum in the microscopy chamber for 14-16 hours before scanning. A 2 kV electron beam accelerating voltage was chosen in a FIB-SEM Zeiss 1540 EsB Gemini instrument at the Center for Microtechnology and Surface Analysis at the Danish Technological Institute. Transmission electron microscopy (TEM) images were collected on a FEI TECNAI T20 operating at 200 kV, at the Center for Electron Nanoscopy of the Technical University of Denmark. Samples with 80 or 100 nm thickness were prepared on a LEICA ULTRACUT microtome using a DIATOME diamond knife at room temperature.

3.6 References

1. Hedrick, J. L.; Labadie, J.; Russell T.; Hofer, D.; Wakharker, V. *Polymer* **1993**, *34*, 4717.
2. Hashimoto T.; Tsutsumi, K.; Funaki, Y. *Langmuir* **1997**, *13*, 6869.
3. Ndoni, S; Vigild, M. E.; Berg, R. H. *J. Am. Chem. Soc.* **2003**, *125*, 13366
4. Wolf, J. H.; Hillmyer, M. A. *Langmuir* **2003**, *19*, 6553.
5. Hillmyer, M. A. *Adv. Polym. Sci.* **2005**, *190*, 137.
6. Hansen, M. S.; Vigild, M. E.; Berg, R. H.; Ndoni, S.; *Polymer Bulletin* **2004**, *51*, 403.
7. Cavicchi, K. A.; Zalusky, A. S.; Hillmyer, M. A.; Lodge, T. P. *Macromol. Rapid Commun.* **2004**, *25*, 704.
8. Szewczykowski, P. P. *Ph. D. Thesis*, DK-2800 Kgs. Lyngby, Denmark, **2009**.
9. Flory, P. J. *Principles of Polymer Chemistry*; Cornell University Press: Ithaca, NY, **1953**.
10. Mark, J. E. *Physical Properties of Polymers Handbook*; American Institute of Physics Press: Woodbury, NY, **1996**.
11. Sakurai, S.; Aida, S.; Okamoto, S.; Ono, T.; Imaizumi, K.; Nomura, S. *Macromolecules* **2001**, *34*, 3672.
12. Zalusky, A. S.; Olayo-Valles, R.; Wolf, J. H.; Hillmyer, M. A. *J. Am. Chem. Soc.* **2002**, *124*, 12761.
13. Mark, J. E. *Polymer Data Handbook*. **1999**, Oxford Unviersity Press.
14. Lai, C.; Loo, Y.-L.; Register, R. A.; Adamson, D. H. *Macromolecules* **2005**, *38*, 7098.
15. Loo, Y.-L.; Register, R. A.; Adamson, D. H.; Ryan, A. J. *Macromolecules* **2005**, *38*, 4947.
16. Zhu, L.; Huang, P.; Cheng, S. Z. D.; Ge, Q.; Quirk, R. P.; Thomas, E. L.; Lotz, B.; Wittman, J.-C.; Hsiao, B. S.; Yeh, F.; Liu, L. *Phys. Rev. Lett.* **2001**, *86*, 6030.
17. Hansen, M. S. *B. Sc. Thesis*, Technical University of Denmark, DK-2800 Kgs. Lyngby, Denmark, **2003**.
18. Mark, H. F.; Bikales, N. M.; Overberger, C. G.; Menges, G. *Encyclopedia of Polymer Science and Engineering, Vol. 14*, **1988**, John Wiley & Sons, New York, USA.

Chapter 4 Functional Nanoporous 1,2-Polybutadiene via Surface Initiated ATRP and Click Chemistry

4.1 Introduction

Ability to manipulate and control the surface properties of NPs according to required application is very important in the designing of functional NPs. In comparison with synthesis of triblock copolymer precursors with functional block in the middle as described in chapter 2, surface modification of porous polymers is easier and more versatile. However, not all NPs are suitable for undergoing surface modification. There are at least two requirements. The first is that the porous polymers should be mechanically stable; otherwise porous structure can not remain during or after modification. For instance, nanoporous PS can not be modified by wet chemistry in good solvents, like THF or toluene. The second requirement is that pores should be accessible. Isolated spherical morphology is not feasible for many modification cases. Thanks to its good mechanical stability and bicontinuous network, nanoporous 1,2-polybutadiene with gyroid morphology is an appropriate platform to prepare diverse functional NPs.

Introduction of functional polymer brushes to pore surface is a useful method for tailoring surface properties, such as antifouling ability and biocompatibility. Polymer brushes can be attached by either physisorption or covalent bonding. In physisorption, polymer chains are adsorbed onto surface with a reversible process and such polymer brushes are often unstable.[1] Covalent tethering of polymer brushes to surface can be achieved by either '*grafting from*' or '*grafting to*' approaches.[2,3] The functionality, length and density of polymer brushes can be well controlled by '*grafting from*' via different surface-initiated living polymerization methods.[4-7] Compared to other surface-initiated living polymerization methods, like anionic, cationic and ring-opening polymerizations, the ATRP requires milder reaction conditions and has more selection of monomers. For ATRP, once the initiator is immobilized onto surface, the polymer chains can grow directly from the reactive site of surface. In case of planar surfaces and big pores, it is possible to use sacrificial initiator, which is not attached to the surface on purpose, in the surface-initiated ATRP synthesis to monitor chain growth of the attached polymers. When pore size is reduced to a dozen of nanometers, steric confinement makes it not easy to extract the unattched polymers, so that

---

This part of the work has been published in *Langmuir* **2010**, *26*, 2008.

employing sacrificial initiator is not suitable. For the '*grafting to*' approach, polymer chains are attached directly on surfaces via reaction between end-functionalized polymers and appropriate reactive groups on pore surfaces.[1] Cu(I)-catalyzed azide/alkyne cycloaddition (CuAAC), also termed as click chemisty, has been extensively used in this approach due to its efficiency and simplicity.[8-11] The method is versatile as well, once a pool of polymers has been prepared with appropriate end-functional groups they can be reacted independently with surfaces. Compared to surface-initiated ATRP, the chain length of the pre-prepared polymers can be well characterized before carrying out click chemistry, but it is difficult to obtain high grafting densities by click chemistry because of steric hindrance of the surface reactive sites by the already attached polymer chains.

In this chapter, the fabrication of novel nanoporous PB (1,2-polybutadiene is abbreviated to PB for simplicity in this chapter and the following chapters) with cavities decorated of polyacrylates: poly(poly(ethylene glycol) methacrylate) (PPEGMA) and poly(2-hydroxyethyl methacrylate) (PHEMA); sulfonated polymers: poly(4-styrenesulfonate) (PSS) and poly(2-acrylamido-2-methyl-1-propanesulfonic acid) (PAMPS); and methoxy poly(ethylene glycol) (MPEG) by either ATRP or click chemistry will be described. Two different approaches to obtain initiator-modified PB are demonstrated, one chemical and the other photochemical. Both types of modified nanoporous PB were amenable to grafting various monomers by surface-initiated ATRP. Alternatively, azide groups were attached onto the nanopore walls and reacted with alkyne end-capped MPEG by click chemistry. In all cases functionalized NPs of predetermined morphology were obtained. Starting with one single NP of well controlled morphology, the physicochemical properties can be changed by different strategies as illustrated. The demonstrated procedures of surface modification will broaden the spectrum of applications of NPs. For instance, in the ultrafiltration field the modified NPs are expected to extend the selection range of solvents. The photochemical approach allows patterning, which in combination with the presented chemical modification could provide interesting materials for biomedical applications; such materials are also expected to show wave guiding.[12] The modified NPs could also be used as scaffolds for metallization or incorporation of inorganic substances in the PEG containing layer. The protocols presented expand the versatility of NPs by controlling the pore functionality via surface-initiated ATRP or click chemistry.

4.2 Modification via surface-initiated ATRP

Scheme 4-1 shows the routes of grafting PPEGMA by ATRP onto nanoporous PB. (Names of different compounds are also shown in the scheme. Abbreviations are first clarified under Experimental part.)

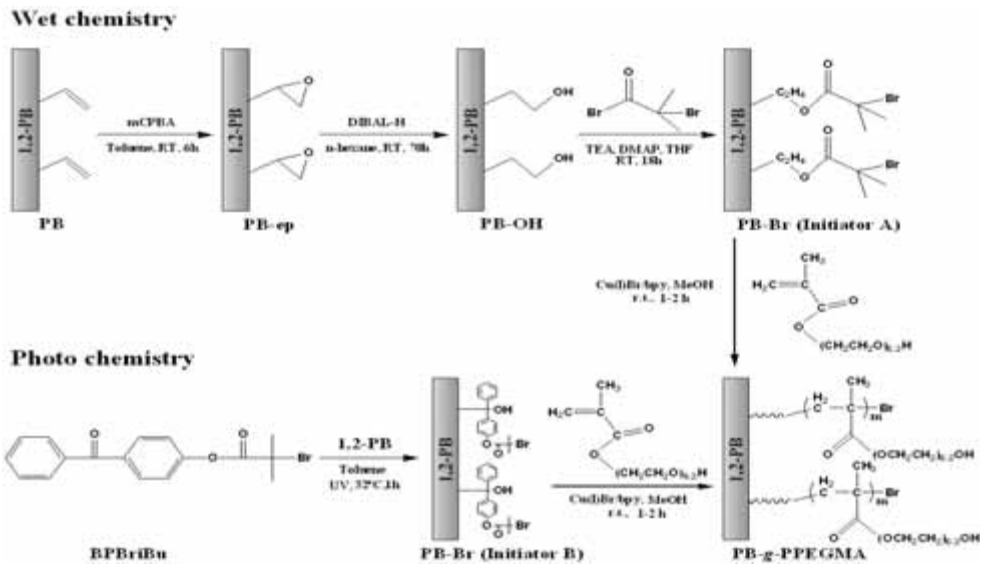

Scheme 4-1. Synthesis of PB-*g*-PPEGMA by surface-initiated ATRP using Initiator A (wet chem.) or Initiatior B (photo chem.).

The three-step procedure for chemical immobilization of initiator A was validated by FT-IR. Figure 4.1 shows FT-IR spectra of the original PB nanoporous material, the epoxidized sample (PB-ep), the hydroxyl group containing sample (PB-OH) and finally the initiator immobilized film (PB-Br).

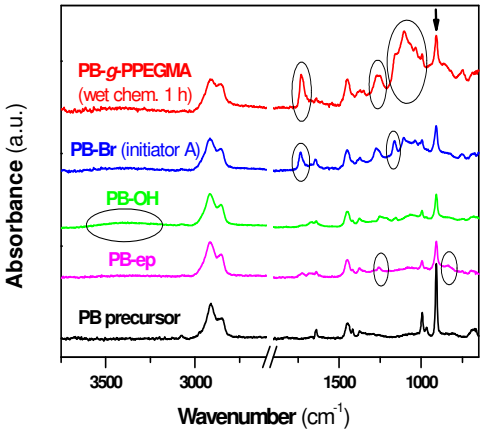

Figure 4.1. FT-IR spectra of the original nanoporous material (PB precursor), the epoxidized sample (PB-ep), the hydroxyl group containing sample (PB-OH), the immobilized monolith initiator film (PB-Br) and finally the resulting surface modified sample (PB-*g*-PPEGMA). H-C= peak at 908 cm^{-1} is marked as an arrow. Absorption peaks highlighted with circles are discussed in the text.

The characteristic absorption peaks related to epoxy groups at 1250 (ring stretching) and 800 cm^{-1} (ring deformation) appear in PB-ep and the intensity of the peak for double bonds at 908 cm^{-1} (out-of-plane C-H bending) is reduced after the epoxidation. The appearance of peaks at 3400-3200 cm^{-1} (O-H stretching) indicates the formation of hydroxyl groups in the film after hydroxylation. Finally, the peaks corresponding to ester groups at 1730 (C=O stretching) and 1230 cm^{-1} (ester C-O stretching) confirm the immobilization of the bromoisobutyrate initiator onto the PB film.

The obtained monolith initiator PB-Br was used to polymerize PEGMA, HEMA, NaStS, and AMPS by ATRP. The use of methanol as solvent in ATRP is advantageous, as methanol exclusively penetrates the porous volume of nanoporous PB.[13] As a result most of the grafted polymer chains are expected onto the pore-wall surface. FT-IR spectroscopy confirms the presence of PPEGMA in the nanoporous PB-*g*-PPEGMA as shown in Figure 4.1. Compared to the spectrum of the PB precursor, additional characteristic peaks associated with ester groups and ethylene oxide units in the grafted polymers appear in the case of the modified film: at 1730 cm^{-1} (C=O), 1230 cm^{-1} (ester C-O) and 1110 cm^{-1} (C-O-C). The FT-IR spectra of PB-*g*-PHEMA, PB-*g*-PAMPS and PB-*g*-PSS are shown in Figure 4.2. The appearances of characteristic peaks for ester groups and ethylene

oxide units in the grafted PHEMA, and sulfonic acid groups: at 1150 cm^{-1} (S=O) and 1030 cm^{-1} (S-O) in the grafted PAMPS and PSS confirm the attachment of these three polymers. The preliminary proton conductivities of PB-*g*-PAMPS and PB-*g*-PSS at room temperature are around 0.002 S/cm, which are measured by electrochemical impedance measurements. Due to the low load of grafted sulfonated compounds, the obtained conductivities of the two modified samples are much lower that (around 0.08 S/cm) of Nafion,[27] which is a perfluoropolymer with sulfonic acid groups.

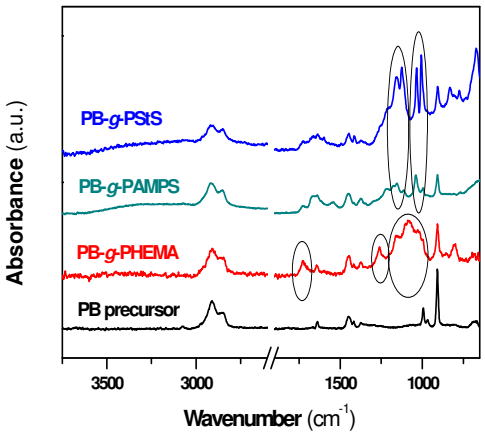

Figure 4.2. FT-IR spectra of the PB precursor and the modified samples PB-*g*-PHEMA, PB-*g*-PAMPS and PB-*g*-PSS.

After UV (wavelength of 365 nm) photoreaction of benzophenonyl bromoisobutyrate (BPBriBu) with nanoporous PB, the corresponding peaks for ester groups and tertiary alcohol (at 1170 cm^{-1}) can be found in FT-IR spectrum of initiator B (see middle curve in Figure 4.3). The peaks for ATRP grafted PPEGMA from initiator B was evident in the top curve of Figure 4.3.

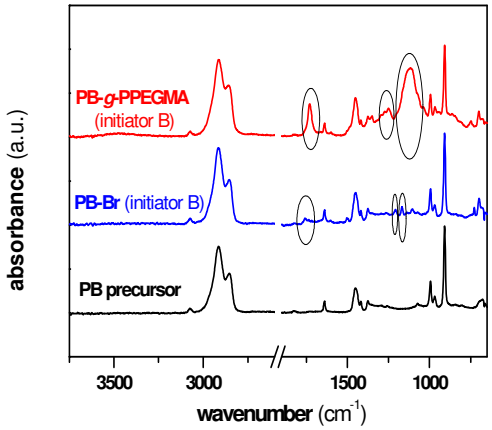

Figure 4.3. FT-IR spectra of the PB precursor, PB-Br (initiator B) and the modified sample PB-*g*-PPEGMA from initiator B.

4.3 Modification via click chemistry

Scheme 4-2 shows the routes of grafting MPEG by click chemistry onto nanoporous PB.

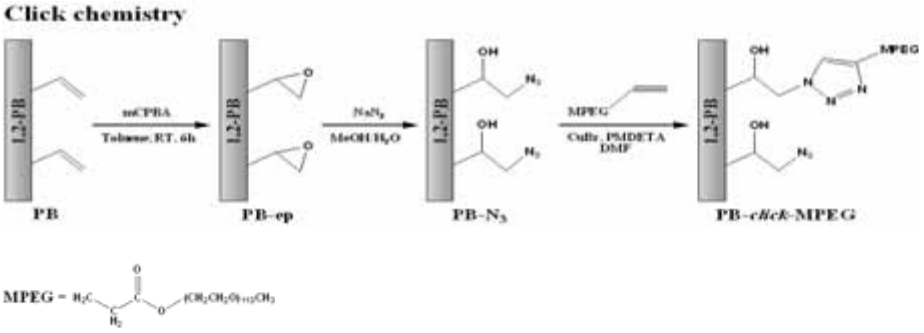

Scheme 4-2. Synthesis of PB-*click*-MPEG by click chemistry.

Figure 4.4 shows FT-IR spectra of modified samples by click chemistry. The characteristic peak for azide groups (N_3) at 2100 cm^{-1} can be found after reaction of NaN_3 with PB-ep films. The peak

related to PEG at 1110 cm^{-1} (C-O-C) confirms the immobilization of alkyne end-capped MPEG onto nanoporous PB by click reaction.

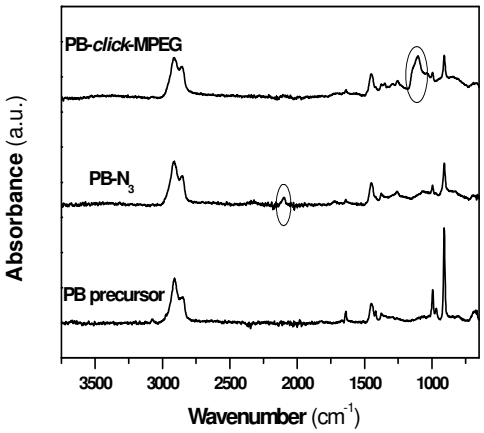

Figure 4.4. FT-IR spectra of the PB precursor, the PB-ep, and modified sample PB-*click*-MPEG.

4.4 Modified nanoporous polymers

In order to investigate the effect of the surface modifications nine nanoporous samples (the PB precursor, two PB-*g*-PHEMA (wet chem.), two PB-*g*-PPEGMA (wet chem.), one PB-*g*-PSS (wet chem.), one PB-*g*-PAMPS (wet chem.), one PB-*g*-PPEGMA (photo chem.) and one PB-*click*-MPEG) were placed into glass vials containing distilled water. The eight modified samples started to sink down to the bottom of their respective vials after a maximum time of 5 minutes. This is to be contrasted with the behavior of the PB precursor, which floated on the surface of the water showing no measurable water uptake for 3 months. The spontaneous uptake of water is a direct proof of hydrophilicity for the nanoporous materials.

Table 4.1 lists a series of volume fractions of the samples after each modification step and in the last column the water uptake for the final nanoporous samples. In parentheses in the first column, the reaction time of surface-initiated ATRP for each monomer is mentioned and also what type of chemical reaction was applied: wet chemistry, photchemistry or click chemistry. The volume fraction is expressed as V_m/V_0 where V_m is the volume of the sample or water uptake and V_0 is the

original volume of the PB-*b*-PDMS block copolymer.[13] The PB precursor has volume fraction of 59.2 %. For all the grafted components a density of 1 g/cm^3 was assumed.

Table 4.1. Cumulative volume fraction (v%) of various functional nanoporous samples by surface-initiated ATRP and click chemistry at different stages of modification (column 2-5) and water uptake (column 6) of the final modified samples. For simplicity, volume fractions were calculated assuming the mass densities of grafted materials to be 1 g/cm^3. The volume fraction of nanoporous PB was measured by methanol uptake. (Uncertainties are within 2%)

Monomer	PB-ep	PB-OH	PB-Br or (PB-N_3)	PB-g-polymer	water uptake
			ATRP		
HEMA (wet chem.) (0.5 h)	61.8	62.1	63.8	77.7	23.3
HEMA (wet chem.) (2 h)	61.8	62.1	63.8	92.6	11.8
PEGMA (wet chem.) (1 h)	61.8	62.1	64.0	71.4	28.5
PEGMA (wet chem.) (2 h)	61.5	61.8	64.1	90.2	14.3
NaStS (wet chem.) (14h)	61.7	62.1	64.0	74.3	27.0
AMPS (wet chem.) (3h)	61.7	62.1	64.0	74.0	26.9
PEGMA (photo chem.) (1 h)	-	-	61.6	74.3	23.4
			Click Chemistry		
MPEG (click chem.)	63.0	-	66.2	71.2	26.0

As seen in Table 4.1 the volume fraction of the grafted polyacrylates (PB-*g*-PHEMA and PB-*g*-PPEGMA) increases with increasing ATRP reaction time, which is in agreement with expectation. The volumes of water uptake for the modified samples shown in the last column are very close to the expected volumes. The samples prepared by wet chemistry typically show an accumulated volume fraction (sum of volume fractions of grafted nanoporous polymer sample and water uptake) of 104% for the long reaction times. The excess might be an artifact contributable to the real bulk densities of PPEGMA and PHEMA exceeding 1 g/cm^3.[14]

From the volume uptake of MPEG, the surface density of grafted MPEG by click chemistry could be calculated to be 3.9×10^{-2} chains/nm^2 by using the following equation:

$$SD\ (units/nm^2) = \frac{(v \times 100)/M_n \times N_A}{S \times 10^{18} \times 59.2 \times d_{PB}} \qquad (4.1)$$

where SD is surface density, v is the volume fraction of attached chemicals or polymers (can be read from Table 4.1), M_n is the molecular weight, N_A is Avogadro's number, S is the specific surface area (260 m^2/g) of nanoporous PB,[15] d_{PB} is the estimated mass density (1 g/cm^3) of cross-linked PB.

The amount of grafted polymer was 1.8 times the MPEG solution concentration and close to the observed equilibrium mass of MPEG adsorbed into the pores at same solution concentration. On the other side the total amount of MPEG captured in the pores after the end of the click reaction was 5 times the solution concentration. Therefore most of the MPEG chains present in the pores did not click and were washed away during the final rinsing. The surface densities of attached MPEG and $-N_3$ are 3.9×10^{-2} and 3 units/nm^2, respectively based on Equation 4.1. Only 1.3% of the azide groups ($-N_3$) are estimated to be reacted with alkyne groups attached to MPEG ($\equiv$–MPEG). A semiquantitative understanding of the low conversion of $-N_3$ can be reached by the following argument. Already attached chains reduce the accessibility of the unreacted $-N_3$ by steric hindrance. The transverse extension (parallel to the surface around the grafting point) of grafted MPEG in the pores is estimated from the radius of gyration of MPEG 5K (R_g ~ 1.8 nm) in DMF. The transverse area of grafted MPEG is approximately 10 nm^2. The excluded area under an assumption of total exclusion is roughly 40 nm^2. The number of $-N_3$ within 40 nm^2 is around 120 from a calculation based on dry volume uptake (column 4 in Table 4.1). This suggests that the probability of the 120 units reacting with a second MPEG chain is limited due to the steric hindrance ('shading') from the already clicked MPEG. A total exclusion only 1 out 120, or 0.8% of the $-N_3$ groups are accessible for MPEG based on the above estimation. This is in the same order of magnitude as the actual result of conversion. This is a conservative estimation, still providing a figure of the same order of magnitude as the actual result of conversion. The above estimation neglects possible effects of pore walls' curvature, being therefore strictly valid on a flat surface.

The confinement in the nanopores of diameter 14 nm may influence ATRP initiated from pore walls. In order to investigate this effect, polymerizations of PEGMA both in nanoporous PB-Br prepared by wet chemistry (heterogeneous) and in d_4-methanol solution (homogeneous) by using 2-EBP as initiator were conducted at the same temperature, monomer concentration and amount of catalyst. Figure 4.5 shows that a linear semilogarithmic plot of monomer conversion vs time was obtained within a polymerization time of 4 h in free methanol solution indicating the living/controlled nature of polymerization.

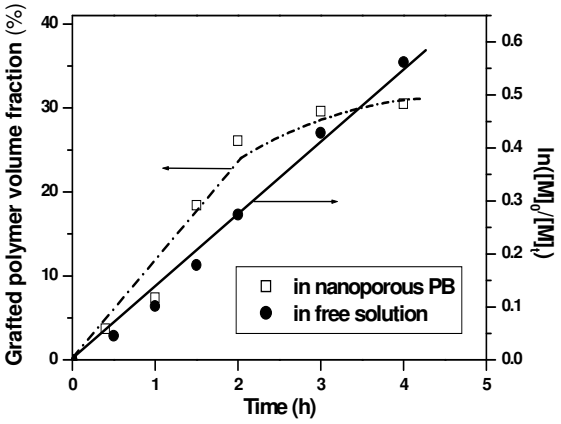

Figure 4.5. Effect of the polymerization time on surface initiated ATRP of PEGMA in nanopores (□) and plot of $\ln([M]_0/[M]_t)$ vs time for ATRP of PEGMA in d_4-methanol solution using 2-EBP as the initiator (●).

During the first 2 h the grafted polymer volume fraction also increased linearly with polymerization time. It slowed down after 2 h, which is probably related to the reaction kinetics entering a diffusion control regime. The conversion of PEGMA for the first 2 hours in heterogeneous conditions can be calculated as 6.3 times that in homogeneous conditions. Assuming equal kinetics of polymerization both under homogeneous and heterogeneous conditions up to 2 hours, the concentration of active bromoisobutyrate in heterogeneous conditions is 6.3 times that of 2-EBP in homogeneous conditions. Since the concentration of 2-EBP in homogeneous conditions is 3.5×10^{-4} mol/mL, the amount of initiated bromoisobutyrate in 1 mL of pores can be estimated to 2.2×10^{-3} mol. The surface density of active bromoisobutyrate is calculated as 3.5×10^{-1} chains/nm^2, which is also the surface density of grafted PPEGMA. The number-average molecular weights of grafted PPEGMA

in PB-*g*-PPEGMA (wet chem. 1h) and PB-*g*-PPEGMA (wet chem. 2h) could be calculated as 860 and 3050 kg/mol respectively. Comparing the surface density of active bromoisobutyrate obtained from the kinetics study with the surface density of attached bromoisobutyrate calculated from volume uptake (column 4 in Table 4.1), roughly 60% of attached bromoisobutyrate did initiate polymerization. The remaining 40% may be attached inside the matrix or sterically hindered on the pore walls.

The hydrophilicity of the modified nanoporous PB films was also substantiated by water static contact angle measurements. Figure 4.6 compares the water contact angle (θ) of the original and the four functionalized nanoporous polymers. The initial θ for PB was around 119°, and it decreased slightly after 2 min. After 20 min most of the water droplet had evaporated from the surface of PB. The case of the modified nanoporous samples prepared by wet chemistry is now discussed. After modification the films became hydrophilic, which led to an initial θ of about 76° for PB-*g*-PHEMA (wet chem. 0.5 h) and 60° for PB-*g*-PPEGMA (wet chem. 1 h). The θ for the two functionalized samples decreased further to 59° or 26°, respectively, after 2 min. The water drop disappeared entirely from the surfaces after 10 min or 3 min 45 s, respectively, due to capillary suction into the nanoporous films. The value of θ and the capillary suction time on PB-*g*-PPEGMA prepared by photochemistry were very close to the respective values observed for PB-*g*-PPEGMA (wet chemistry 1 h) prepared by wet chemistry. Apparently the larger amount of grafted PPEGMA by the photochemical path, 12.7% against the 7.4% grafted by the wet chemistry path, does not affect these parameters. At last the PB-*click*-MPEG sample shows the strongest hydrophilicity among the four modified samples, despite the only 5% volume increase due to polymer grafting. Its initial contact angle was lowest, 52°, and the suction of the water drop took the least time, 2 min 15 s. The determining factor for the observed hydrophilicity is the content of ethylene oxide in the grafted polymers. An increasing mass fraction of ethylene oxide in the grafted polymers, 0.35 (PHEMA) < 0.76 (PPEGMA) < 1.00 (PEG), qualitatively correlates with decreasing initial contact angle of water and with shorter capillary suction time.

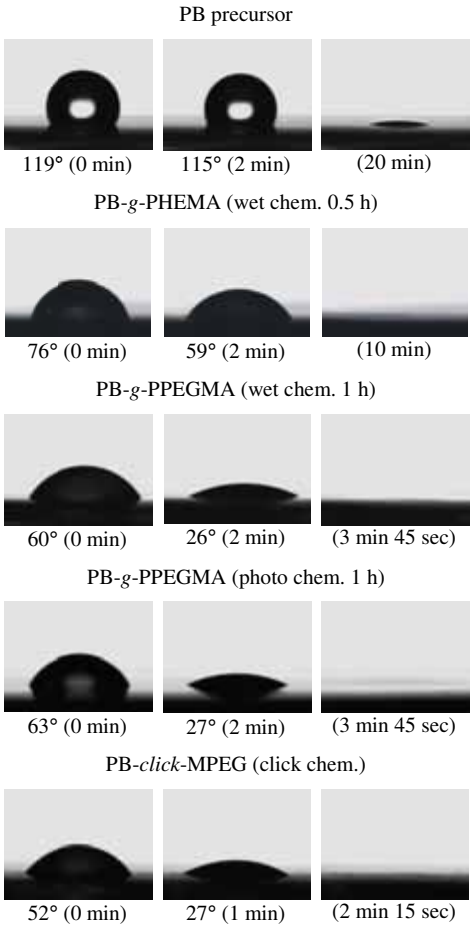

Figure 4.6. Water contact angle measurements for PB precursor, PB-*g*-PHEMA (wet chem. 0.5 h), PB-*g*-PPEGMA (wet chem. 1 h), PB-*g*-PPEGMA (photo chem. 1 h) and PB-*click*-MPEG.

Small angle x-ray scattering (SAXS) was used to investigate the morphology of nanoporous samples in the dry state after each modification step. The hydrophilic samples were also characterized in the presence of water. Figure 4.7 shows the resulting data for PB-*g*-PPEGMA (wet chem. 1 h). The 1-D scattering pattern of nanoporous PB precursor (curve a) is well described by models of gyroid morphology reported from literatures.[16-18] Specifically the intensity ratios of scattering peaks at {420}, {332}, {422} and {431} (relative q positions at $20^{1/2}$, $22^{1/2}$, $24^{1/2}$ and

$26^{1/2}$) to the principal scattering peak at {211} (relative q position at $6^{1/2}$) are similar to the predicted values which are around 1 %.[16,17]

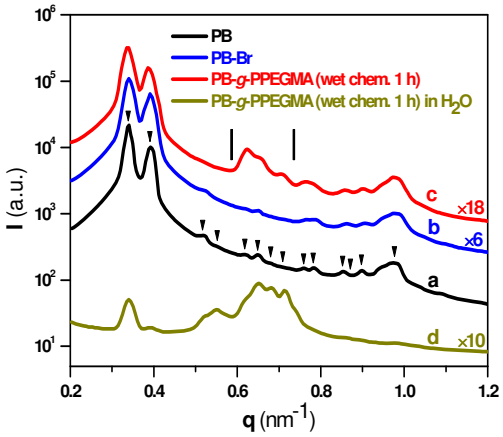

Figure 4.7. SAXS 1D profiles of (a) PB precursor, (b) PB-Br, (c) PB-*g*-PPEGMA (wet chem. 1 h) and (d) PB-*g*-PPEGMA (wet chem. 1 h) in H_2O. The intensity of some curves is shifted for clarity as indicated in the graph. (The marked positions have characteristic q ratios for gyroid morphology: $6^{1/2}$, $8^{1/2}$, $14^{1/2}$, $16^{1/2}$, $20^{1/2}$, $22^{1/2}$, $24^{1/2}$, $26^{1/2}$, $30^{1/2}$, $32^{1/2}$, $38^{1/2}$, $40^{1/2}$, $42^{1/2}$, $50^{1/2}$) The range of peaks mainly used in the discussion is marked by two black bars.

The q-position of the scattering peaks for the modified samples does not change. This proves that the gyroid structure and lattice spacing of the sample were preserved after the modification sequence. Nevertheless, due to the additional layer of grafted PPEGMA, a core-shell gyroid morphology is expected to be formed with an air-core, and PPEGMA-shell inside the PB-matrix. This three components system is similar to the one described in ref. 19. Looking at the same scattering peaks (relative q positions at $20^{1/2}$, $22^{1/2}$, $24^{1/2}$ and $26^{1/2}$) for the modified sample (curve c), the intensities increase in the same manner as described in the reference, but a quantitative analysis is very difficult. One of the reasons for this is that the scattering pattern of three components systems is much more difficult to be predicted,[19,20] mainly due to the missing knowledge of the interaction parameters that are required in the models. In the presence of water the pores are filled with liquid, electron density contrast between the pores and the polymers is reduced, leading to weaker scattering. The relative intensities of peaks at q positions of $14^{1/2}$, $16^{1/2}$, $20^{1/2}$, $22^{1/2}$, $24^{1/2}$ and $26^{1/2}$ to q^* position of $6^{1/2}$ become more enhanced after soaking in water, possibly

caused by the change of form factor of the core-shell structure[21] when PPEGMA-shell expands in the presence of water. The scattering patterns of other modified samples are similar to those of PB-*g*-PPEGMA (wet chem. 1 h) (data not shown).

Figure 4.8 shows the online SAXS 1D profiles which were recorded during the drying process of PB-*g*-PPEGMA (wet chem. 1 h) filled with water. The sample was dried under vacuum in the sample chamber of SAXS equipment.

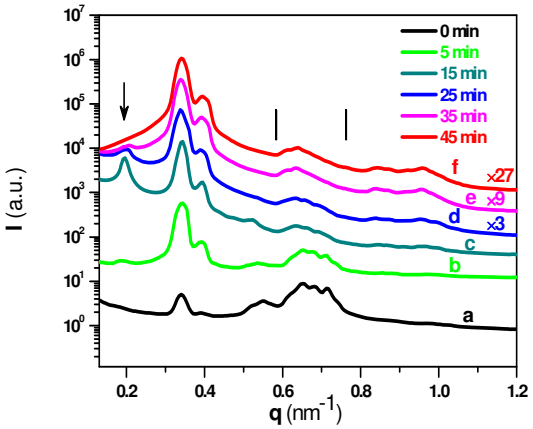

Figure 4.8. Time resolute SAXS 1D profiles of the drying process of PB-*g*-PPEGMA (wet chem. 1h) in H_2O. The intensity of some curves is shifted for clarity as indicated in the graph.

The *q*-position of the scattering peaks in the process is preserved. The scattering intensity is increasing for the first 15 min, indicating that water is sucked out of nano pores gradually. After 15 min, the scattering intensity reaches the maximum and remains there, suggesting that most of water has evaporated from pores. Surprisingly, an additional peak at lower *q* position, which is marked as an arrow in the figure, starts to appear during the drying process. The ratio of *q* positions of the additional peak to primary peak is $2^{1/2}$: $6^{1/2}$. The additional scattering peak is most likely from the {110} planes, which in principle generate a forbidden Bragg reflection in gyroid morphology. The gyroid structure is known to have bi separate continuous network, which can be illustrated from a computer-generated projection of the gyroid real space structure from Vigild et al. shown in Figure 4.9.[22] When the water in the pores of nanoporous PB-*g*-PPEGMA evaporates, the evaporation speed can be slightly different between the two networks at a small dimensional scale. This difference of

evaporation speed or content of water in the pores actually breaks the symmetry of bicontinuous network structure. As a result, the {110} planes become to allow the reflection. As seen in Figure 4.8, the relative intensity of the additional peak increases during the first 15 min and then starts to decrease. Finally the peak vanishes when the sample is totally dried after 45 min. The finding of the additional scattering peak at relative q position of $2^{1/2}$ confirms the existence of bicontinuous network in the gyroid morphology.

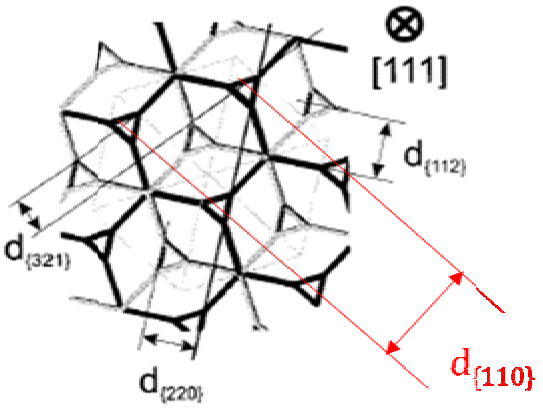

Figure 4.9. A computer-generated projection of the gyroid real space structure. A view along the [111] direction displaying {110}, {112}, {220}, and {321} planes.[22]

Transmission electron microscopy (TEM) was employed to further elucidate the structure of the samples. Figure 4.10 shows images of the nanoporous PB precursor, PB-*g*-PPEGMA (wet chem. 1h) and PB-*g*-PPEGMA (wet chem. 2h). All three images were observed nearly along the [111] direction, though with small deviation as indicated by Fourier transform images in the inserts. The center to center distances in the 'wagon wheel' pattern (36±2 nm for PB precursor, 37±1 nm for PB-*g*-PPEGMA (wet chem. 1h), 36±1 nm for PB-*g*-PPEGMA (wet chem. 2h)) calculated by using the trigonometric relationships were in good agreement with those obtained from SAXS analysis (twice the spacing of the {211} planes, 37 nm for all three samples). As seen in the figure, the gyroid morphology was fully preserved after modification. In the TEM images, the increased black in the gray scale corresponds to increased polymer in the electron beam path. The ratio of white areas was 1 : 0.95 : 0.39 for PB precursor, PB-*g*-PPEGMA (wet chem. 1h) and PB-*g*-PPEGMA (wet chem. 2h). The thickness of additional PPEGMA layer in PB-*g*-PPEGMA (wet chem. 1h) is

calculated as around 1 nm, and the resolution of TEM is not high enough to distinguish the difference between the sample and PB precursor. The significant reduction of the white area in the case of PB-*g*-PPEGMA (wet chem. 2h) suggests that much more pore space was occupied by grafted polymers after polymerization for 2 hours.

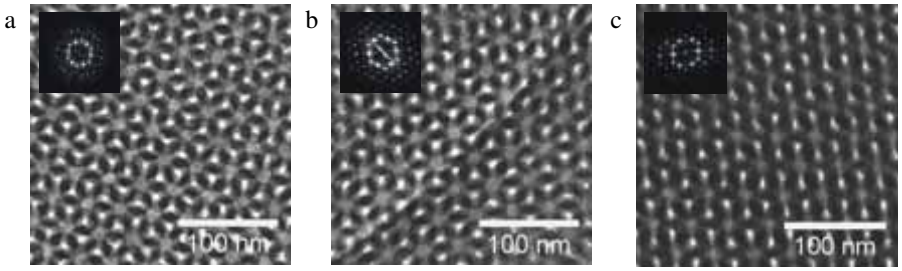

Figure 4.10. TEM images of (a) PB precursor, (b) PB-*g*-PPEGMA (wet chem. 1 h) and (c) PB-*g*-PPEGMA (wet chem. 2 h). The insets show Fourier transform of the TEM pictures.

4.5 Conclusion

Functionally controlled nanoporous polymer samples were prepared by surface-initiated ATRP and click chemistry. PHEMA, PPEGMA or MPEG in the increasing order of content of ethylene oxide units, and sulfonated polymers, PAMPS and PSS, were grafted onto the pore surface of nanoporous PB. The gyroid structure of PB precursor was preserved after modification as evidenced by SAXS and TEM. The hydrophilicity of the modified samples was verified by water contact angle and water uptake measurements. Two different methods were applied to immobilize the ATRP bromoester initiator onto the pore walls of cross-linked PB: (1) three-step chemical conversion of residual double bonds into bromoisobutyrate, and (2) photochemical functionalization with bromoisobutyrate groups. The methods in principle can be applied to any monomers, including functional ones, which can be polymerized by ATRP. Thus various surface functionalities may be inserted. It was also shown that click chemistry is an alternative method to modify nanoporous PB. Thus, the work presented in this chapter is expected to broaden the spectrum of tools to create functionalized nanoporous polymers with well defined morphologies.

4.6 Experimental

Materials. Gyroid nanoporous 1,2-polybutadiene (PB) films with pore diameter of 14 ± 1 nm and surface area of 260 ± 30 m^2/g used for this study were prepared from PB-*b*-PDMS by cross-linking PB block with dicumyl peroxide followed by removal of PDMS block with tetrabutylammonium fluoride. HEMA and THF were passed through a column of activated aluminum oxide, afterwards HEMA, THF, toluene, triethylamine (TEA) and *N,N*-dimethylformamide (DMF) were stirred over CaH_2 overnight and distilled before use. All other chemicals were received from commercial sources and used without further pretreatment.

Monolith Initiator Formation. Two different kinds of ATRP bromoester monolithic initiators were produced from the nano-porous PB material following one of the two procedures below. The initiators are designated as *Initiator A* and *Initiator B*.

Initiator A followed from a three-step chemical conversion of double bonds: The first step is epoxidation of the double bonds in the PB precursor. Four nanoporous PB films (0.7 cm× 0.7 cm× 0.03 cm) were prepared and placed into a round bottom flask together with 0.2 g of *meta*-chloroperoxybenzoic acid (*m*CPBA) and 5 mL of dry toluene under stirring. The mixture was stirred further for 6 hours at room temperature. The epoxidized films (PB-ep) were washed with toluene and THF, and then vacuum-dried. The second step is hydroxylation of the PB-ep films. The films were treated in 8.5 mL of hexane for 70 h at room temperature with 1 mL of hexane solution of 1 M diisobutylaluminum hydride (DIBAL-H).[23] The films were then washed successively with hexane, a 1:1 (v/v) mixture of 1 M HCl and methanol, and finally THF before drying. After formation of the PB films with OH groups (PB-OH) bromoisobutyryl bromide was attached to give the PB monolith initiator (PB-Br) by the same method as described previously.[24]

Initiator B followed from photochemical functionalization: The initiator was prepared by the UV photo reaction of benzophenonyl bromoisobutyrate (BPBriBu) which was synthesized according to literature.[25] The nanoporous PB films were submerged into a BPBriBu 170 mg/ml toluene solution for 4 hours. Then the films were placed into transparent glasses filled with nitrogen. After irradiation under UV of wavelength 365 nm at 32 °C for 1 hour, the films were washed with toluene and THF.

Surface-Initiated Polymerization. PEGMA and HEMA, AMPS and NaStS were graft-polymerized onto the nanoporous material by ATRP (heterogeneous polymerization). Similar procedures were

followed for the polymerization of the four monomers; the surface polymerization of PEGMA is described in the following. A Schlenk flask was charged with the nanoporous PB film with immobilized initiator, 13 mg of CuBr, 24 mg of 2,2'-bipyridyl (bpy), and 1.5 mL of methanol, and flushed with nitrogen for 10 minutes. 1.2 mL of PEGMA with M_n of 360 g/mol (average number of EO units is 6.2) was then added. Oxygen was removed by three freeze-pump-thaw cycles. The reactions were carried out at room temperature under nitrogen. The polymerization was stopped by immersing the Schlenk flask in an isopropanol/dry ice bath after desired time and the films were rinsed with methanol and THF. The monomer AMPS and NaStS were first dissolved in water. The pH value of the solution was adjusted to 9 ~10 by adding NaOH. Then the monomer solution was added to the methanol before ATRP.

Homogeneous polymerization of PEGMA. PEGMA was polymerized with ethyl 2-bromopropionate (2-EBP) as the initiator and deuterated-methanol as the solvent at room temperature by following typical ATRP procedures. The amounts of chemicals used are the following: 12.4 μL of 2-EBP, 13 mg of CuBr, 24 mg of bpy, 1.2 mL of PEGMA, and 1.5 mL of d_4-methanol.

Click Chemistry. PB-ep films, NaN_3 (0.3 g) and NH_4Cl (0.1 g) were placed in 10 mL of a 8:1 (v/v) mixture of methanol and H_2O, and the solution was refluxed at 80 °C for 24 hours. After reaction, the films were washed by a mixture of methanol and H_2O, and THF. The MPEG-alkyne was prepared by dicyclohexylcarbodiimide (DCC) coupling, using a commercially available MPEG (M_n = 5010, PDI = 1.1), 1.5 equiv of 4-pentynoic acid, DCC and 1.5 equiv of 4-(dimethylamino)pyridine (DMAP) relative to the hydroxyl end group of MPEG in dichloromethane at 0 °C. The click reaction was performed by using 0.33 g of MPEG-alkyne[26], 12 mg of CuBr, and 0.02 mL of *N*,*N*,*N*′,*N*″,*N*″-pentamethyldiethylenetriamine (PMDETA) in 5 mL of DMF at 40 °C for 40 hours.

Adsorption of MPEG on the nanoporous polymers. Nanoporous PB samples were submerged in 5 mL of DMF solution containing 0.33 g of MPEG under gentle stirring at 40 °C. The samples were taken out after 2 days and vacuum dried before weighting.

Online SAXS measurement of drying process. The modified sample PB-*g*-PPEGMA (wet chem. 1 h) filled with water was placed in a quartz capillary which had an open end. The capillary with the wet sample was then located in the SAXS sample chamber at beamline 7-11 at MAX-lab

synchronton radiation source with a wavelength of λ = 1.095 Å. The water was sucked out from the capillary by vacuuming the sample chamber.

Characterization Methods. FT-IR spectra were measured on a PerkinElmer SpectrumOne FT-IR spectrometer. ^{1}H NMR was run on a 300 MHz Bruker Avance DRX 300 instrument. SAXS was done at beamline 7-11 at MAX-lab synchrotron radiation source in Lund, Sweden, with a wavelength of λ = 1.095 Å. Water uptake experiments were carried out by placing dry samples in glass vials containing water and kept under gentle stirring at room temperature. After being submerged for a certain time a fine tissue was used to dry the surfaces of the sample quickly before weighing. The static contact angles of water droplets on the film surface were recorded at 25 °C using Contact Angle System OCA 20 from Dataphysics, Germany. TEM images were collected on a FEI TECNAI T20 operating at 200 kV, at the Center for Electron Nanoscopy of the Technical University of Denmark. Samples with 80 or 100 nm thickness were prepared on a LEICA ULTRACUT microtome using a DIATOME diamond knife at room temperature.

4.7 References

1. Xu, F. J.; Neoh, K. G.; Kang, E. T. *Prog. Polym. Sci.* **2009**, *34*, 719.
2. Zhao, B.; Brittain, W. J. *Prog. Polym. Sci.* **2000**, *25*, 677.
3. Edmondson, S.; Osborne, V. L.; Huck, W. T. S. *Chem. Soc. Rev.* **2004**, *33*, 14.
4. Jordan, R.; UIman, A. *J. Am. Chem. Soc.* **1998**, *120*, 243.
5. Jordan, R.; UIman, A.; Kang, J. F.; Rafailovich, M. H.; Sokolov, J. *J. Am. Chem. Soc.* **1998**, *121*, 1016.
6. Pyun, J.; Kowalewski, T.; Matyjaszewski, K. *Macromol. Rapid. Commun.* **2003**, *24*, 1043.
7. Fristrup, C. J.; Jankova, K.; Hvilsted, S. *Soft Matter* **2009**, *5*, 4623.
8. Lee, J. K.; Chi, Y. S.; Choi, I. S. *Langmuir* **2004,** *20*, 3844.
9. Bakbak, S.; Leech, P. J.; Carson, B. E.; Saxena, S.; King, W. P.; Bunz, U. H. F. *Macromolecules* **2006**, *39*, 6793.
10. Fleming, D. A.; Thode, C. J.; Williams, M. E. *Chem. Mater.* **2006**, *18*, 2327.
11. Daugaard, A. E.; Hvilsted, S.; Hansen, T. S.; Larsen, N. B. *Macromolecules*, **2008**, *41*, 4321.
12. Ndoni, S. ; Li, L.; Schulte L.; Szewczykowski, P. P.; Hansen, T. W.; Guo, F.; Berg, R. H.; Vigild, M. E.; *Macromolecules*, **2009**, *42*, 3877.
13. Guo, F.; Andreasen, J. W.; Vigild, M. E.; Ndoni, S. *Macromolecules* **2007**, *40*, 3669.
14. Yoshikawa, C.; Goto, A.; Ishizuka, N.; Nakanishi, K.; Kishida, A.; Tsujii, Y.; Fukuda, T. *Macromol. Symp.* **2007**, *248*, 189.
15. Szewczykowski, P. P. *Ph. D. Thesis*, DK-2800 Kgs. Lyngby, Denmark, **2009**.
16. Hajduk, D. A.; Harper, P. E.; Gruner, S. M.; Honeker, C. C; Kim, G.;Thomas, E. L.; Fetters, L. J. *Macromolecules* **1994**, *27*, 4063.
17. Matsen, M. W.; Bates, F. S. *Macromolecules* **1996**, *29*, 1091.
18. Ndoni, S.; Vigild, M. E.; Berg, R. H. *J. Am. Chem. Soc.* **2003**, *125*, 13366.
19. Shefelbine, T. A.; Vigild, M. E.; Matsen, M. W.; Hajduk, D. A.; Hillmyer, M. A.; Cussler, E. L.; Bates, F. S. *J. Am. Chem. Soc.* **1999**, *121*, 8457.
20. Matsen, M. W. *J. Chem. Phys.* **1998**, *108*, 785.
21. Eguchi, K.; Kaneda, I.; Hiwatari, Y.; Masunaga, H.; Sakurai, K. *J. Appl. Crystallogr.* **2007**, *40*, 264.
22. Vigild, M. E.; Almdal, K.; Mortensen, K.; Hamley, I. W.; Fairclough, J. P. A.; Ryan, A. J. *Macromolecules*, **1998**, *31*, 5702.

23. Marchand-Brynaert, J.; Jongen, N.; Dewez, J. L. *J. Polym. Sci., Part A: Polym. Chem.* **1997**, *35*, 1227.

24. Jankova, K.; Chen, X.; Kops, J.; Batsberg, W. *Macromolecules* **1998**, *31*, 538.

25. Huang, J. Y.; Murata, H.; Koepsel, R. R.; Russell, A. J.; Matyjaszewski, K. *Biomacromolecules* **2007**, *8*, 1396.

26. MPEG-alkyne was synthesized by Kaijia Yu. (Yu, K. *M. Sc. Thesis*, Technical University of Denmark, DK-2800 Kgs. Lyngby, Denmark, **2007**.)

27. Samms, S. R.; Wasmus, S.; Savinell, R. F. *J. Electrochem. Soc.* **1996**, *143*, 1498.

Chapter 5 Nanoporous 1,2-Polybutadiene Scaffold for Conductive Polymers

5.1 Introduction

Polymeric materials with highly ordered nanopores have attracted considerable interest due to their unique nanometer-scaled structures. Such NPs can be used as a scaffold to prepare various functional materials with controlled morphologies. The scaffold can be removed or remained after growth of new materials depending on the specific applications. For example, many research groups used NPs as templates to synthesize conducting metals, oxides or polymers inside pores, and then etched the templates to shrink the dimensions of (opto)electronic devices.[1-3] On the other hand, many applications may require existence of porous structures, so modifications on the scaffold surface without damaging pore structures or blocking pores are necessary. As described in the preceding chapter, a layer of different polymer brushes was attached onto the pore walls by either the '*grafting from*' or '*grafting to*' approaches to obtain new physicochemical properties. Besides the covalent bonding attachment, surface coating is an alternative way to modify the nanoporous polymers. In this chapter, an attempt to prepare conductive NPs via surface coating is discussed.

Polypyrrole (PPy) is one of the most common conducting polymers due to its simplicity of preparation, high conductivity and stability. A number of methods have been developed to produce PPy nanowires in both nanoporous organic and inorganic materials.[3-6] In addition to PPy nanowires, PPy ultrathin film incorporated onto nanopores of nanoporous polymers may also introduce conductivity to the previously insulating framework, and meanwhile the original porous structure is kept.

The fabrication of conductive monolithic NPs by coating PPy on nanopores of gyroid nanoporous 1,2-polybutadiene (PB) is presented here. Gyroid nanoporous PB is prepared by cross-linking PB block from the PB-*b*-PDMS diblock copolymer precursor and then etching away the PDMS block. Gyroid morphology provides a continuous network. PPy thin film is deposited on the nanopores by vapor phase polymerization (VPP) with iron (III) *p*-toluenesulfonate (Fe(III)pTs) as an oxidant. Cyclic voltammogram of PPy modified nanoporous PB shows a promising electro activity. The

prepared conductive nanoporous polymers may have interesting potential applications in sensing and catalysis due to their huge surface area.

5.2 Vapor phase polymerization of pyrrole in nanoporous PB

The vapor phase polymerization of pyrrole by using Fe(III)pTs as oxidants is shown in Scheme 5-1.

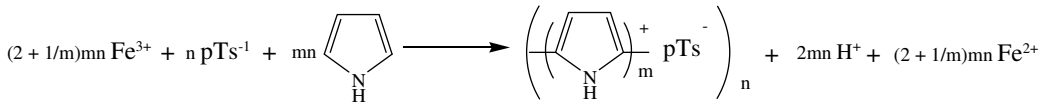

Scheme 5-1. Reaction between pyrrole monomer and Fe(III)pTs.

Fe(III)pTs oxidatively polymerizes pyrrole and incorporates pTs ions in the polymer as the 'dopant'.[7] 1/m is the degree of doping, which is typically around 0.25 for electrochemically deposited PPy.[8] This means 2.25 mole of Fe^{3+} is consumed to polymerize each mole of pyrrole. Degrees of doping of 0.23 and 0.31 haven been obtained for PPy synthesized by using Fe(III)pTs.[7,9] Our procedure for preparation of conductive NPs films from original block copolymers is outlined in Scheme 5-2.

Scheme 5-2. Schematic illustration of the preparation of conductive ordered nanoporous polymers.

The Fe(III)pTs was chosen as an oxidant here. Winther-Jensen et al. has reported that by using Fe(III)pTs oxidant VPP of pyrrole can leave very smooth and coherent coatings on a flat surface.[8] Gyroid morphology is known for its bicontinuous network, so it is easy accessible to gases and liquids, and probably less apt to have pore blockages.[10] The combination of VPP of pyrrole with Fe(III)pTs oxidant and gyroid morphology of nanoporous PB is used in this work to make continuous conductive PPy coatings throughout the nanopores. Talbe 5.1 lists the mass uptake of

PPy in nanoporous PB. From Table 5.1, we can see that the mass of PPy in nanoporous PB increases with oxidant concentration. Nevertheless, the deposited amounts for the four samples don't fit the expected values. One possible reason for this discrepancy could be that Fe^{3+} may be possibly regenerated by the air oxidation of Fe^{2+}.[3]

Table 5.1. Mass uptake of nanoporous PB with PPy

Sample	Concentration of Fe(III)pTs solution (%)	Mass uptake[a] (%)	Expected mass uptake[b] (%)
PB-PPy-I	2.5	0	0.1
PB-PPy-II	5	0.6	0.2
PB-PPy-III	10	1.3	0.4
PB-PPy-IV	20	2.0	0.8

[a] It is measured after films are washed in ethanol, and the reference is the mass of nanoporous PB precursor. [b] Expected value is calculated based on assumptions that no Fe(III)pTs loss during the loading process and 2.23 mole of Fe(III)pTs is consumed per mole of pyrrole.

To obtain evidence of PPy impregnation into nanoporous PB, FT-IR spectra of the film before and after modification were recorded. As shown in Figure 5.1, compared to the spectrum of the PB precursor, additional characteristic peaks associated with PPy appear in the modified film: PB-PPy-III at 1550 cm^{-1} (ring stretching), 1180 and 1040 cm^{-1} (in-plane deformation of C-H bond). Furthermore, intensities of the three characteristic PPy peaks increase with increasing concentration of Fe(III)pTs. This is an indication that more PPy would be formed when more Fe(III)pTs is employed.

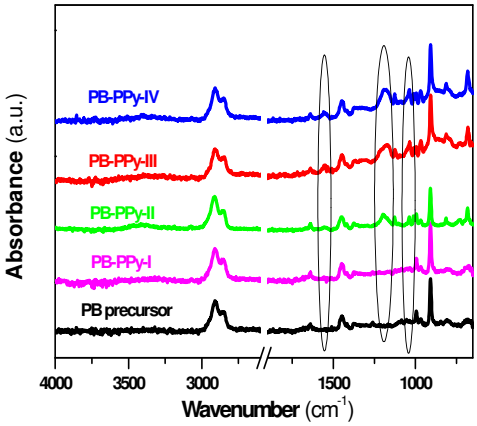

Figure 5.1. FT-IR spectra of PB precursor and PB-PPy-I, II, III, IV.

Ultra Violet Visible (UV-Vis) spectroscopy was further employed to confirm the presence of PPy in nanoporous PB. Figure 5.2 shows that the PB precursor does not absorb any light in the range from 350 to 900 nm. After modification, at 430 nm the typical $\pi - \pi^*$ absorption of conjugated PPy takes place. In addition, a broad band at 850 nm can be assigned to an extended conjugation in the backbone of the PPy. As expected, the film containing more PPy absorbs more in these two broad ranges.

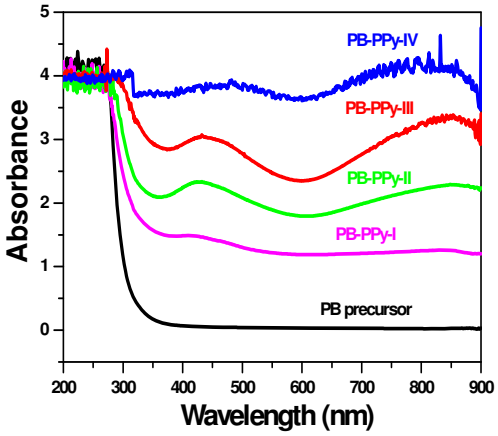

Figure 5.2. UV-Vis spectra of PB precursor and PB-PPy-I, II, III, IV.

To investigate the thickness of PPy coating on the pore walls, PPy thin films were prepared on glass slides at same conditions as for nanoporous PB. Figure 5.3 shows the relationship between the coating thickness and absorbance of the coating at 430 nm. Based on this relation, the average coating thickness on pore walls of nanoporous PB can be calculated. Values for the four samples are smaller than 1 Å, which means that the pore walls are not covered completely, and distribution of the coating is not homogeneous.

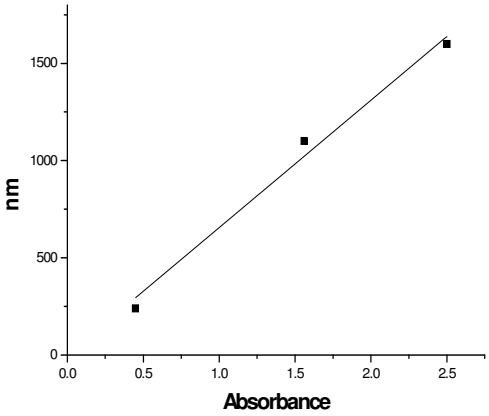

Figure 5.3. Relationship between PPy coating thickness and absorbance of the coating at 430 nm.

The calculated values are also close to the results obtained from the mass uptake calculation by using the following equation:

$$D(\text{Å}) = \frac{m/d_{PPy} \times 10^{24}}{S \times 10^{20}} \qquad (5.1)$$

where D is the coating thickness, m is the mass uptake of PPy (can be obtained from Table 5.1), d_{PPy} is the mass density (1.5 g/cm^3) of PPy,[11] and S is the specific surface area (260 m^2/g) of nanoporous PB.

PPy inside network of the nanoporous PB was investigated by Raman spectroscopy with 632.8 nm diode laser excitation on a 300 lines/mm grating at room temperature on the cross section of PB-PPy-III. Raman spectrum in Figure 5.4 shows a typical spectrum of PPy, similar to that of pure PPy

polymerised under identical conditions. The peak at 1590 cm^{-1} may be due to C-C and C=C ring stretching. The broad peak at 1380 cm^{-1} may be attributed to C-H and N-H in plane bending vibration. The peak at 1060 cm^{-1} may be associated to C-H in plane deformation. The peak at 930 cm-1 may be related to the ring deformation. This not only confirms that the resulting composite material contains PPy, but also indicates that PPy coating has been incorporated into the whole thickness of the nanoporous PB.

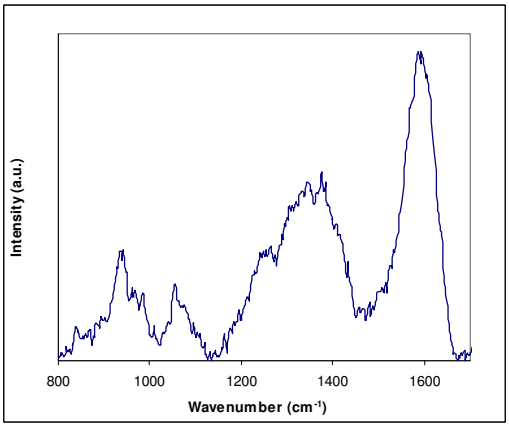

Figure 5.4. Raman Spectrum of PB-PPy-III with a 632.8 nm laser excitation and a 300 lines/mm grating.

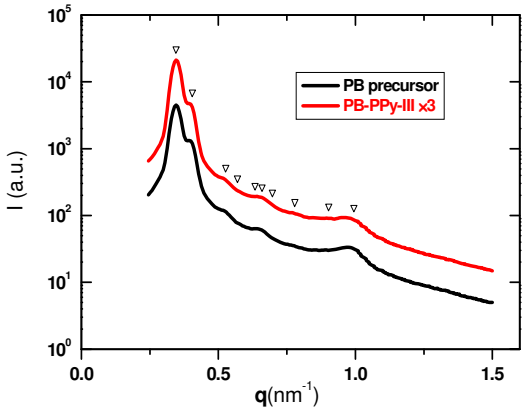

Figure 5.5. 1D SAXS profiles of PB precursor and PB-PPy-III. The (211), (220) and other characteristic peaks for gyroid structure are marked.

SAXS was used to investigate the morphology of nanoporous PB after modification. Figure 5.5 shows 1D scattering curves for the nanoporous PB precursor and PB-PPy-III. The ratio of the peak positions is characteristic for gyroid morphology. After VPP of pyrrole, the position of the scattering peaks PB-PPy-III does not change. This proves that the gyroid structure and lattice spacing of the sample were preserved during the modification. Scattering patterns of other modified samples are the same to that of PB-PPy-III (data not shown). TEM was employed to directly visualize the nanoporous structure. Figure 5.6 shows images of the PB precursor and PB-PPy-III. Both images were observed nearly along the [111] direction. The center to center distances in the typical "wagon wheel" pattern (36±2 nm for PB precursor and 36±1 nm for PB-PPy-III) calculated by using the trigonometric relationships were in good agreement with those obtained from SAXS analysis (twice the spacing of the {211} planes, 37 nm for both samples). There is no observation of blocked pores or grainy structure of PPy particles in the pores through over the area of 1.5 μm×1.5 μm in TEM picture of PB-PPy-III. This confirms that the gyroid morphology and open pores were fully preserved after incorporation of PPy and that PPy were deposited onto the nanopore wall surfaces.

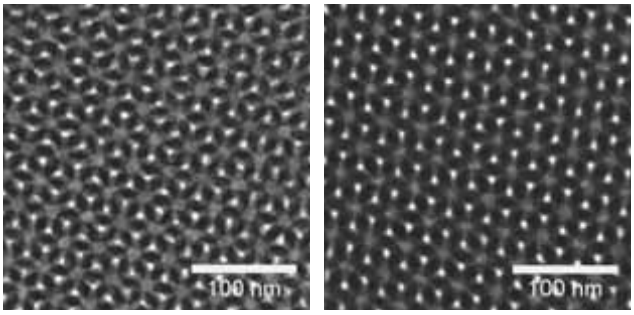

(a) (b)

Figure 5.6. TEM images of (a) PB precursor and (b) PB-PPy-III.

Figure 5.7 shows the cyclic voltammogram of PB-PPy-III electrode in 1.0 M $NaNO_3$ solution. It displays a typical stable redox couple (labelled A & B), which could be assigned to the PPy backbone. Even though the PPy does not cover the pore walls completely, partially continuous PPy coating exists in the network. That is why the sample shows the good electro activity. This suggests that the PPy/NPs has a potential as novel kind of nanoporous electromaterials.

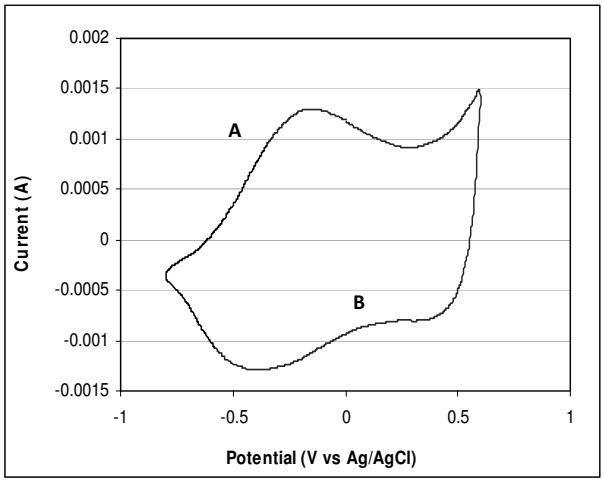

Figure 5.7. Cyclic voltammogram of PB-PPy-III. Range: -0.8 V to +0.6 V. Scan rate: 50 mV s^{-1}.

5.3 Conclusion

Conducting PPy thin coatings on nanopores of nanoporous PB are obtained by using vapor phase polymerization with ferric *p*-toluenesulfonate as oxidant. The highly ordered porous structure of PB precursor was preserved after modification as shown by SAXS and TEM. After incorporation of PPy coatings, previously insulating nanoporous polymers became conductive as verified by cyclic voltammogram. This method provides a general approach for producing conductive nanoporous polymers, which will have significant potential to be a novel nanometer-scaled electronic device.

5.4 Experimental

Materials. Colorless transparent gyroid nanoporous 1,2-polybutadiene (PB) monoliths (2 cm× 1 cm× 0.03 cm) with pore diameter of 14 ± 1 nm, surface area of 260 ± 30 m^2/g and porosity of 40 % used for this study were prepared from PB-*b*-PDMS by cross-linking the PB block with dicumyl peroxide followed by removal of the PDMS block with tetrabutylammonium. All other chemicals were received from Sigma-Aldrich and used as received.

VPP of pyrrole. Fe(III)pTs solutions with concentration between 2.5% and 20% in ethanol were prepared. Nanoporous PB films were soaked in the Fe(III)pTs solutions for 30 min. When the films were taken out from oxidant solutions, the outside of the samples was washed with ethanol to remove excess Fe(III)pTs on the outside surface. The oxidant filled films were put into an oven at 80 – 100 °C to avoid crystallization of Fe(III)pTs before dry. After 5 min the solvent evaporated and the films became brownish. The films were then placed into a sealed chamber saturated with pyrrole vapors. After few minutes the color of the films changes from brown to black, indicating the formation of PPy. After 30 min the films were taken out of the vapor chamber and placed into a petri dish to dry in air for 30 min before they were washed thoroughly in ethanol. VPP of pyrrole on glass slides was prepared in the same procedure as described for nanoporous PB.

Characterizations. FT-IR and UV-Vis spectra were measured at room temperature on SpectrumOne FT-IR and Lambda 5 UV/VIS spectrometers, both from PerkinElmer. SAXS was done at Risø-DTU using Cu Kα x-rays with a wavelength of $\lambda = 1.54$ Å. Polypyrrole was characterized by Raman spectroscopy using a JOBIN YVON HR800. Confocal Raman system with 632.8 nm diode laser excitation on a 300 lines/mm grating at room temperature was employed. TEM images were collected on a FEI TECNAI T20 operating at 200 kV, at the Center for Electron Nanoscopy at the Technical University of Denmark. Samples with 80 or 100 nm thickness were prepared on a LEICA ULTRACUT microtome using a DIATOME diamond knife at room temperature. Electrochemical testing of the polypyrrole modified NPs was performed on an electrochemical hardware system comprising of an EG&G PAR 363 Potentiosts/Galvanostat, a MacLab 400 with Chart v. 3.5.7/ EChem v.1.3.2 software (AD Instruments). The cyclic voltammetry was carried out at room temperature in a three-electrode cell, using PPy/NPs as the working electrode, Platinum mesh and Ag/AgCl as the auxiliary and reference, repectively. The thickness of PPy coating on glass slides was measured by a DekTak profilometer.

5.5 References

1. Crossland, E. J. W.; Kamperman, M.; Nedelcu, M.; Ducati, C.; Wiesner, U.; Smilgies, D. M.; Toombes, G. E. S.; Hillmyer, M. A.; Ludwigs, S.; Steiner, U.; Snaith, H. J. *Nano Letter* **2009**, *9*, 2807.
2. Kim, D. H.; Sun, Z.; Russell, T. P.; Knoll, W.; Gutmann, J. S. *Adv. Funct. Mater.* **2005**, *15*, 1160.
3. Johnson, B. J. S.; Wolf, J. H.; Zalusky, A. S.; Hillmyer, M. A. *Chem. Mater.* **2004**, *16*, 2909.
4. Bein, T.; Enzel, P. *Angew. Chem. Int. Ed.* **1989**, *28*, 1692 –1964.
5. Ikegame, M.; Tajima, K.; Aida, T. *Angew. Chem. Int. Ed.* **2003**, *42*, 2154-2157.
6. Guo, R.; Li, G.; Zhang, W.; Shen, G.; Shen, D. *ChemPhysChem* **2005**, *6*, 2025-2028.
7. Walker, J. A.; Warren, L. F.; Witucki, E. F. *J. Polym. Sci., Part A: Polym. Chem.* **1988**, *26*, 1285.
8. Wynne, K. J.; Street, G. B. *Macromolecules* **1985,** *18*, 2361.
9. Winther-Jensen, B.; Chen, J.; West, K.; Wallace, G. *Macromolecules* **2004**, *37*, 5930-5935.
10. Ndoni, S.; Vigild, M. E.; Berg, R. H. *J. Am. Chem. Soc.* **2003**, *125*, 13366.
11. De Bruyne, A.; Delplancke, J. L.; Winand, R. *J. Appl. Electrochem.* **1997**, *27*, 867.

Chapter 6 Cross-linked 1,2-Polybutadiene with Reversible Nanoporosity

6.1 Introduction

Previous chapters focused on the attachment of various chemical functionalities into NPs by different methods. This chapter will pay attention to a unique physical functionality possessed by cross-linked NPs.

As described in Chapter 3, nanoporous PB from PB-*b*-PDMS can be prepared by cross-linking PB block and etching the PDMS block. Different cross-linking degrees can be achieved by adjusting the amount of cross-linker and the cross-linking time. SAXS and methanol uptake results showed that the pore stability is dependent on the mechanical strength of the remaining block, PB. If the cross-linking degree of PB is not sufficiently high, the pore will be collapsed. Recently Szewczykowski et al. first reported that nanopores can be recovered when the collapsed polyisoprene matrix is in the gel state.[1] Inspired by this work, a collapsed PB matrix was prepared by cross-linking the matrix at a very low degree. When the collapsed PB matrix is exposed to a good solvent, a gel with well defined nanopores can be generated. Due to its large pore volume, ordered bicontinuous pore structure and high surface area, this gel shows a promising future for load-release applications. It opens a new application window for designing and synthesizing chemical delivery, particularly drug delivery, systems.

6.2 Cross-linking

The 1,2-PB-*b*-PDMS block copolymer precursor used here is BD14, which has a gyroid morphology at 140 °C. Two different cross-linking conditions were used to cross-link BD14 samples: 0.5 mole DCP per mole double bonds, cross-linking at 140 °C for 1h for sample BD14-x1; 2 mole DCP per mole double bonds, cross-linking at 140 °C for 2h for sample BD14-x4. During the cross-linking, 65% and 15% of double bonds were lost for BD14-x1 and BD14-x4, respectively as indicated by FT-IR spectra shown in Figure 6.1. The way how to calculate the fraction of consumed double bonds from FT-IR spectra has already been described in Chapter 3. According to the

previous studies on relation between Flory cross-linking degree and fraction of consumed double bonds during the cross-linking, the BD14-x4 has a lower cross-linking degree than BD14-x1. After etching of PDMS, BD14-x4e and BD14-x1e lost respectively 41 % and 40 % of mass, which had good agreements with the original mass fraction of PDMS in the block copolymer. The mass loss and disappearance of characteristic absorption peaks for PDMS in FT-IR spectra substantiated the quantitative removal of the PDMS block.

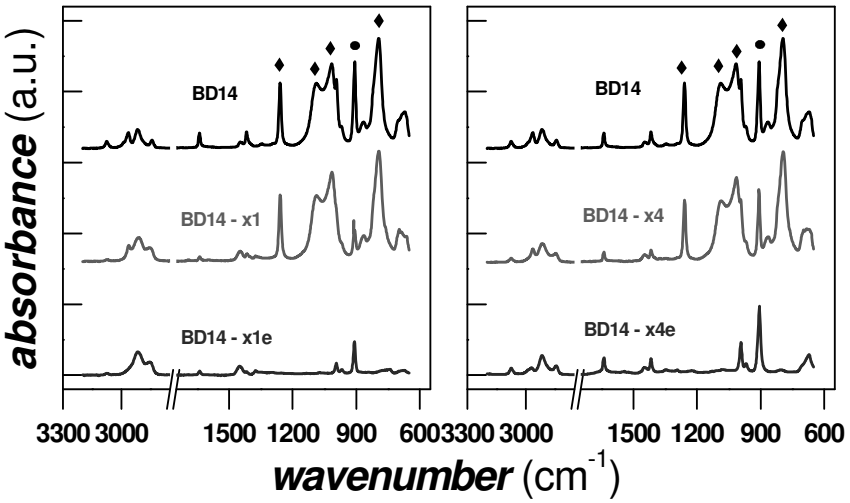

Figure 6.1. FT-IR spectra of BD14 precursor, cross-linked samples BD14-x1 and BD14-x4, and etched samples BD14-x1e and BD14-x4e.

6.3 Structures

Structural features of BD14-x1e and BD14-x4e were investigated by methanol uptake and SAXS measurements. Methanol can exclusively penetrate the porous volume of PB as described before. Within 2 min BD14-x1e took up methanol to volume fraction of 40%, which is very close to the volume fraction of PDMS (39%). It indicates the existence of pores in BD14-x1e. There was no methanol uptake for BD14-x4e over one week, showing pores are collapsed in the sample. Figure 6.2 depicts SAXS 1D profiles presenting the three steps of preparation for these two samples

(Figure 6.2 a for BD14-x1e, and Figure 6.2 b for BD14-x4e). The scattering profile from precursor polymer BD14 at room temperature shows the lamellar structure with the presence of scattering peaks at ratios of 1, 2 and 3. After cross-linking at 140 °C, the primary peak for the two samples are shifted to higher q values and the higher order lamellar peaks at 2 and 3 q^* disappear, while the second order reflection of the gyroid structure emerges at $(8/6)^{1/2}$ q^*. The scattering vector length increases from 0.290 nm^{-1} before cross-linking to 0.340 and 0.310 nm^{-1} after cross-linking for BD14-x1 and BD14-x4 respectively. The shift is caused by shrinkage of the matrix as a result of the cross-linking. With a higher cross-linking degree, shrinkage is expected to be more pronounced, so that the scattering vector length would shift towards a larger value. After etching, the scattering intensity for BD14-x1e has increased 2-3 orders of magnitude, due to the substitution of PDMS with vacuum, which gives an increased electron density contrast. The ratio of scattering peaks confirms that the gyroid morphology was preserved after etching PDMS. The position of primary peak changes slightly from 0.340 nm^{-1} before etching to 0.343 nm^{-1} for BD14-x1e. For BD14-x4e, there is no nanostructure which can be observed by SAXS, confirming the sample was totally collapsed after etching. The highest possible q value of scattering from BD14-x4e is 0.380 nm^{-1} when the pore size is infinitely small. The value is calculated based on an assumption that the volume of cross-linked PB matrix does not change during the etching process.

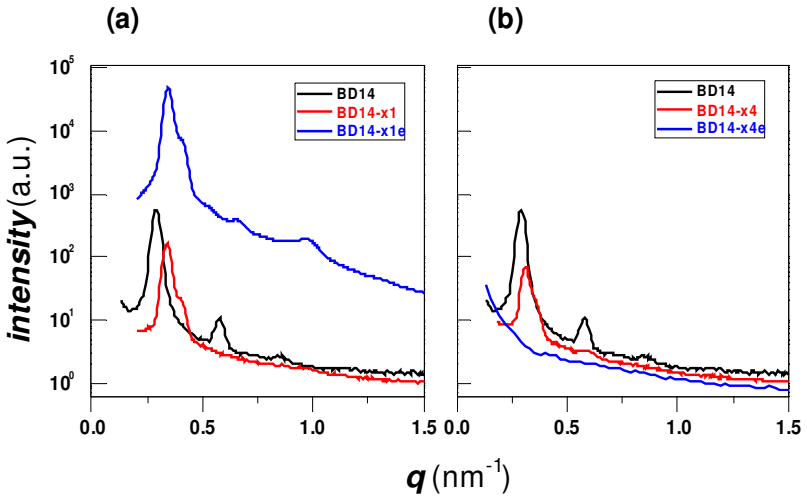

Figure 6.2. SAXS 1D profiles during three steps of preparation for BD14-x1e, and BD14-x4e.

6.4 Swelling-drying cycles

In order to check whether collapsed PB polymers have an ability to reproduce the nanoporous structure in the gel state, BD14-x4e (SLD=0.48 × 10^{10} cm^{-2}) was submerged into chloroform (SLD=2.38 × 10^{10} cm^{-2}) followed by drying with nitrogen flow. The swelling-drying process was recorded by in-situ SANS measurement. Figure 6.3 shows time-resolved SANS data of a swelling-drying process. In order to illustrate the process more clearly, changes of peak position q^* and main peak intensity I_{max} with time are shown in Figure 6.4. There is no scattering peak when the sample was dry (see front profile in Figure 6.3 a). After the sample was in chloroform for 1 min, a broad weak peak appears at 0.37 nm^{-1}. Scattering peaks start to show up more clearly after 2 min, and the peak position q^* gradually deceases with time and reaches minimum value of 0.28 nm^{-1} after 8 min (see Figure 6.4 a). The decrease of q^* suggests an increase of real space of the sample and domain spacing of the equilibrium state can be calculated as 22 nm. Meanwhile, the scattering intensity increases from the beginning and reaches maximum value of around 40 cm^{-1} after 9 min. This could be associated with the development of contrast between the swollen PB-matrix and solvent-filled cavities, which were opened up by chloroform. Apparently, BD14-x4e exhibits the memory of nano structure of its precursor, BD14-x4. The scattering profiles during sample drying are given in Figure 6.3 b. The peak position q^* increases and scattering intensity decreases over time. After nitrogen flow for 15 min, the peak is almost gone. This can be interpreted as a closing process of nano pores. The profile at the front is the scattering from the sample which is dried in vacuum for 24 h. After the swelling-drying cycle, the scattering of the sample is back to its original state. These profiles show the swelling-induced nano structure of BD14-x4e disappears during drying.

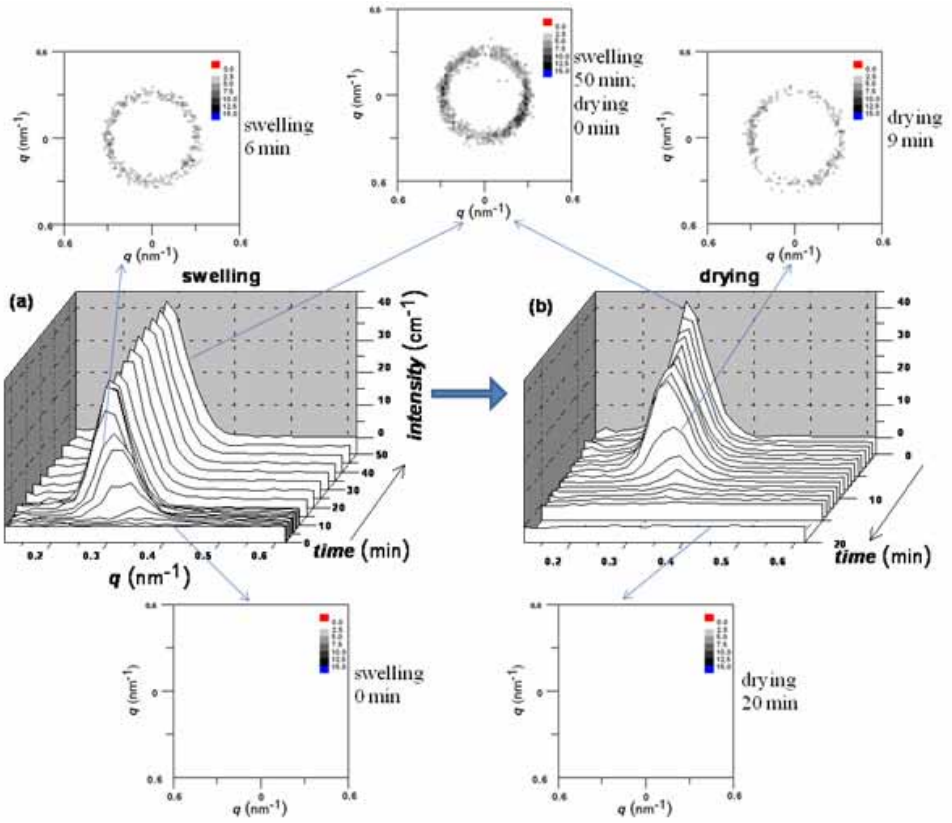

Figure 6.3. Time-resolved SANS data of a swelling-drying process for BD14-x4e.

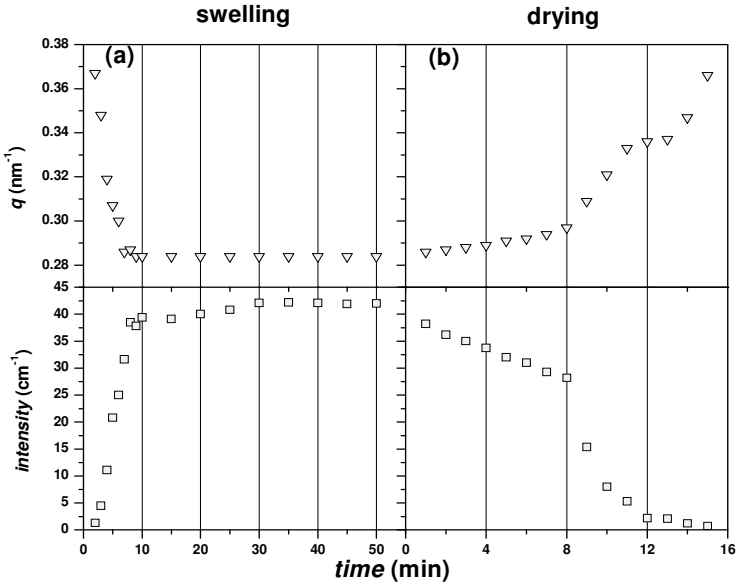

Figure 6.4. Time evolution of changes of primary peak position q^* (upper panel, open triangles) and main peak intensity I_{max} (lower panel, open squares) during the (a) swelling and (b) drying process of BD14-x4e. The data is originally from Figure 6.3.

6.5 Load and release of *d*-PEG

Load and release application of collapsed PB polymers were tested by using big molecules, deuterated-poly(ethylene glycol) (*d*-PEG) (SLD=6.29 × 10^{10} cm^{-2}) with Mn of 5000 g/mol. Figure 6.5 shows the time evolution of the SANS pattern for loading PEG, drying and releasing PEG process of BD14-x4e. Again, changes of peak position q^* and main peak intensity I_{max} with time in the whole process are shown in Figure 6.6. The sample was submerged in 100 mg/ml *d*-PEG in chloroform solution and recorded online by SANS. From Figure 6.5 a and Figure 6.6 a, we can see that the peak position q^* decreases and reaches minimum value of 0.29 nm^{-1} after 10 min. This q^* value is close to the obtained q^* value (0.28 nm^{-1}) during the swelling experiment. From the q^* value, 0.29 nm^{-1} and highest possible value, 0.38 nm^{-1}, the volume swelling ratio can be calculated as 2.25. The peak intensity increases up to 48 cm^{-1} for the first 7 min, and then decreases during the following 3 min and reaches plateau at 43 – 44 cm^{-1} afterwards. We could not find the similar

'overshoot' phenomenon on peak intensity in the swelling experiment of BD14-x4e. This phenomenon must be related to *d*-PEG, which has a higher SLD than chloroform and PB matrix, but unfortunately reasonable explanations are missing here. More studies on kinetics of diffusion of *d*-PEG solution into nanopores and PB matrix may be helpful to understand it. The stabilized peak intensity of 43 – 44 cm^{-1} is slightly larger than the maximum intensity (40 – 42 cm^{-1}) obtained during the swelling experiment. This slight intensity increase might be caused by existence of *d*-PEG in pores, which introduces a larger scattering contrast between the pores and matrix.

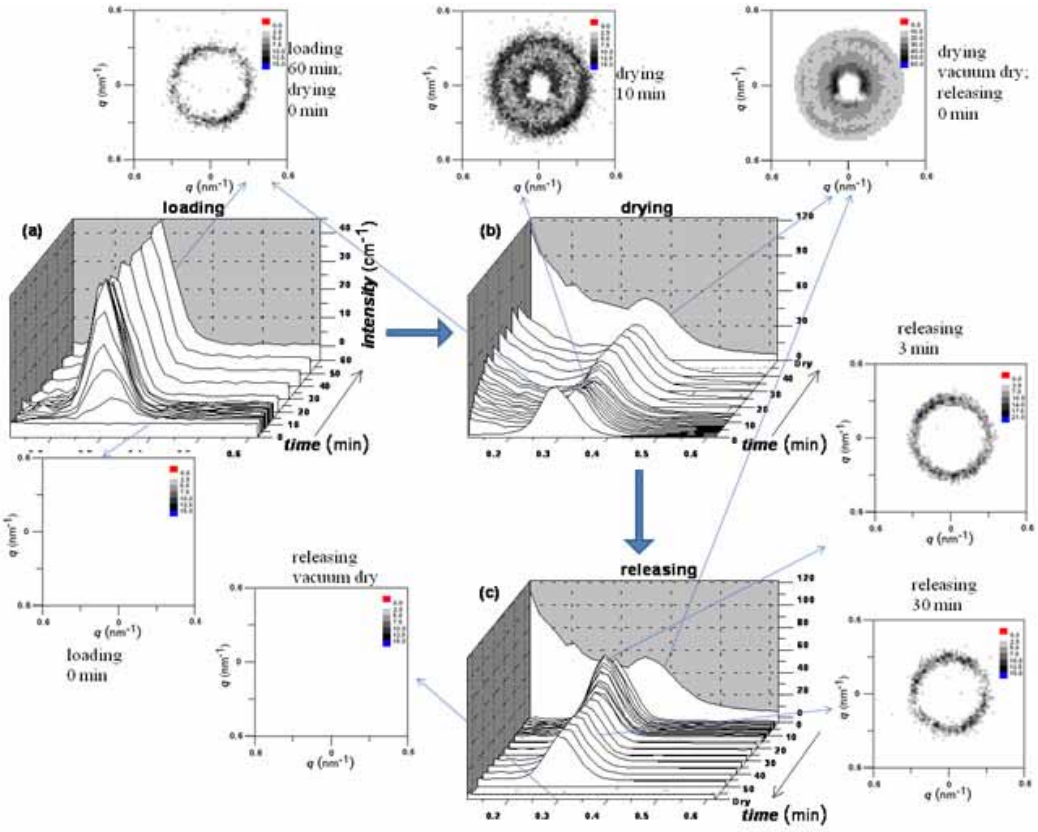

Figure 6.5. Time-resolved SANS data of *d*-PEG loading-releasing process for BD14-x4e.

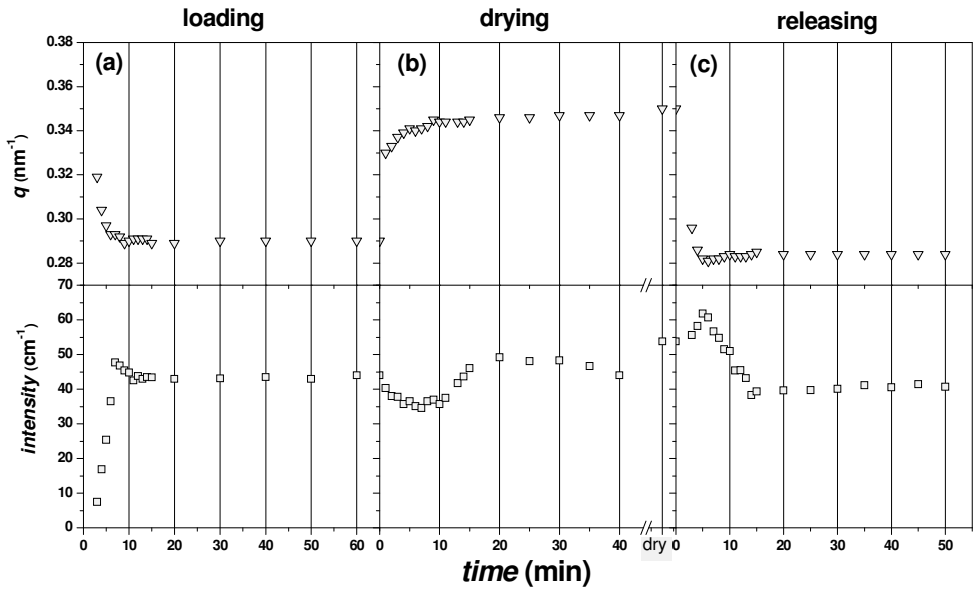

Figure 6.6. Time evolution of changes of primary peak position q^* (upper panel, open triangles) and main peak intensity I_{max} (lower panel, open squares) during the (a) loading *d*-PEG, (b) drying and (c) releasing *d*-PEG process of BD14-x4e. The data is originally from Figure 6.5.

After 4 h, the *d*-PEG solution was sucked out by using syringe and the sample was dried with nitrogen flow. As shown in Figure 6.5 b and Figure 6.6 b, the peak position q^* increases with time and reaches maximum value of 0.35 nm^{-1} after it was dried under vacuum. It shows that pores reduce in size over time, but do not varnish even when the sample was completely dry, suggesting *d*-PEG molecules were trapped in the pores. Intensity of the peak decreases till 34 - 35 cm^{-1} for first 10 min and afterwards increases over time till 53 cm^{-1} when it was totally dry. Chloroform in pores is expected to evaporate faster than in matrix. Dramatic reduction in volume fraction of pores to matrix may cause the decrease of intensity, even the scattering contrast between pores and matrix become lager over the whole drying process due to existence of *d*-PEG. After some time, the change in scattering contrast becomes a dominant factor, so the intensity starts to increase. Furthermore, scattering at a low q range appears and intensity increases along the drying process. One of the possible explanations is that during the evaporation of chloroform blobs of *d*-PEG with different sizes may be formed. These heterogeneous blobs give the scattering over the whole q

range, particularly with strong scattering at low *q* values. If we look at profiles more closely, an additional weak peak can be found at around 0.20 nm^{-1} from scattering profiles after drying for 20 min. The ratio between the position of this weak peak to that of the main peak is 1 : $3^{1/2}$. This suggests the symmetry of bi-continous network in gyroid structure was broken due to the uneven distribution of *d*-PEG in pores. The previous forbidden {110} planes become allowed Bragg planes, which cause the weak scattering peak. The appearance of the additional peak at the lower *q* range has also been observed in the online SAXS measurements of drying process of PPEGMA modified nanoporous PB filled with water as reported in Chapter 4. After drying under vacuum, the mass uptake of BD14-x4e was 12 %. *d*-PEG could be loaded in both nanopores and PB matrix.

Then the *d*-PEG loaded sample was exposed to pure chloroform. The first 1 min frame of scattering was recorded with a delay of 3 min. The scattering at low *q* values can not be found after 3 min. This might be because chloroform opens and penetrates pores very quickly, *d*-PEG molecules dissolve in chloroform and homogeneous pores form within 3 min. Peak position shifts to lower values until 5 min. The intensity increases during the first 5 min, probably due to increase in volume fraction of pores and matrix, just like an opposite phenomenon in the beginning of the drying process. The intensity starts to decrease after 5 min and reaches minimum after 15 min, caused by decrease in contrast between pores and matrix as a result of passive diffusion of *d*-PEG. After being in chloroform for 1 h, the sample was taken out and dried under vacuum. The scattering profile of dried sample is at the front and shows no nanoporous structure. There was still 1.5% mass uptake, caused by entrapped *d*-PEG in PB matrix. In order to investigate the quantity of *d*-PEG load in nanopores and matrix respectively, a PB matrix was prepared from homopolymer PB with the same cross-linking conditions as BD14-x4. This PB matrix can take 3.2 mass percentage of *d*-PEG in 4 h. This suggests that during the loading process around 75% of loaded *d*-PEG molecules are in nanopores and 25% are in PB matrix, and during the releasing process possibly all the loaded *d*-PEG molecules in nanopores and 50% of trapped *d*-PEG molecules in matrix can be released within 1 h in chloroform.

FT-IR measurements were employed to confirm the presence of *d*-PEG in BD14-x4e after loading, and absence of *d*-PEG upon the subsequent releasing. The band of the C-O-C stretching vibrations at 1115 cm^{-1} as shown in Figure 6.7 is the evidence for the presence of *d*-PEG in BD14-x4e. Other characteristic peaks for d-PEG at 2170, 2075, 1255 and 802 cm^{-1} are clearly observed in the sample after loading by IR spectrum as well. After releasing and drying, the peaks associated with *d*-PEG

disappear, owing to most of *d*-PEG were released. Mass measurement shows that there is still some residual of *d*-PEG, but it is difficult to detect this small quantity of *d*-PEG by IR spectrum.

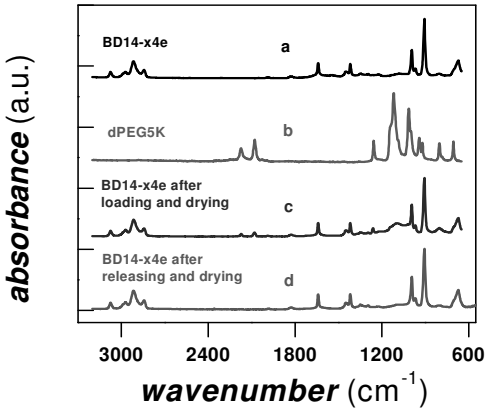

Figure 6.7. FT-IR spectra of (a) BD14-x4e, (b) *d*-PEG, (c) BD14-x4e after *d*-PEG loading and (d) BD14-x4e after *d*-PEG releasing.

6.6 Conclusion

A new type of polymer matrix for chemical delivery was developed. A collapsed 1,2-polybutadiene matrix was prepared from PB-*b*-PDMS by slightly cross-linking PB blocks and etching away the PDMS block. The matrix does not have nanoporous structure in the dry state as evidenced by SAXS and methanol uptake, but it can form a gel with uniform bicontinuous nanopores when it is exposed to a good solvent. Opening and closing of the nanopores can be controlled by swelling and drying process as well as nature of liquids. PEG molecules were successfully loaded and released by the collapsed 1,2-PB matrix as confirmed by in-situ SANS and FT-IR measurements. High loading (12 % *d*-PEG uptake) and fast releasing (20 min for reaching release equilibrium) of the collapsed matrix was observed. With further work on pore surface modification with biocompatible component, this new type of polymer matrix has the potential to be used as drug carriers.

6.7 Experimental

Cross-Linking of 1,2-PB and Etching of PDMS. Dicumyl peroxide (DCP) from Merck was used as received for the cross-linking of 1,2-PB. 0.5 % mole DCP per mole double bonds was co-dissolved with the block copolymer in THF, followed by solvent casting into a Petri dish. THF evaporated under an argon flow overnight. The cross-linking of the solvent cast film was carried out under argon at 140 °C for 1 h in a homemade gastight steel cylinder. One reference sample with a higher cross-linking degree was prepared by using 2 % mole DCP and 2 h for cross-linking reaction. 1.0 M tetrabutylammonium fluoride (TBAF) in THF from Aldrich was used as cleaving reactant for PDMS. Cross-linked samples were stirred for 36 h in a volume of THF solution containing 5 times molar excess TBAF relative to PDMS repeating unit. Afterward, the samples were washed by fresh THF and methanol for 24 h before drying under an argon flow at room temperature.

Swelling-drying. Samples (1 cm× 1 cm× 0.05 cm) were placed in home made quartz cuvettes. In the swelling experiment, one cuvette with sample inside is located in the SANS sample chamber. 4 mL of chloroform was injected into the cuvette through a Teflon tube and scattering measurement started. In the drying experiments, chloroform was sucked out from the cuvette through the Teflon tube, nitrogen flow was applied into the cuvette and scattering measurement started. After drying under nitrogen flow for 1 h, the sample was taken out from the sample chamber and placed under vacuum for 24 h.

Loading and releasing *d*-PEG. 4 mL of 100 mg/ml *d*-PEG chloroform solution was injected into a cuvette with a sample during the loading process monitored by SANS. After sample being in the solution for 4 h, the *d*-PEG solution was sucked out and the sample was dried with nitrogen flow for 40 min before it was transferred into vacuum. In the releasing experiment, the dried sample was placed back in the cuvette, which was then filled with 4 mL of chloroform before scattering measrument started.

Characterization methods. FT-IR spectra were measured on a PerkinElmer SpectrumOne FT-IR spectrometer. Methanol uptake experiments were carried out by placing dry samples in glass vials containing methanol and kept under gentle stirring at room temperature. After being submerged for a certain time a fine tissue was used to dry the surfaces of the sample quickly before weighing. SAXS were done at Risø-DTU using Cu Kα x-rays with a wavelength of $\lambda = 1.54$ Å and at beamline 7-11 at MAX-lab synchronton radiation source with a wavelength of $\lambda = 1.10$ Å in Lund,

Sweden. SANS measurements were performed on a instrument SANS-II at SINQ, Paul Scherrer Institute (PSI) in Villigen, Switzerland, with a wavelength of $\lambda =$ 4.55 Å.

6.8 References

1. Szewczykowski, P. P.; Andersen, K.; Schulte, L.; Mortensen, K.; Vigild M. E.; Ndoni, S. *Macromolecules* **2009**, *42*, 5636.

Chapter 7 Summary

Highly ordered nanoporous polymers with tunable pore sizes (5-50 nm), narrow pore size distribution, controlled pore shape and various morphologies can be prepared through the removal of the one or more block components from self-assembled block copolymer precursors. The resultant nanoporous polymers have many potential applications including templates for nano objects, separation membranes, ultra-low dielectric constant materials and waveguides. These applications do not only rely on unique structural properties but also on the chemical functionalities of the prepared nanoporous polymers. Therefore, obtaining nanoporous polymers with controlled synergy of structural properties and functionalities is very essential.

The structural properties of nanoporous polymers can be engineered through designing the total length, composition and incompatibility of the blocks during the synthesis of the block copolymer precursors. Functionalities of nanoporous polymers can be variable through different approaches. In this thesis the viability of five different approaches to functionality has been discussed:

1. A P*t*BA-*b*-PS diblock copolymer precursor has been synthesized by ATRP and a PDMS-*b*-P*t*BA-*b*-PS triblock copolymer precursor by a combination of living anionic polymerization and ATRP. PS was the matrix and mechanically stable component, P*t*BA block could be converted by acidic deprotection to hydrophilic PAA generating at the same time nanoporosity and PDMS could be quantitatively etched to provide additional nanoporosity. Both the deprotection of *tert*-butyl groups in P*t*BA and selective etching of PDMS were realized by one step operations using either HF or TFA. The bulkiness of the protection group in the acrylate polymer and the length of the PDMS chain can be used as controlling handles for the porosity and pore size.
2. Surface-initiated ATRP has been applied as a '*grafting from*' technique to obtain functional nanoporous polymers based on nanoporous 1,2-polybutadiene. The ATRP monolith initiator was prepared by immobilizing bromoester initiators onto the pore walls through two different methodologies: (1) three-step chemical conversion of double bonds of PB into bromoisobutyrate, and (2) photochemical functionalization of PB with bromoisobutyrate sites. Hydrophilic polyacrylates (PHEMA, PPEGMA) and proton conductive sulfonated polymers (PAMPS and PSS) have been successfully grafted onto the pore walls by ATRP.

3. Click chemistry has been used as a '*grafting to*' technique. Azide groups were attached on the pore walls of nanoporous PB, and alkynated MPEG was clicked onto immobilized azide groups on the pore walls by CuAAC reaction.
4. Property of pore surfaces could also be modified through surface coating of an ultra thin film. Vapor phase deposition is a suitable method for the purpose due to high mobility of small chemicals in vapor phase. Conductive nanoporous polymers were prepared by vapor phase polymerization of pyrrole with ferric *p*-toluenesulfonate as an oxidant onto the pore walls of nanoporous PB.
5. If the polymer matrix (PB in the present work) is cross-linked at a very low degree before removing the other block, pores will be collapsed due to insufficient mechanical support. Nanoporosity can be re-established when the PB matrix is subjected to a good solvent. The nanopores can be opened or closed dependent on the presence or absence of solvent as well as nature of solvents. Properties on control of pore states can be used for applications on chemical delivery systems.

There are pros and cons for each method. For example, ABC triblock copolymers allow formation of nanoporous polymers with more complicated morphologies while they need more sophisticated synthesis strategies. Surface-initiated ATRP and click chemistry afford the preservation of nanostructure after functionalization and versatile choices of functionalities while suffers a relatively low grafting density. Surface coating by vapor phase deposition is a rather easier way to modify the pore surfaces, but choices of chemicals are limited and uniformity of the coating is hardly controlled. Cross-linking can adjust the mechanical properties of cross-linkable polymer matrix; however, applicability of cross-linking is not suitable for polymers which can not be easily cross-linked. The method should be chosen according to the specific application.

The combination of defined structures and controlled functionalities opens up new opportunities for development of functional nanoporous polymers as well as broadens the spectrum of applications of nanoporous polymers.

Appendix A Introduction of Primary Amines to Nanoporous 1,2-Polybutadiene by UV Irradiation

Benzophenonyl bromoisobutyrate (BPBriBu) was successfully immobilized onto the pore walls of nanoporous PB under UV irradiation to generate bromoester initiators for ATRP as described in Chapter 4. The principle of the immobilization is based on the hydrogen abstraction and radical combination between BPBriBu and PB. Therefore, we conducted preliminary work on introduction of primary amines to nanoporous PB by UV irradiation presented in this appendix. For this reason, an anthraquinone (AQ) photolinker containing primary amino groups (AQ-NH_2) has been used. The AQ-NH_2 has been reported to be grafted on flat PS and SU-8, which is an epoxy-based polymer, surfaces.[1,2] Once primary amino groups are generated on the pore walls, many other different functionalities can be expected to be introduced by reacting with the attached amino sites.

A mixture of MeOH/Milli-Q H_2O (80/20 v %) is used as a solvent to help transport AQ-NH_2, which is a white powder, into pores of PB. The mixture can only penetrate into pores without swelling the PB matrix to ensure the subsequent photochemistry exclusively occurs in the pores. The solvent evaporates under vacuum before samples are placed into a quartz bottle filled with nitrogen. The reaction of AQ-NH_2 with PB under UV is similar to that of BPBriBu with PB and is simplified in Scheme A-1. UV irradiation makes hydrogen abstraction from C-H bond of PB by one carbonyl oxygen in AQ-NH_2, as a result a semiquinone radical is formed. The semiquinone radical can subsequently recombine with the alkyl radical generated in PB to create a covalent link.[2]

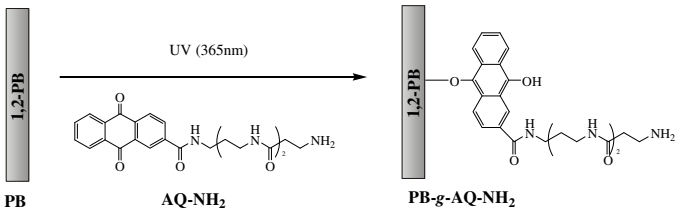

Scheme A-1. Reaction of AQ-NH_2 with PB under UV irradiation.

After UV irradiation with wavelength of 365 nm for 1 h, the samples are washed with copious amount of MeOH/H_2O to remove unattached AQ-NH_2 compounds. The modified samples are dried and weighed. Degree of grafting (DOG) is usually used to characterize the amount of grafted compounds. DOG can be calculated by the following equation:

$$DOG = \frac{m_g - m_0}{m_0} \qquad \text{(A. 1)}$$

where m_g and m_0 are the mass of film after and before grafting, respectively.

DOG vs. AQ-NH_2 concentration is shown in Figure A.1. DOG increases with AQ-NH_2 concentration up to 100 mg/ml. The maximum obtained DOG is about 4.7 %, from which surface density of AQ-NH_2 can be calculated as 0.2 unit/nm^2.

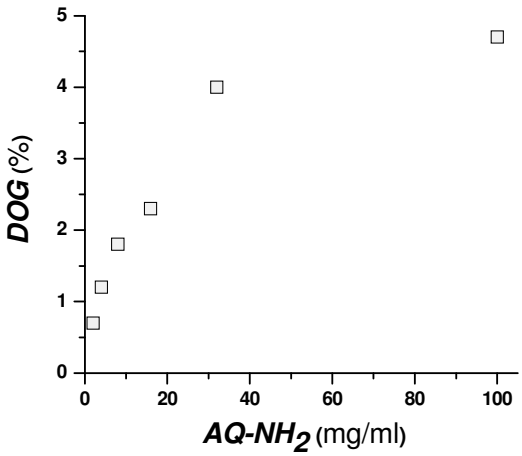

Figure A.1. Degree of grafting by using various AQ-NH_2 concentrations.

FT-IR was used to investigate the chemical composition change in nanoporous PB after and before grafting as shown in Figure A.2. Additional absorption between 1650 and 1730 cm^{-1} in spectrum of PB-*g*-AQ-NH_2 corresponds to the C=O bond in AQ-NH_2. This indicates AQ-NH_2 is attached in nanoporous PB.

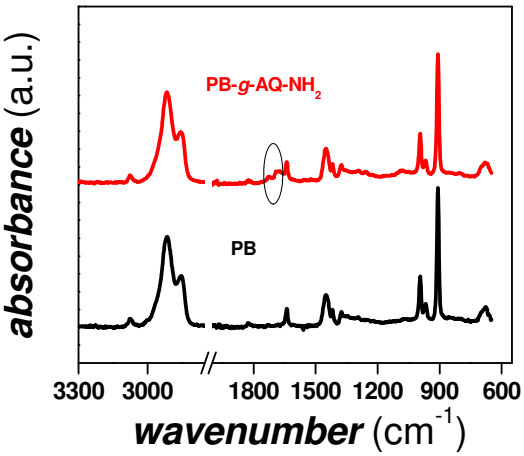

Figure A.2. FTIR spectra of PB and PB-*g*-AQ-NH_2 (with AQ-NH_2 concentration of 16 mg/ml).

Bromophenol blue (BPB) can be used as an indicator to detect the amino group. The binding of amino groups and BPB gives blue color.[3] As seen in Figure A.3, the original nanoporous PB is colorless and transparent. After grafting of AQ-NH_2, the PB film becomes slight yellowish. When the grafted PB film is submerged in BPB solution of DMF, blue color appears throughout the whole film. BPB can be washed away by piperidine, which is why the color of the film turns back to slight yellow when piperidine is applied.

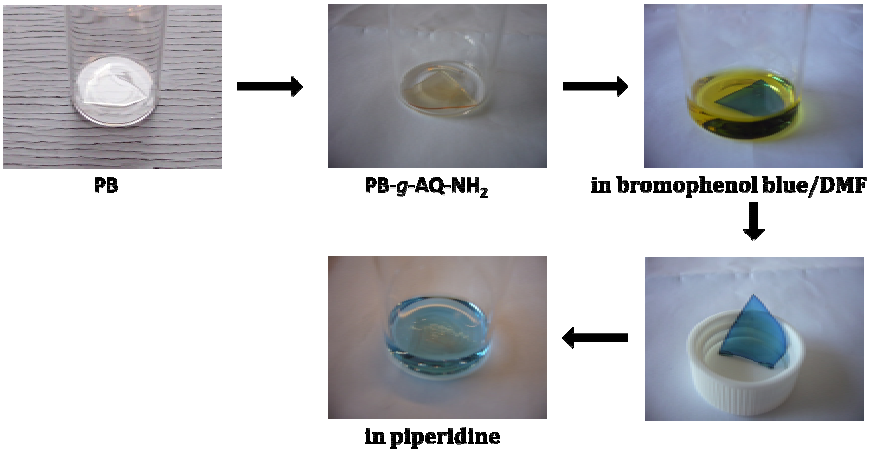

Figure A.3. Color change of PB, PB-*g*-AQ-NH_2, and PB-*g*-AQ-NH_2 in BPB and piperidine solutions.

References

1. Tech Note, Volume 4, No. 26, Nalge Nunc International.
2. Blagoi, G.; Keller, S.; Persson, F.; Boisen, A.; Jakobsen, M. H. *Langmuir* **2008**, *24*, 9929.
3. Geschwind, I. R.; Li, C. H. *Ibid.* **1952**, *74*, 834.

Appendix B Contrast Variation SANS Experiments of Nanoporous 1,2-Polybutadiene

Introduction

In chapter 4, the preparation of functional nanoporous 1,2-polybutadiene (PB) with gyroid morphology via surface-initiated ATRP has been described. SAXS and TEM have been utilized to characterize structure of nanoporous PB after modification. In addition to SAXS, SANS is also well suited for structural investigation of complex polymer systems. By deuterium labeling one block of polymer chains and varying neutron scattering length density (SLD) of solvents, different structural properties of complex polymer systems can be highlighted.[1] In this appendix, contrast variation SANS experiments of modified nanoporous PB are shown. Deuterated poly(methyl methyacrylate) (PMMA) (*d*PMMA) was grafted into nanoporous PB by surface-initiated ATRP. The sample PB-*g*-*d*PMMA was investigated in mixtures of protonated methanol (*n*MeOH) and deuterated methanol (*d*MeOH) and mixtures of chloroform ($CHCl_3$) and THF. Different scattering functions were obtained due to the different neutron SLD of solvents and different solubility of PMMA in solvents.

Contrast matching for nanoporous PB

The mixtures of *n*MeOH and *d*MeOH with different volume fractions and the mixtures of $CHCl_3$ and THF with different volume fractions were used as solvents in contrast matching measurements for nanoporous PB. Contrast matching is to find the critical conditions where no scattering contrast between the solvent and PB matrix exist. For a two phase system, the scattering intensity is proportional to the square of the difference between the scattering length densities of phase A and phase B.

$$I \propto (\rho_A - \rho_B)^2 P(Q) S(Q) \qquad \text{(B.1)}$$

where ρ_A and ρ_B are scattering length densities of phase A and B respectively. $P(Q)$ is form factor, which depends on the shape and size of the individual phase. $S(Q)$ is structure factor, which tells the spatial arrangement or interactions between phases.

The nanoporous PB has an ordered gyroid morphology with pore diameter of 14 ± 1 nm, and SAXS data shows that domain spacing between two {211} planes is around 18 nm (data are shown in Chapter 4). The mass densities and neutron SLD of PB and solvents can be found in Table B.1.

Table B.1. Mass densities and neutron scattering length densities of chemicals used in the appendix.

Chemicals	Density (g/cm^3)	Neutron SLD (cm^{-2})
cross-linked PB	1.03	0.48×10^{10}
MeOH	0.791	-0.37×10^{10}
*d*MeOH	0.88	5.80×10^{10}
THF	0.889	0.18×10^{10}
$CHCl_3$	1.492	2.38×10^{10}
PMMA	1.171	0.83×10^{10}
*d*PMMA	1.255	9.16×10^{10}

MeOH is known as a bad solvent for PB. It only penetrates the pores of nanoporous PB without swelling the PB matrix (see Methanol Uptake in Chapter 3). The SANS data from nanoporous PB in the mixture of *n*/*d* MeOH with varying fractions of *d*MeOH are shown in Figure B.1. The scattering intensity in Y axis of the figure is not in absolute value, because background subtraction was not done for the scattering profiles. We are still able to see that the intensity of main peak decreases with the increasing fraction of *n*MeOH until the contrast matching point, where 86.5 v% of solvent is *n*MeOH. At this point, the peak disappears totally (see blue curve in Figure B.1), suggesting that the neutron SLD of solvent is the same as that of PB matrix. If the concentration of *n*MeOH continues to increase after this point, the peak will show up again as indicated with purple and dark blue curves in Figure B.1.

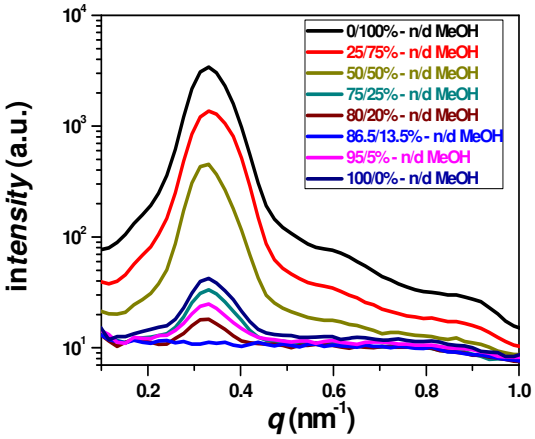

Figure B.1. SANS contrast matching measurements of nanoporous PB in mixtures of *n*/*d* MeOH with different volume fractions.

Figure B.2 shows the linear relationship between the square root of scattering intensity and volume fraction of *n*MeOH in solvent. It confirms that neutron SLD of the mixture is proportional to the volume fraction of *n*MeOH or *d*MeOH. By using the same contrast variation method, contrast matching conditions for mixtures of $CHCl_3$ and THF to nanoporous PB can be found when 87 v% of solvent is THF (data are not shown).

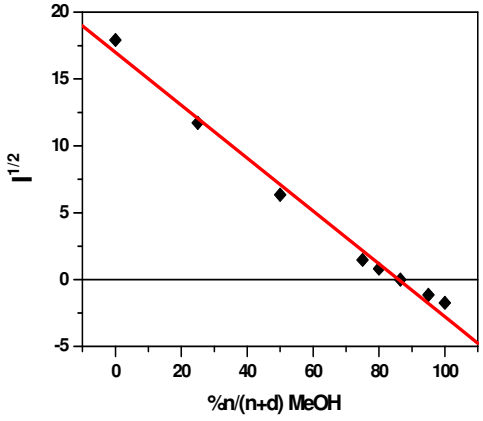

Figure B.2. Square root of scattering intensity versus volume fraction of *n*MeOH in solvent.

SANS of PMMA- or *d*PMMA-grafted nanoporous PB

Two modified nanoporous samples, PB-*g*-PMMA and PB-*g*-*d*PMMA were prepared by surface-initiated ATRP of MMA and *d*MMA onto pores of nanoporous PB. The ATRP initiator, bromoisobutyrate, was immobilized onto pores via photochemical functionlization method as described in Chapter 4. After ATRP reaction for 0.5 h, PMMA and *d*PMMA were grafted onto the pores. The volume uptakes of grated polymers are listed in Table B.2. The thicknesses of grafted layers for two samples are more or less the same, and they are roughly estimated between 1-2 nm based on volume uptake results.

Table B.2. Cumulative volume fraction (v%) of the two modified nanoporous samples at different stages of modification. The mass densities of PMMA and *d*PMMA are taken as 1.171 and 1.255 g/cm^3, respectively.[2]

Monomer	PB	PB-Br	PB-*g*-polymer
MMA	59.2	61.8	74.7
*d*MMA	59.2	61.8	71.2

Figure B.3 shows SANS data of nanoporous PB, PB-*g*-PMMA and PB-*g*-*d*PMMA, and their possible scattering length density profiles. For nanoporous PB, we can only observe one scattering peak at q value of around 0.34 nm^{-1}(see Figure B.3 a), which is very close to the value obtained by SAXS (see Figure 4.7 Chapter 4). Due to the low resolution of SANS, the higher order peaks for gyroid morphology are missing. When PMMA is grafted onto pores, an additional peak at q value of around 0.62 nm^{-1} appears as shown in Figure B.3 b. The appearance of this additional peak is also observed from SAXS data of other modified nanoporous PB (see Chapter 4), and it is possibly caused by the form factor of core-shell pores, which are formed by air-core and PMMA shell. When the grafted polymer is deuterated PMMA instead of protonated PMMA, the scattering intensity of the additional peak is enhanced by a factor of 10 (see Figure B.3 c), whereas the scattering intensity of the primary peak doesn't change much for all three samples. The intensity increase of the additional peak for PB-*g*-*d*PMMA is because the neutron SLD of *d*PMMA is much higher than those of other compounds in the system.

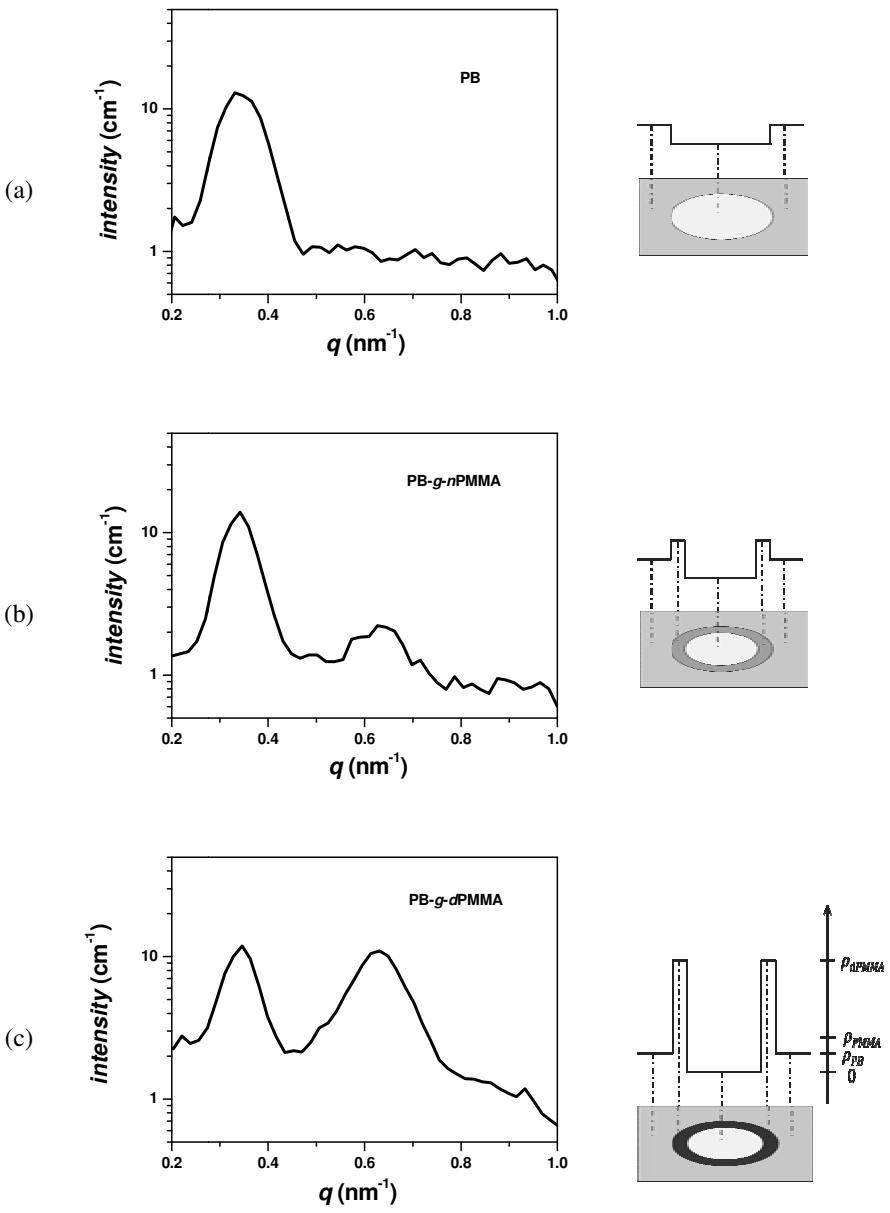

Figure B.3. SANS data of (a) nanoporous PB, (b) PB-*g*-PMMA and (c) PB-*g*-*d*PMMA, and schematic illustration of their possible scattering length density profiles. In the illustration, gray color is for PB matrix, white is for air, dark gray is for PMMA and black is for *d*PMMA.

Mixtures of *n*/*d* MeOH and mixtures of $CHCl_3$ and THF were used as solvent to investigate structure information of PB-*g*-*d*PMMA. Methanol is a poor solvent for PMMA, while $CHCl_3$ and THF are good solvents for PMMA. These can be verified by Hansen solubility parameters.[3] Figure B.4 shows SANS data of PB-*g*-*d*PMMA in pure MeOH and in mixture of *n*/*d* MeOH (86.5/13.5 v%). The scattering profile of PB-*g*-*d*PMMA in pure MeOH shown in Figure B.4 a is very close to that of dry PB-*g*-*d*PMMA (see Figure B.3 b), that is because the SLD profiles for the two cases are very similar. When pure MeOH is replaced by the mixture of *n*/*d* MeOH (86.5/13.5 v%), the intensity of primary peak is reduced, while the peak at *q* value of 0.62 nm^{-1} remains the same (see Figure B.4 b). Intensity of the additional peak becomes higher than that of the primary peak, indicating that the scattering from *d*PMMA shell becomes dominant and the structure contribution to the scattering profile is significantly reduced at this contrast matching point.

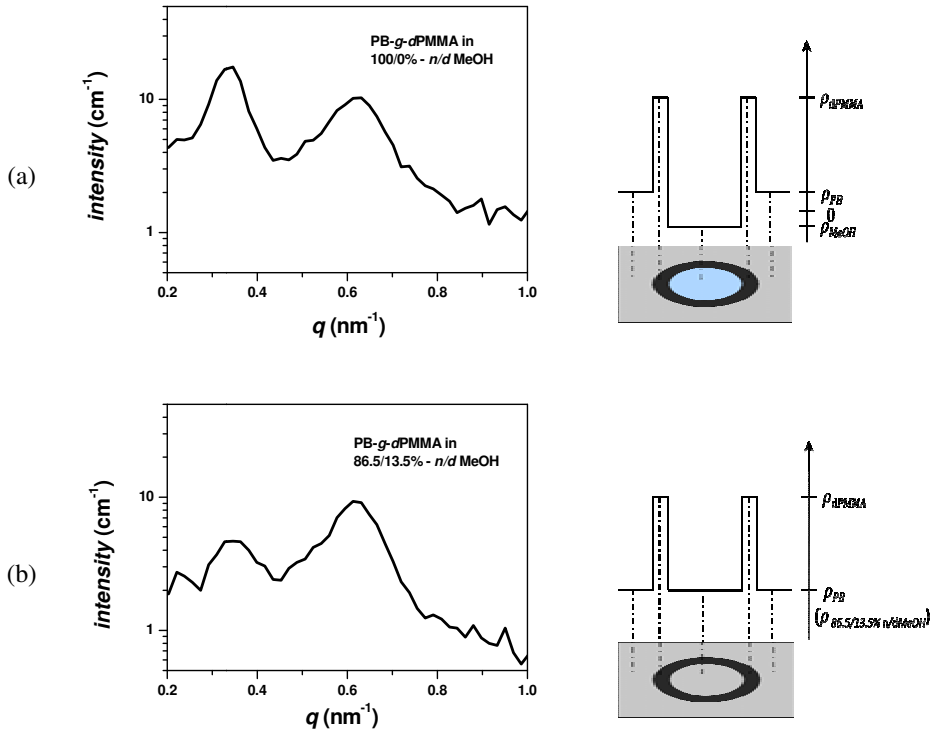

Figure B.4. SANS data of (a) PB-*g*-*d*PMMA in pure MeOH and (b) in mixture of *n*/*d* MeOH (86.5/13.5 v%), and their possible scattering length density profiles.

Figure B.5 shows SANS data of PB-*g*-*d*PMMA in pure $CHCl_3$ and mixture of THF/ $CHCl_3$ (87/13 v%). The scattering profiles look similar to that of nanoporous PB without any modification. The additional peak at q value of 0.62 nm^{-1} vanishes for both cases. One of possible explanation is that *d*PMMA is well dissolved in the solvents and relatively homogeneous solutions are created, and as a result, scattering length density functions become flat in pores. Core-shell morphology disappears and contribution from the corresponding form factor doesn't exist. Structure contribution of gyroid morphology becomes dominant again. Due to the high neutron SLD of $CHCl_3$, the scattering from PB-*g*-*d*PMMA in pure $CHCl_3$ is expected to be much more intensive than in the mixture of THF/ $CHCl_3$ (87/13 v%). Originally the mixture has the same neutron SLD as PB matrix, but the neutron SLD in pores is slightly larger than that of PB matrix because of contribution from *d*PMMA.

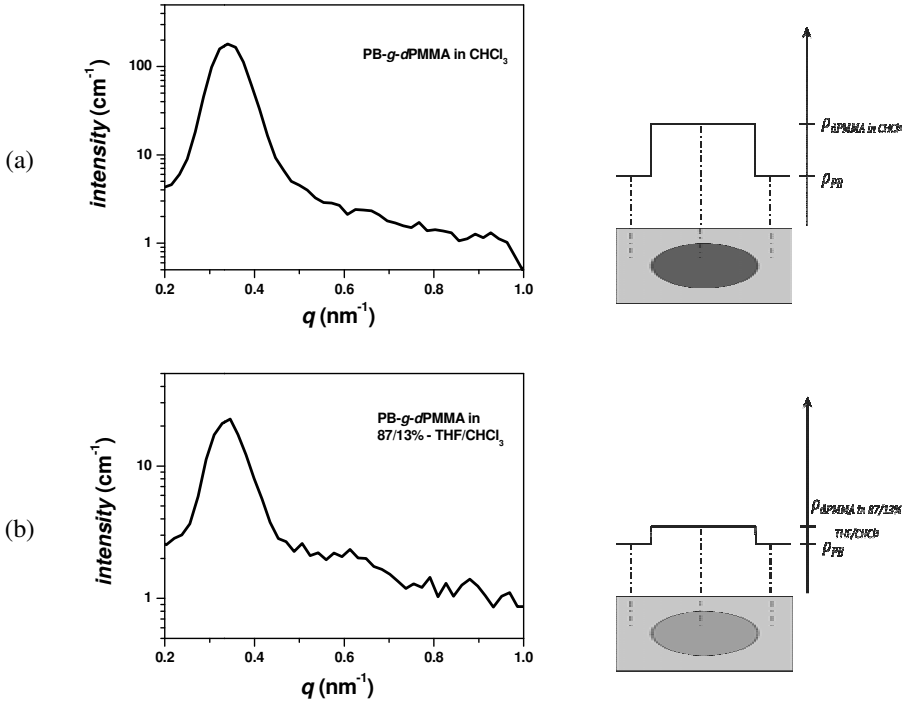

Figure B.5. SANS data of (a) PB-*g*-*d*PMMA in pure $CHCl_3$ and (b) in mixture of THF/ $CHCl_3$ (87/13 v %), and their possible scattering length density profiles.

References

1. Mortensen K. *Structural Studies of Polymer Systems Using Small-Angle Neutron Scattering.* **2001**, Gordon & Breach Science Publishers.

2. Ngoepe, P. E.; Lambson, E. F.; Saunders, G. A.; Bridge, B. *J. Mater. Sci.* **1990**, *25*, 4654.

2. Hansen C.M. *Hansen solubility parameters – a user's handbook.***1999**, Boca Raton (FL): CRC Press.

Department of Chemical
and Biochemical Engineering

DTU Building 229
Søltofts Plads
DK-2800 Kgs. Lyngby
www.kt.dtu.dk